Delft University of Technology

Numerical optimization techniques for practical problems in Aerodynamics

Belligoli, Z.

Important note
To cite this publication, please use the final published version (if applicable).
Please check the document version above.

NUMERICAL OPTIMIZATION TECHNIQUES FOR PRACTICAL PROBLEMS IN AERODYNAMICS

Dissertation

for the purpose of obtaining the degree of doctor
at Delft University of Technology,
by the authority of the Rector Magnificus Prof.dr.ir. T.H.J.J. van der Hagen,
chair of the Board of Doctorates,
to be defended publicly on
Friday 26 March 2021 at 12:30

by

Zeno BELLIGOLI

Master of Science in Aerospace Engineering,
Delft University of Technology, the Netherlands,
born in Verona, Italy.

This dissertation has been approved by the promotors.

Composition of the doctoral committee:

Rector Magnificus,	chairperson
Prof. dr. ing. G. Eitelberg	Delft University of Technology, promotor
Dr. R. P. Dwight	Delft University of Technology, promotor

Independent members:

Prof. dr. ir. L. L. M. Veldhuis	Delft University of Technology
Prof. dr. P. Schmid	Imperial College London, United Kingdom
Prof. dr. H. Xiao	Virginia Tech, Unites States of America
Prof. dr. S. Görtz	Technische Universität Braunschweig, Germany
Dr. J. E. V. Peter	Université Paris Saclay, France

Reserve member:

Prof. dr. S. Hickel	Delft University of Technology

TUDelft Delft University of Technology

To my parents

Table of Contents

Summary

The continuous increase in the number of flights in the last decades caused a steep growth of aviation-related pollution to the point that the aviation sector is responsible for 3% of the global greenhouse gas emissions. Regulators have been slow at catching up with this problem, and stringent emission targets have been put in place only very recently. As a consequence, innovative solutions to make airplanes comply with regulations must be sought in a short time span. However, the aviation industry is known to be risk-averse and slow at incorporating innovation, especially when it comes to new aerodynamic designs.

A decisive acceleration to the design development process has been given by the introduction of aerodynamic shape optimization techniques (ASO), using a computational fluid dynamics (CFD) code to optimize the shape of a part of an aircraft in order to reduce its aerodynamic drag and, consequently, its overall carbon footprint. The first part of this dissertation focuses on the optimization of the wing-fuselage junction, a region where complex flow phenomena significantly contribute to the total drag of the aircraft. The ASO discovers an innovative shape of the fuselage that reduces drag by activating a propulsive pressure force that would otherwise be null.

However, the CFD code used for the ASO is subject to uncertainties and errors and so is the complex experiment carried out to validate the optimized design. As a consequence, the confidence in the results of Reynolds-averaged Navier-Stokes (RANS) simulations and wind-tunnel experiments of complex flow phenomena is often limited. Hence, the second part of the dissertation explores ways to reduce these errors by developing two variational data assimilation (DA) techniques that inject sparse experimental data into a RANS code in order to correct the Reynolds stress tensor (RST) computed by a linear eddy viscosity turbulence model, one of the largest sources of errors in a CFD simulation. The DA problem is formulated in a way to guarantee the physical realizability of the RST and the results demonstrate an excellent ability to reconstruct complex flow fields. Finally, the DA methodology is extended to incorporate corrections to the experimental angle of attack and Mach number, thus being able to simultaneously correct turbulence modeling and wind-tunnel wall interference errors. The methodology is validated on 2D and 3D test cases, showing that different corrections for the angle of attack and Mach number than those from conventional correction techniques are needed for an optimal reconstruction of the flow field around the test object.

1

Introduction

> **Disclaimer**
>
> The work presented in this dissertation was carried out, for the most part, before the beginning of 2020, under a favourable economical situation which stimulated research and innovation. The introductory part of this dissertation highlights the main economical and societal reasons – under that climate – that made this research project possible. These reasons have been shaken by the coronavirus pandemic, whose economical consequences hit the aviation sector particularly hard. Only time will tell whether these adverse economical effects will downsize the ambition of the aviation giants for good (and the funds for research and innovation with it), or just be an unexpected accident on their path to connect the world.

Air transport is key to global economic development as it provides direct, reliable and fast connections between cities – enabling the flow of goods, people, capital, technology and ideas – at a steadily decreasing cost. This strategic role is underpinned by the positive economic performance of the last decade. Indeed, annual passenger enplanements rose from about 2.5 billion in 2008 to more than 4.0 billion in 2017. Over the next 20 years, passenger traffic is expected to grow at an average annual rate of 4.7 percent, contributing to increased aircraft production. Stronger order intake in the past several years resulted in a record-high commercial aircraft backlog of 14,215 units at the end of 2017, representing more than nine years of current annual production [1]. Similarly, cargo traffic is expected to grow 4.2% annually for the next twenty years. As a consequence, 2650 freighters will be delivered in this time span, with approximately half replacing retiring airplanes and the remainder expanding the fleet to meet projected traffic growth [2].

Because of the current and anticipated increase in aircraft production and number of flights, regulators have started to worry about the environmental impact of these machines. The main aircraft engine emission pollutants are carbon dioxide (CO_2), nitrogen oxides (NO_x), sulfur oxides (SO_x), unburned hydrocarbons (HC), carbon monoxide (CO), particulate matter (PM) and soot. CO_2 is a greenhouse gas and thus contributes to the phenomenon known as *global warming* [3], while the other gases and particles are mainly responsible for health-related problems [4]. In particular, aircraft CO_2 emissions increased from 88 to 156 million tonnes (+77%) between 1990 and 2005 [5]. In the same period, NO_x emissions increased by 85 percent. In fact, *all* aircraft-related emissions are projected to increase in the next 20 years [6].

Over 90 percent of the commercial aircraft unit backlog belongs to Airbus and Boeing [7], the two biggest aircraft manufacturers in the world, whose duopoly has lasted since the 1990s. More than 80 percent of the current orders of new airplanes are for the widely popular Airbus A320 [8] or Boeing 737 [9]. Hence, these two models are the main contributors to aviation-related pollution. Although these machines are the most technologically advanced the industry has ever seen, their design is based on 35-year-old and 55-year-old concepts, respectively. Compared to their ancestors, the new generations feature more lightweight materials, more efficient engines, and better aerodynamics. How-

ever, current and future technology improvements will likely not be able to counteract the increasing environmental impact of the aviation industry [10].

As a consequence, stringent new regulations on pollution are being devised and implemented by policymakers. As an example, regulating aircraft emissions was part of the Obama administration's goal under the Paris Climate Agreement [11]. To comply with these new limitations, the pace at which innovation is incorporated into the design process must accelerate.

The aerodynamic sector has been particularly slow at implementing innovative designs in commercial aircraft. A notable example is the winglet, a concept first introduced at the beginning of the 20th century that started to be widely applied only twenty years ago. This is because the process of aerodynamic design requires both creative effort and a great deal of routine and manual modeling work. Working with such modeling tools is, for the most part, laborious and repetitive, and it demands specialized skills. As a result, a large portion of time is spent in the attempt to obtain a new design, which not only has to be energy-efficient but also has to respect all the constraints imposed on it to be incorporated into the final airplane.

In this context, automatic design techniques based on optimization methods have contributed to accelerate the pace at which innovative designs are generated. In particular, they routinely and automatically modify an initial configuration to optimize a given figure of merit under certain constraints. This process often produces new geometric shapes that could have hardly been conceived by a human engineer (see, for example, [12, 13]).

1.1 Aerodynamic Shape Optimization

Thanks to the progress in high-performance computing and the development of optimization algorithms, the last twenty years have witnessed the birth and development of automated design methods based on computational fluid dynamics (CFD), also known as aerodynamic shape optimization (ASO). The goal of ASO is to find a shape that minimizes/maximizes a specific objective function while adhering to appropriate constraints. For example, one can optimize the shape of a wing in order to minimize its drag while keeping a certain amount of lift. These methods can be classified as either deterministic or non-deterministic depending on the type of optimization algorithm employed [14].

Non-deterministic algorithms do not require any gradient information of the objective function and are suited for noisy objective functions because of their ability to escape local optima. On the other hand, they require a large number of function evaluations (CFD runs) to converge to an optimum solution, with associated long optimization times. This is why they are often coupled with reduced-order models (ROMs) for efficiently exploring the design space. Nevertheless, the number of variables that can be concurrently optimized with non-deterministic techniques is still limited, thus making them unsuitable for solving high-dimensional optimization problems [15].

By contrast, deterministic methods, and in particular gradient-based algorithms, require the computation of the sensitivities of the objective function with respect to the control parameters. Hence, they tend to converge to local optima and their use with noisy

objective functions is not recommended. However, the introduction of the adjoint method in the field of fluid dynamics by Pironneau [16], and its extension to ASO by Jameson [17] permitted to obtain accurate gradients with a computational cost independent from the number of control parameters, thus making them the most viable choice for solving large-scale ASO problems.

Despite this disruptive change in the design process, optimizing a full aircraft still requires considerable computational resources seldom available in practice. Therefore, the application of ASO is usually limited to a particular component of the airplane. In the last years, gradient-based optimization techniques have been used to optimize the shape of turbine blades [18, 19], high-lift devices [20], and wings [21, 22] among others.

In this context, one of the most critical areas is the wing/fuselage junction, i.e. the region where the wing connects to the body of the airplane. The junction area is estimated to be responsible for approximately 10 percent of the total drag of an aircraft [23] and the ideal way to mitigate its effects would be to re-design the aircraft in such a way that no junction geometry is present as in the case of the blended wing/body concept [24, 25]. Although several studies proving the superiority of this design over the one currently in use have been published [26], many technical and regulatory challenges have still to be overcome before the blended wing/body aircraft could take off in our skies. Hence, the conventional wing/fuselage geometry still is the primary subject of drag minimization studies. The most popular solutions for this purpose are (i) the use of a leading-edge fillet to reduce the adverse pressure gradient responsible for flow separation at the wing nose, and (ii) the outward deformation of the fuselage to form a fairing that keeps the flow attached for as long as possible. Historically, their design has relied on the know-how of a small group of experts and a trial-and-error process based on small changes to a baseline geometry [27]. Only recently automated design techniques have started to be used to explore the wing/body junction design space more thoroughly [12, 21, 28, 29].

The majority of these studies have focused on optimizing the wing shape at the junction, showing that a careful re-design of that part of the wing could significantly reduce the drag and improve the aircraft performance.

In contrast, little attention has been paid to the effect of changing the geometry of the fuselage. Researchers started focusing on this problem only in the last fifteen years, and the results suggest that optimizing the fuselage shape at the junction could reduce drag more than optimizing the wing root shape [12]. However, most of the works either allow only outward deformations of the fuselage in an attempt to obtain fairings resembling those in use on modern aircraft [30] or treat the fuselage shape optimization as a toy problem for the validation of numerical methods without further investigating the physics of the new design.

In this regard, Chapter 3 investigates the possibility of reducing the drag at wing/body junctions by optimizing the shape of the body solely, without any constraint on the spanwise direction of the deformation. This idea was originally proposed for a transonic aircraft configuration by Brezillon and Dwight [12], and subsequently explored on a simpler geometry at subsonic conditions by Belligoli [31]. In this dissertation I build upon the insights generated by these studies to set up an ASO problem that is able to discover a novel body design that reduces the aerodynamic drag. Furthermore, the performances of

the novel geometry are compared to those of more conventional designs, the results validated in a wind tunnel experiment, and the flow physics at the location of the optimized design thoroughly investigated to finally unveil a new mechanism for reducing junction drag.

1.2 Data Assimilation

Any new design generated via ASO should be validated by a wind-tunnel experiment since CFD simulations are subject to uncertainties and errors. Reynolds-averaged Navier-Stokes (RANS) codes, which are the workhorse of this dissertation, have four main sources of errors [32, 33]:

- discretization errors: due to a coarse temporal/spatial discretization of the problem;

- iterative convergence errors: due to soft stopping criteria for the iterative solution methods of the simulation;

- geometry modeling errors: due to uncertainties and simplifications in the geometry to simulate;

- turbulence modeling errors: due to the approximate models used to reproduce the behavior of turbulence.

While the first three sources of error can be minimized by choosing an adequately refined mesh and appropriate stopping criteria for the iterative algorithms, dealing with the latter is difficult. Turbulence operates within a vast range of length scales, the smallest of which require enormous computational resources to be resolved, even for moderate Reynolds numbers. This is why RANS simulations make use of a turbulence model to approximate the effect of turbulence on the mean flow. These models are calibrated using data from simple, canonical experiments [34] and have proven to be reliable for the simulation of many fluid dynamic phenomena. However, their reliability plunges when the flow becomes too complex [35] and only an experiment can validate the numerical results [36].

Nevertheless, wind-tunnel experiments are also subject to errors and uncertainties due to the interference between the components of the wind tunnel and the object to test [37]. The presence of the wind-tunnel walls, for example, alters the field of flow about the test object from what it would be if they were not present. Hence, wind-tunnel wall interference corrections are necessary to compute the equivalent free-air state corresponding to the in-tunnel conditions. This topic is especially relevant in light of the current tendency to test bigger models in the wind tunnel to reach high Reynolds numbers.

Several techniques have been developed for correcting wall interference in the linear flow regime [38], i.e. subsonic flow conditions without separation. These methods make use of a linear potential flow code to compute the interference corrections and, as such, their scope is limited by assumptions of the mathematical model and the approximations in the computer code. In other words, an interference correction technique is as reliable as the numerical model used for it.

By contrast, only few correction techniques exist for the non-linear regime, despite this pertaining to the majority of the flight envelope of a modern airliner. A non-linear correction technique must rely on a non-linear CFD code, thus inheriting all the uncertainties and errors associated with that code [39].

Errors and uncertainties associated with the computational models and their validation in the wind tunnels have contributed to the slow pace at which innovative commercial aircraft designs are adopted. Therefore, in Chapter 4, I propose two approaches utilizing data assimilation to reduce some of these errors.

Data assimilation (DA) is a particular type of optimization which minimizes the difference between some high-fidelity data and the corresponding numerical counterpart by finely tuning the simulation parameters. It could be seen as an ad-hoc calibration of a numerical code for a single, specific test case.

Despite being a very natural way to incorporate experimental and numerical results, data assimilation has never been applied for the correction of wall interference in wind-tunnel experiments. On the other hand, it has already been used to quantify and correct the errors due to turbulence modeling, but only a few studies were published on the topic [40–42].

In this regard, in Chapter 5, I propose a data assimilation technique to solve the problem of non-linear wind-tunnel wall interference corrections. I give particular attention to the correction of the turbulence model error, and propose three different ways to do so.

1.3   Contribution

The original contribution of this dissertation can be summarized as follows:

- A novel geometry reducing drag at wing-body junctions was discovered through aerodynamic shape optimization. The new design generates a pressure force opposite to the drag force thanks to the interaction between the deformed body and the wing leading-edge [1].

- Two new variational data assimilation techniques for the correction of structural and functional turbulence modeling errors have been developed and validated. They calculate a physically realizable Reynolds stress tensor which minimizes the discrepancy between some sparse high-fidelity data and the corresponding numerical data.

- A new procedure based on the integration of experimental data and turbulent CFD simulations to correct non-linear wind-tunnel wall interference has been developed and tested on 2D and 3D cases. The methodology removes many of the burdens associated with wall interference corrections and is generalizable to all types of wind tunnels.

---

[1]Contribution equally shared between Zeno Belligoli and Annemiek Koers.

1.4   Outline

After introducing the main mathematical concepts used in this dissertation in Chapter 2, in Chapter 3 I investigate whether it is possible to obtain an innovative, drag-reducing design for the wing-fuselage junction of an aircraft by only changing the shape of the fuselage. I show that, not only this is possible, but that the optimized design outperforms other designs currently in use on commercial aircraft.

Having acknowledged the uncertainties and errors in the results of CFD-based shape optimizations, in Chapter 4, I focus on the development of data assimilation frameworks to reduce turbulence modeling errors in CFD codes. There, I show how the choice of a new set of design variables improves the ability of the DA technique to reconstruct turbulent phenomena over other choices made in literature.

In Chapter 5, I exemplify how the data assimilation techniques of the previous chapter can be applied to the problem of non-linear wind-tunnel wall interference correction.

Finally, in Chapter 6, I present the main findings of this dissertation, their limitations and propose some recommendations for further developments.

References

[1] "Deloitte, 2018 Global Aerospace and Defence Industry Outlook," `https://www2.deloitte.com/content/dam/Deloitte/global/Documents/Manufacturing/gx-manufacturing-2018-global-ad-outlook.pdf`, Accessed: 2019-09-15.

[2] "Boeing, World Air Cargo Forecast 2018-2037," `https://file.veryzhun.com/buckets/carnoc/keys/3fa55da709101d0d937e78732a88cd9d.pdf`, Accessed: 2019-09-15.

[3] Meinshausen, M., Meinshausen, N., Hare, W., Raper, S. C., Frieler, K., Knutti, R., Frame, D. J., and Allen, M. R., "Greenhouse-gas emission targets for limiting global warming to 2 C," *Nature*, Vol. 458, No. 7242, 2009, pp. 1158.

[4] Kampa, M. and Castanas, E., "Human health effects of air pollution," *Environmental pollution*, Vol. 151, No. 2, 2008, pp. 362–367.

[5] "European Aviation Environmental Report 2016," `https://ec.europa.eu/transport/sites/transport/files/european-aviation-environmental-report-2016-72dpi.pdf`, Accessed: 2019-09-15.

[6] "European Aviation Safety Agency website," `https://www.easa.europa.eu/eaer/figures-tables/nox-emissions-will-increase-further-advanced-engine-combustor-technology-could-help`, Accessed: 2019-09-15.

[7] "Leeham News and Analysis website," `https://leehamnews.com/2019/01/11/airbus-holds-56-share-of-backlogs-vs-boeing/`, Accessed: 2019-09-15.

[8] "Airbus, Orders and Deliveries," `https://www.airbus.com/aircraft/market/orders-deliveries.html`, Accessed: 2019-09-15.

[9] "Boeing, Orders and Deliveries," `http://www.boeing.com/commercial/#/orders-deliveries`, Accessed: 2019-09-15.

[10] "European Aviation Safety Agency website," `https://www.easa.europa.eu/eaer/topics/overview-aviation-sector/emissions`, Accessed: 2019-09-15.

[11] "Obama White House website," `https://obamawhitehouse.archives.gov/the-record/climate`, Accessed: 2019-09-15.

[12] Brezillon, J. and Dwight, R. P., "Applications of a discrete viscous adjoint method for aerodynamic shape optimisation of 3D configurations," *CEAS Aeronautical Journal*, Vol. 3, No. 1, 2012, pp. 25–34.

[13] Belligoli, Z., Koers, A. J., Dwight, R. P., and Eitelberg, G., "Using an Anti-Fairing to Reduce Drag at Wing/Body Junctions," *AIAA Journal*, Vol. 57, No. 4, 2018, pp. 1468–1480.

[14] Verstraete, T. et al., "Introduction to optimization and multidisciplinary design," *VKI, lecture Series*, Vol. 7, 2010, pp. 93.

[15] Quagliarella, D., Périaux, J., Poloni, C., and Winter, G., *Genetic algorithms and evolution strategies in engineering and computer science*, Jhon Wiley & Sons, 1997.

[16] Pironneau, O., "Optimal shape design for elliptic systems," *System Modeling and Optimization*, Springer, 1982, pp. 42–66.

[17] Jameson, A., "Aerodynamic design via control theory," *Journal of scientific computing*, Vol. 3, No. 3, 1988, pp. 233–260.

[18] Vitale, S., Albring, T. A., Pini, M., Gauger, N. R., Colonna, P., et al., "Fully turbulent discrete adjoint solver for non-ideal compressible flow applications," *Journal of the Global Power and Propulsion Society*, Vol. 1, 2017, pp. Z1FVOI.

[19] Rubino, A., Pini, M., Colonna, P., Albring, T., Nimmagadda, S., Economon, T., and Alonso, J., "Adjoint-based fluid dynamic design optimization in quasi-periodic unsteady flow problems using a harmonic balance method," *Journal of Computational Physics*, Vol. 372, 2018, pp. 220–235.

[20] Kim, S., Alonso, J., and Jameson, A., "Design optimization of high-lift configurations using a viscous continuous adjoint method," *40th AIAA Aerospace Sciences Meeting & Exhibit*, 2002, p. 844.

[21] Reuther, J., Jameson, A., Farmer, J., Martinelli, L., and Saunders, D., "Aerodynamic shape optimization of complex aircraft configurations via an adjoint formulation," *34th Aerospace Sciences Meeting and Exhibit*, 1996, p. 94.

[22] Giles, M. B. and Pierce, N. A., "An introduction to the adjoint approach to design," *Flow, turbulence and combustion*, Vol. 65, No. 3-4, 2000, pp. 393–415.

[23] Gand, F., Deck, S., Brunet, V., and Sagaut, P., "Flow dynamics past a simplified wing body junction," *Physics of Fluids*, Vol. 22, No. 11, 2010, pp. 115111.

[24] Brown, M. and Vos, R., "Conceptual design and evaluation of blended-wing body aircraft," *2018 AIAA Aerospace Sciences Meeting*, 2018, p. 0522.

[25] Faggiano, F., Vos, R., Baan, M., and Van Dijk, R., "Aerodynamic Design of a Flying V Aircraft," *17th AIAA Aviation Technology, Integration, and Operations Conference*, 2017, p. 3589.

[26] Okonkwo, P. and Smith, H., "Review of evolving trends in blended wing body aircraft design," *Progress in Aerospace Sciences*, Vol. 82, 2016, pp. 1–23.

[27] Vassberg, J., Sclafani, A., and DeHaan, M., "A wing-body fairing design for the DLR-F6 model: a DPW-III case study," *23rd AIAA Applied Aerodynamics Conference*, 2005, pp. 4730.

[28] Reuther, J. and Jameson, A., "Aerodynamic shape optimization of wing and wing-body configurations using control theory," *33rd Aerospace Sciences Meeting and Exhibit*, 1995, p. 123.

[29] Peigin, S. and Epstein, B., "Aerodynamic optimization of essentially three-dimensional shapes for wing-body fairing," *AIAA journal*, Vol. 46, No. 7, 2008, pp. 1814–1825.

[30] Xu, S., Timme, S., Mykhaskiv, O., and Müller, J., "Wing-body junction optimisation with CAD-based parametrisation including a moving intersection," *Aerospace Science and Technology*, Vol. 68, 2017, pp. 543–551.

[31] Belligoli, Z., *Optimization of a Wing-Body Junction*, Master's thesis, TU Delft, 2015.

[32] Duraisamy, K., Iaccarino, G., and Xiao, H., "Turbulence modeling in the age of data," *Annual Review of Fluid Mechanics*, Vol. 51, 2019, pp. 357–377.

[33] Xiao, H. and Cinnella, P., "Quantification of model uncertainty in RANS simulations: A review," *Progress in Aerospace Sciences*, 2019.

[34] Wilcox, D. C. et al., *Turbulence modeling for CFD*, Vol. 2, DCW industries La Canada, CA, 1998.

[35] Levy, D., Laflin, K., Vassberg, J., Tinoco, E., Mani, M., Rider, B., Brodersen, O., Crippa, S., Rumsey, C., Wahls, R., et al., "Summary of data from the fifth AIAA CFD drag prediction workshop," *51st AIAA Aerospace Sciences Meeting including the New Horizons Forum and Aerospace Exposition*, 2013, p. 46.

[36] Slotnick, J., Khodadoust, A., Alonso, J., Darmofal, D., Gropp, W., Lurie, E., and Mavriplis, D., "CFD vision 2030 study: a path to revolutionary computational aerosciences," 2014.

[37] Glauert, H., "Wind tunnel interference on wings, bodies and airscrews," Tech. rep., AERONAUTICAL RESEARCH COUNCIL LONDON (UNITED KINGDOM), 1933.

[38] Ewald, B., "Wind Tunnel Wall Corrections (la Correction des effets de paroi en soufflerie)," Tech. rep., ADVISORY GROUP FOR AEROSPACE RESEARCH AND DEVELOPMENT NEUILLY-SUR-SEINE (FRANCE), 1998.

[39] Jouhaud, J.-C., Sagaut, P., and Labeyrie, B., "A kriging approach for cfd/wind-tunnel data comparison," *Journal of Fluids Engineering*, Vol. 128, No. 4, 2006, pp. 847–855.

[40] Parish, E. J. and Duraisamy, K., "A paradigm for data-driven predictive modeling using field inversion and machine learning," *Journal of Computational Physics*, Vol. 305, 2016, pp. 758–774.

[41] Singh, A. P. and Duraisamy, K., "Using field inversion to quantify functional errors in turbulence closures," *Physics of Fluids*, Vol. 28, No. 4, 2016, pp. 045110.

[42] Xiao, H., Wu, J.-L., Wang, J.-X., Sun, R., and Roy, C., "Quantifying and reducing model-form uncertainties in Reynolds-averaged Navier–Stokes simulations: A data-driven, physics-informed Bayesian approach," *Journal of Computational Physics*, Vol. 324, 2016, pp. 115–136.

2

Overview of Techniques

Abstract *While Chapter 1 puts this research into context by discussing the societal and technological motivations behind it, this Chapter concludes the prologue of this dissertation by presenting the equations and mathematical techniques used throughout this work. First, I introduce the Navier-Stokes equations and the derivation of their Reynolds-averaged counterpart for compressible flows, which is the physical model used throughout this dissertation. Then I discuss the reasons for modeling the effect of turbulence on the mean flow, and the approximations this step requires. Finally, I explain why aerodynamic shape optimization and data assimilation are challenging high-dimensional 'inverse problems', how they are formulated as gradient-based optimizations, and how the adjoint method allows to significantly speed up the computation of the sensitivities of the objective function with respect to the control parameters.*

2.1   Governing Equations of Fluid Dynamics

The Navier-Stokes equations are a set of coupled, non-linear, partial differential equations that describe the conservation of mass, momentum, and energy of a fluid in a control volume. For example, consider an aerodynamic surface S immersed in a fluid represented by a domain $\Omega \subset \mathbb{R}^3$, with a disconnected boundary divided into a far-field Γ_∞ and a solid wall boundary S as shown in Fig. 2.1. The compressible Navier-Stokes equations can be
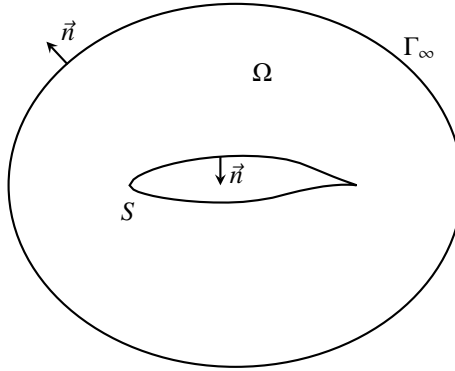
Figure 2.1: General flow domain Ω and boundaries Γ_∞ and S with outward-pointing normals.

written as

$$\partial_t \boldsymbol{U} + \nabla \cdot \boldsymbol{F}^{\mathrm{c}} - \nabla \cdot \boldsymbol{F}^{\mathrm{v}} = \boldsymbol{Q} \quad \text{in } \Omega,\, t > 0, \tag{2.1}$$

where $\boldsymbol{U} = [\rho, \rho v_1, \rho v_2, \rho v_3, \rho E]^\top$, ρ is the fluid density, E is the total energy per unit mass, and $\boldsymbol{v} = (v_1, v_2, v_3) \in \mathbb{R}^3$ is the flow velocity in a Cartesian coordinate system. $\boldsymbol{F}^{\mathrm{c}}$ and $\boldsymbol{F}^{\mathrm{v}}$ are the convective and viscous fluxes, and $\boldsymbol{Q}$ is a generic source term. In this particular

model, convective and viscous physical fluxes are written as

$$\boldsymbol{F}_i^{\mathrm{c}} = \begin{pmatrix} \rho v_i \\ \rho v_i v_1 + p\delta_{i1} \\ \rho v_i v_2 + p\delta_{i2} \\ \rho v_i v_3 + p\delta_{i3} \\ \rho v_i H \end{pmatrix}, \quad \boldsymbol{F}_i^{\mathrm{v}} = \begin{pmatrix} \cdot \\ \tau_{i1} \\ \tau_{i2} \\ \tau_{i3} \\ v_j \tau_{ij} + \kappa_T \partial_i T \end{pmatrix}, \quad i = 1, 2, 3 \tag{2.2}$$

where p is the static pressure, T is the temperature, $H = h + v_i^2/2 = E + p/\rho$ is the total enthalpy, δ_{ij} is the Kronecker delta, κ_T is the thermal conductivity for a calorically perfect fluid. The viscous stresses are of molecular origin and can be compactly written as

$$\tau_{ij} = \mu \left(\partial_j v_i + \partial_i v_j - \frac{2}{3} \partial_n v_n \delta_{ij} \right) = \mu \left(2S_{ij} - \frac{2}{3} \partial_n v_n \delta_{ij} \right), \tag{2.3}$$

with μ being the dynamic viscosity. Assuming the fluid is a perfect gas with a ratio of specific heats $\gamma = \frac{c_p}{c_v}$ and a gas constant R, the pressure is determined from

$$p = (\gamma - 1)\rho \left[E - \frac{1}{2}(\boldsymbol{v} \cdot \boldsymbol{v}) \right], \tag{2.4}$$

and the temperature is given by

$$T = \frac{p}{\rho R}. \tag{2.5}$$

It is difficult to prove that a unique solution to the Navier-Stokes equations exists for particular boundary conditions and, in all cases for which a solution is possible, many of the terms in the equations are zero [1]. For other flows, some terms are unimportant and can be neglected, but this simplification introduces errors. In most cases, even the simplified equations cannot be solved analytically, and one has to use numerical methods.

2.2 Reynolds-averaging

In order to numerically solve the Navier-Stokes equations, we need to employ a discretization method to approximate the PDEs by a system of algebraic equations, which can then be solved on a computer. In principle, the time-dependent, 3D Navier-Stokes equations contain all of the physics of a given turbulent flow. However, their numerical solution is often unfeasible from a computational point of view, thus making the introduction of models a necessity. This is the case for the treatment of turbulent flows.

Most flows encountered in engineering practice are turbulent, and so are those studied in this dissertation. Turbulent flows are 3D, unsteady, chaotic flows characterized by the presence of vortical structures at a broad range of spatial and temporal scales. The smallest scales of turbulence are, typically, many orders of magnitude smaller than the largest ones, and the ratio of largest to smallest scales is proportional to $Re^{3/4}$. Direct Numerical

Simulations (DNS) resolve all the physically relevant scales of turbulence but are limited to relatively low Reynolds numbers by the processing speed and memory of computers. Large Eddy Simulations (LES) only resolve the large energy-carrying scales and have recently started to be used for the simulation of complex test cases thanks to the constant increase in computational power. However, the Reynolds-averaged Navier-Stokes (RANS) simulations are still the industrial workhorses for the simulation of complex geometries in turbulent flows since they employ a turbulence model that approximate the effect of all scales of turbulence on the mean flow thus reducing the required computational time.

Because turbulence consists of chaotic fluctuations of the flow properties, a statistical approach called Reynolds-averaging can be employed to decompose the instantaneous quantities into a mean and a fluctuating part. We assume that the turbulent flow, on average, does not vary with time, i.e. it is stationary. For such flow, an instantaneous variable can be expressed as

$$A = \overline{A} + A' \tag{2.6}$$

where $\overline{A}$ is a time-averaged turbulent quantity obtained as

$$\overline{A}(\boldsymbol{x}, t) = \frac{1}{\mathcal{T}} \int_{-\mathcal{T}/2}^{\mathcal{T}/2} A(\boldsymbol{x}, t + q) dq, \tag{2.7}$$

where $\mathcal{T}$ is a sufficiently long period of time relative to the maximum period of the velocity fluctuations but has to remain small with respect to the time scales of other unsteady effects.

For compressible or variable-density flows, it is common to use an alternative decomposition of the state variables into mean and fluctuating terms know as Favre-averaging [2], where

$$\tilde{A} = \frac{\overline{\rho A}}{\overline{\rho}}, \tag{2.8}$$

such that

$$A = \tilde{A} + A''. \tag{2.9}$$

The application of Favre-averaging to the Navier-Stokes equations returns the compressible Reynolds-averaged Navier-Stokes (RANS) equations. They can be written as:

$$\partial_t \begin{pmatrix} \overline{\rho} \\ \overline{\rho}\tilde{v}_1 \\ \overline{\rho}\tilde{v}_2 \\ \overline{\rho}\tilde{v}_3 \\ \overline{\rho}\tilde{E} \end{pmatrix} + \nabla \cdot \begin{pmatrix} \overline{\rho}\tilde{v}_i \\ \overline{\rho}\tilde{v}_i\tilde{v}_1 + \overline{p}\delta_{i1} \\ \overline{\rho}\tilde{v}_i\tilde{v}_2 + \overline{p}\delta_{i2} \\ \overline{\rho}\tilde{v}_i\tilde{v}_3 + \overline{p}\delta_{i3} \\ \overline{\rho}\tilde{v}_i\tilde{H} \end{pmatrix} - \nabla \cdot \begin{pmatrix} \tilde{\tau}_{i1} - \overline{\rho v_i'' v_1''} \\ \tilde{\tau}_{i2} - \overline{\rho v_i'' v_2''} \\ \tilde{\tau}_{i3} - \overline{\rho v_i'' v_3''} \\ \tilde{v}_j\tilde{\tau}_{ij} + k_T\partial_i\tilde{T} + \overline{\rho v_j'' h''} - \tilde{v}_j\overline{\rho v_i'' v_j''} \end{pmatrix} = \mathbf{0}. \tag{2.10}$$

Aside from replacement of instantaneous variables by mean values, the only difference between the Favre-averaged and instantaneous momentum equations is the appearance of

the correlation $-\overline{\rho v_i'' v_j''}$, which can also be rewritten as $-\bar{\rho} \widetilde{v_i'' v_j''}$ [3, 4]. The component $R_{ij} := \widetilde{v_i'' v_j''}$ is a symmetric tensor commonly referred to as *Reynolds-stress tensor*. The components of R_{ij} are unknown and therefore additional equations must be introduced to close the system. The function of turbulence modeling is to devise approximations for these unknown components in terms of flow properties that are known so that a sufficient number of equations exists (see Section 2.3). Note that also the mean energy equation presents additional unknown terms compared to the instantaneous formulations[1].

In order to study the effect of turbulence on the mean flow, the Reynolds stress tensor can be decomposed into an anisotropic and isotropic part:

$$\widetilde{v_i'' v_j''} = 2k \left(b_{ij} + \frac{\delta_{ij}}{3} \right), \tag{2.11}$$

where $k = \widetilde{v_i'' v_i''}/2$ is the turbulent kinetic energy, $a_{ij} := 2k b_{ij}$ is the anisotropy tensor, and $\frac{2k}{3}\delta_{ij}$ is the isotropic part of the RST. The normalized anisotropy tensor $b_{ij} = a_{ij}/2k$ is a symmetric, trace-free (by construction), positive definite tensor and can be eigen-decomposed such that

$$\widetilde{v_i'' v_j''} = 2k \left(X_{in} \Lambda_{nl} X_{jl} + \frac{\delta_{ij}}{3} \right), \tag{2.12}$$

where X is the matrix of orthonormal right eigenvectors and Λ is diagonal matrix whose elements are ordered such that $\lambda_1 \geq \lambda_2 \geq \lambda_3$, where λ_i is the i-th eigenvalue of the normalized anisotropy tensor. With this representation, b has been transformed to its canonical form such that X identifies the *principal coordinate system*, i.e. the invariant orientations that the linear transformation given by b merely shrink/elongates (and does not rotate) by a factor λ_i. In this sense, the RST can be seen as an ellipsoid with direction of axes given by the columns of X, and length of axes given by λ_i, with k being an additional parameter governing the overall 'size' of the ellipsoid. In short, one can say that the amplitude, shape, and orientation of the RST are given by k, Λ and X, respectively.

From (2.12) it follows that the relation between the eigenvalues of the RST (φ_i) and those of the normalized anisotropy tensor (λ_i) can be written as

$$\lambda_i = \frac{\varphi_i}{2k} - \frac{1}{3}. \tag{2.13}$$

In order to be physically realizable, the diagonal elements of the RST must be non-negative and the Cauchy-Schwartz inequality must hold for the off-diagonal terms [5]. These requirements imply that the following conditions must hold for the normalized anisotropy tensor:

- $b_{ij} \in [-1/3, 2/3]$ for $i = j$,

- $b_{ij} \in [-1/2, 1/2]$ for $i \neq j$.

---

[1]Some extra terms have been neglected as they are usually orders of magnitude smaller than the Reynolds-stress term.

These considerations are useful for describing the limiting behaviors of turbulence at a specific spatial location:

- 1-component turbulence describes a state whereby turbulent fluctuations are present only along one direction. It is present when only one $\varphi_i \neq 0$ or, equivalently, when only one $\lambda_i \neq -\frac{1}{3}$.

- 2-component turbulence is present when two φ_i are non-zero. This implies that the turbulent fluctuations are active in a plane identified by the eigenvectors associated with the non-zero eigenvalues. This is the typical state of wall turbulence.

- 3-component turbulence identifies a situation whereby turbulence fluctuations can exists with various strengths along any direction. In this case, all three φ_i are non-zero. If the three eigenvalues are of the same strength, this state is called *isotropic*.

- The *plane strain* state is obtained when at least one anisotropy eigenvalue is equal to zero. When one or more $\lambda_i = 0$, the turbulence along the direction corresponding to that eigenvalue is due only to isotropic stresses. This implies that turbulence is statistically stationary along the direction of the zero eigenvalue, thus only influencing the solution within the plane perpendicular to this direction.

A powerful tool to visualize the magnitude of the anisotropy is the barycentric map proposed by Banerjee et al. [6]. This mapping leverages the fact that any state of turbulence is a convex combination of its three limiting states. These can be taken to be the vertices $(\boldsymbol{x}_{1c}, \boldsymbol{x}_{2c}, \boldsymbol{x}_{3c})$ of an equilateral triangle arbitrarily located in the Euclidean space. Each state of turbulence can be represented by a point $\boldsymbol{x} = (x, y)$ in the barycentric map as

$$x = C_{1c}x_{1c} + C_{2c}x_{2c} + C_{3c}x_{3c}$$
$$y = C_{1c}y_{1c} + C_{2c}y_{2c} + C_{3c}y_{3c}$$

with $C_{1c} = \lambda_1 - \lambda_2$, $C_{2c} = 2(\lambda_2 - \lambda_3)$, and $C_{3c} = 3\lambda_3 + 1$. The barycentric map is shown in Fig.2.2. States within its boundaries are physically realizable and uniqueness of the mapping is ensured by the constraint $\sum C_{ic} = 1$. This mapping will be used to study how the proposed data assimilation methodologies affect the characteristics of turbulence in specific regions of interest.

2.3 Turbulence Modeling

Closing the RANS equations involves specifying relations between the unknowns and the mean flow quantities in the form of a turbulence model (*closure problem*). Linear eddy viscosity models (EVMs) are the most widespread ones, especially in industry. They are based on the Boussinesq approximation, which models the effect of the anisotropic part of the Reynolds stresses as an added viscosity of the flow such that

$$\widetilde{v_i'' v_j''} - \frac{2}{3}k\delta_{ij} \approx -\frac{\mu_{\text{turb}}}{\rho}\left(\partial_j \tilde{v}_i + \partial_i \tilde{v}_j - \frac{2}{3}\partial_n \tilde{v}_n\right), \tag{2.14}$$
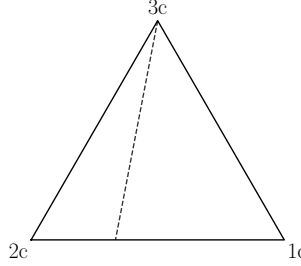
Figure 2.2: The barycentric map domain. The dashed line corresponds to the plane strain limit, the top vertex to the three-component limit, the bottom left vertex to the two-component limit, and the bottom right vertex to the one-component limit.

where $k = \frac{1}{2}\widetilde{v_i'' v_i''}$ is the turbulent kinetic energy, and μ_{turb} is the turbulent (or "eddy") viscosity. The Boussinesq approximation assumes the anisotropic part of the Reynolds-stress tensor is proportional to the mean strain rate tensor $\tilde{S}_{ij} = \frac{1}{2}\left(\partial_j \tilde{v}_i + \partial_i \tilde{v}_j\right)$, thus leaving the turbulent viscosity as the only unknown term. This immediately points out a limitation in the Boussinesq hypothesis, namely that the anisotropy can only be sustained by a local mean strain and is insensitive to the mean rotation rate tensor. Indeed, the eigenvectors of the RST are identically those of the mean strain S_{ij}, and no modification to the magnitude of ν_{turb} will be able to influence the orientation of this tensor [7].

Eddy viscosity models introduce additional transport equations for quantities connected to μ_{turb} in order to obtain a closed system of equations. In this dissertation we focus on the popular Spalart-Allmaras (SA) [8] and the Menter's shear-stress transport (SST) [9] turbulence models. Finally, the turbulent heat-flux vector $\overline{\rho v_j'' h''}$ is usually approximated as

$$\overline{\rho v_j'' h''} = -\frac{\mu_{\text{turb}} c_p}{Pr_{\text{turb}}} \frac{\partial \tilde{T}}{\partial x_j} = -\frac{\mu_{\text{turb}}}{Pr_{\text{turb}}} \frac{\partial \tilde{h}}{\partial x_j} \tag{2.15}$$

where Pr_{turb} is the turbulent Prandtl number which is usually assumed to be 0.90.

2.3.1 Turbulence Modeling Errors

The process of closing the RANS equations with a turbulence model introduces three nested levels of simplification that are responsible for uncertainties and errors in the CFD simulations.

The first level is related to the *structure* of the constitutive relations chosen to compute the Reynolds stress tensor to relate the mean flow quantities to the fluctuating ones. For example, the Boussinesq hypothesis in (2.14) fixes the relationship between the Reynolds stress tensor $\widetilde{v_i'' v_j''}$ and the strain rate S_{ij} to be a function of ν_{turb}, thus reducing the unknown terms from the six components of the RST to the sole ν_{turb}. Furthermore, the

turbulence model is coupled to the RANS equations through an additive modification to the diffusion term in the momentum equation essentially increasing flow mixing. Finally, the turbulent viscosity is assumed to be a function of a set of independent, mean variables which are computed via transport equations. All these assumptions are responsible for what is known as *structural* or *model-form* uncertainty.

The second level of approximation, relates to the choice of a specific *functional* form for the PDEs describing the transport of these independent variables. For example, different $k - \omega$ models have different functional forms for the transport equations.

The third level of simplification is connected to the value assigned to the calibration coefficients within the transport equations and is commonly referred to as *parametric* or *model coefficient* uncertainty. These coefficients are usually determined by enforcing consistency in the prediction of fundamentals flows [10, 11], and therefore are not universal and not appropriate for the simulation of more complex flows. Parametric uncertainty is effectively tackled by re-calibrating the coefficients for a new flow case. However, this process is unable to address the first and second levels of approximation. On the other hand, if the structural uncertainty is corrected, the functional and parametric uncertainties are automatically corrected as well.

The second part of this dissertation is primarily dedicated to the analysis and formulation of methodologies to correct inadequacies introduced in the turbulence model by the first (structural) and second (functional) levels of approximation.

2.4   Inverse Problems

A CFD simulation is a typical example of *forward problem*, which propagates some parameters $\boldsymbol{\theta}$ through a model $\mathcal{B}$ to obtain a quantity $\boldsymbol{d}$:

$$\boldsymbol{d} = \mathcal{B}(\boldsymbol{\theta}). \tag{2.16}$$

By contrast, the focus of this dissertation is on the *inverse problem* of finding $\boldsymbol{\theta}$ given $\boldsymbol{d}$: we want to recover the true value of the parameters $\boldsymbol{\theta}_{\text{true}}$ given some noisy observations $\boldsymbol{d}$. In particular, the main questions we seek to answer are:

- What is the optimum body shape for minimum drag at wing-body junctions? (Chapter 3)

- What is the optimum turbulence modeling corrective term and the optimum Reynolds stress tensor for minimum discrepancy between experimental and numerical data? (Chapter 4)

- What are the optimum wall-interference corrections for a specific wind-tunnel experiment with non-linear effects? (Chapter 5)

The vast majority of inverse problems is *ill-posed*, meaning that a solution either does not exist, or it is not unique, or it is ill-conditioned (i.e. small changes to the input parameters lead to large changes to the solution). One of the most common ways to deal with

ill-posed problems is to add a regularization term, for example by imposing additional constraints that penalize departures of $\boldsymbol{\theta}$ from its presumed value [12]. In this sense, following the Bayesian formalism is a rigorous and convenient approach to formulate regularized inverse problems in a natural way.

The Bayesian approach treats all variables as random by assigning them a probability density function (PDF). The first step of this approach requires to define a statistical model for the forward problem. We note that measured quantities $\boldsymbol{d} \in \mathbb{R}^{N_d}$ (e.g. from an experiment) differ from the true values of those quantities $\boldsymbol{d}_{\text{true}} \in \mathbb{R}^{N_d}$ due to measurement noise and bias. We can model this discrepancy statistically as

$$\boldsymbol{d} = \boldsymbol{d}_{\text{true}} + \boldsymbol{\varepsilon}, \quad \boldsymbol{\varepsilon} \sim \mathcal{N}(\boldsymbol{0}, \sigma_{\text{exp}}^2 \boldsymbol{I}), \tag{2.17}$$

where we assume zero bias, and noise to be independent identically distributed (i.i.d.) normal random variables with known constant standard deviation σ_{exp}. Given some flow-state $\boldsymbol{U} \in \mathcal{U}$, let $\mathcal{B} : \mathcal{U} \to \mathbb{R}^{N_d}$ be a projection which extracts the observed quantities. Under most circumstances – including here – this operator will have negligible error, so that $\boldsymbol{d} = \mathcal{B}(\boldsymbol{U}_{\text{true}}) + \boldsymbol{\varepsilon}$ is a reasonable generalization of equation (2.17) (where $\boldsymbol{U}_{\text{true}} \in \mathcal{U}$ is the true state). However, we don't have access to $\boldsymbol{U}_{\text{true}}$, and approximate it by solving the RANS equations including boundary-conditions

$$\mathcal{R}(\boldsymbol{U}) = 0, \tag{2.18}$$

where $\boldsymbol{U} = \boldsymbol{U}(\boldsymbol{\theta})$ is a function of some parameters $\boldsymbol{\theta}$, so that ultimately we can write $\mathcal{B}(\boldsymbol{\theta}) := \mathcal{B}(\boldsymbol{U}(\boldsymbol{\theta}))$ and our statistical model can be written as

$$\boldsymbol{d} = \mathcal{B}(\boldsymbol{\theta}) + \boldsymbol{\varepsilon}. \tag{2.19}$$

Bayes' theorem states that the posterior probability function of the parameters given data $p(\boldsymbol{\theta}|\boldsymbol{d})$ is proportional to the product of the likelihood $p(\boldsymbol{d}|\boldsymbol{\theta})$ and the prior PDF on the parameters $p_0(\boldsymbol{\theta})$, i.e.

$$p(\boldsymbol{\theta}|\boldsymbol{d}) = \frac{p(\boldsymbol{d}|\boldsymbol{\theta})p_0(\boldsymbol{\theta})}{\int p(\boldsymbol{d}|\boldsymbol{\theta})p_0(\boldsymbol{\theta})d\boldsymbol{\theta}} \propto p(\boldsymbol{d}|\boldsymbol{\theta})p_0(\boldsymbol{\theta}). \tag{2.20}$$

The PDF $p(\boldsymbol{\theta}|\boldsymbol{d})$ does not provide a single parameter vector, but a distribution over the space of possible parameters. Therefore, when a representative vector of $\boldsymbol{\theta}_{\text{true}}$ has to be chosen, it can make sense to identify the one corresponding to the maximum a posteriori (MAP) estimate of $p(\boldsymbol{\theta}|\boldsymbol{d})$. When the observations are independent of each other, the likelihood function can be written as

$$p(\boldsymbol{d}|\boldsymbol{\theta}) = p(d_1|\boldsymbol{\theta}) \cdot p(d_2|\boldsymbol{\theta}) \cdot \ldots p(d_{N_d}|\boldsymbol{\theta}) \tag{2.21}$$

If we also assume that they are normally distributed with standard deviation σ_{exp} and with mean given by $\mathcal{B}(\boldsymbol{\theta})$, we can write

$$p(d_i|\boldsymbol{\theta}) = \frac{1}{\sigma_{\text{exp}}\sqrt{2\pi}} \exp\left\{-\frac{[\mathcal{B}(\boldsymbol{\theta})_i - d_i]^2}{2\sigma_{\text{exp}}^2}\right\} \tag{2.22}$$

and the likelihood function becomes

$$p(\boldsymbol{d}|\boldsymbol{\theta}) = \left(\frac{1}{\sigma_{\text{exp}} \sqrt{2\pi}}\right)^{N_d} \exp\left\{-\sum_{i=1}^{N_d} \frac{[\mathcal{B}(\boldsymbol{\theta})_i - d_i]^2}{2\sigma_{\text{exp}}^2}\right\}. \tag{2.23}$$

In case of uninformative priors, we have that $p(\boldsymbol{\theta}|\boldsymbol{d}) \propto p(\boldsymbol{d}|\boldsymbol{\theta})$, and the MAP estimate can be found by minimizing the exponent of the likelihood function as

$$\min_{\boldsymbol{\theta}} \hat{\mathcal{J}} = \min_{\boldsymbol{\theta}} \sum_{i=1}^{N_d} \frac{[\mathcal{B}(\boldsymbol{\theta})_i - d_i]^2}{2\sigma_{\text{exp}}^2}. \tag{2.24}$$

If, on the other hand, we choose to specify a prior probability density function for our control parameters $\boldsymbol{\theta}$, and we assume they are independent and normally distributed with mean given by $\theta_{j,\text{prior}}$ for $j = 1, ..., N_m$, and standard deviation $\sigma_{j,\theta}$, the MAP can be obtained as

$$\min_{\boldsymbol{\theta}} \mathcal{J} = \min_{\boldsymbol{\theta}} \sum_{i=1}^{N_d} \frac{[\mathcal{B}(\boldsymbol{\theta})_i - d_i]^2}{2\sigma_{\text{exp}}^2} + \sum_{j=1}^{N_m} \frac{(\theta_j - \theta_{j,\text{prior}})^2}{2\sigma_{j,\theta}^2} \tag{2.25}$$

Hence, we see that a regularization term appears because of the specification of a subjective prior distribution on the control parameters and that the least-squares formulation of the optimization problem is equivalent to computing the MAP estimate of the posterior $p(\boldsymbol{\theta}|\boldsymbol{d})$.

These are the principles followed to derive the objective functions for the data assimilation problems of Chapters 4 and 5. Even the drag minimization problem of Chapter 3 can be seen as a particular type of inverse problem where $\mathcal{B}(\boldsymbol{\theta})$ is the drag computed by the operator $\mathcal{B}(\cdot)$, and $d_i = 0$, which is the *ideal* aim for the drag value.

2.5 Adjoint-Based Optimization

In Section 2.4, we demonstrated how an inverse problem formulated with the Bayesian formalism reduces, after making certain approximations, to a deterministic minimization problem. As already mentioned in Chapter 1, optimization problems can be solved using gradient-free or gradient-based methods. Due to the large number of control parameters of the inverse problems in this dissertation (from $O(10^2)$ to $O(10^5)$), gradient-based methods provide the only computationally-affordable technique for their solution. For these methods, the value of the control parameters at optimization iteration $n + 1$ is given by

$$\boldsymbol{\theta}_{n+1} = \boldsymbol{\theta}_n + \psi \boldsymbol{p}_n, \tag{2.26}$$

where ψ is a positive step size, and $\boldsymbol{p}_n$ is a direction along which to search for a new iterate with a lower function value. A line-search algorithm is used to generate a limited number of trial step lengths until it finds one that loosely approximates the minimum of

$$\min_{\psi} \quad \mathcal{J}(\boldsymbol{\theta}_n + \psi \boldsymbol{p}_n). \tag{2.27}$$

At the new point, the search direction and step length are re-computed and the process is repeated.

The *steepest descent* method is a line search method that moves along $\boldsymbol{p}_n = -\nabla \mathcal{J}(\boldsymbol{\theta}_n)$, and can choose the step length ψ in a variety of ways. However, line search methods can use other descent directions than the steepest one. Among these, the *Newton direction* is particularly interesting in that it can be shown that there is a natural step length of 1 associated to it [13], thus requiring adjustments to ψ only when it does not produce a satisfactory reduction in the objective function.

The Newton direction is $\boldsymbol{p}_n = -\nabla^2 \mathcal{J}_n^{-1} \nabla \mathcal{J}_n$ and requires to compute the Hessian of the cost function. Contrary to the steepest descent methods, those using the Newton direction have a fast rate of convergence, although the exact Hessian matrix is not always available in practice. This is why *quasi-Newton* search directions are a valid alternative in that they only require an approximation of the Hessian which is updated after each step to take account of the additional knowledge gained during the optimization iteration. The updates make use of the fact that changes in the gradient provide information about the second derivative of the objective function along the search direction. In this dissertation we make use of two classes of quasi-Newton methods, namely the Sequential Least-Squares Quadratic Programming (SLSQP) [14] and of Limited-Memory Broyden-Fletcher-Goldfarb-Shanno (L-BFGS) [15, 16] algorithms.

Despite the vast amount of different optimization algorithms available, the computation of the gradients has been the real bottleneck of these kinds of techniques for a long time. Indeed, if a first-order finite difference technique were used, the gradient computation would require as many RANS solver evaluations as the number of design variables, thus making the entire optimization time scale with the number of control parameters. The introduction of the adjoint method to fluid dynamics by Pironneau [17], and its extension to aerodynamic shape optimization by Jameson [18–21] opened the doors to a new era for optimization problems in aerodynamics by drastically reducing the computational cost of obtaining the gradients.

The adjoint method is a mathematical technique that allows to compute the gradient of an objective function with respect to *any* number of control parameters at a cost comparable to a single additional RANS solver evaluation. In other words, the cost of computing gradients with the adjoint method is *independent* of the number of control parameters [22], thus making possible the solution of high-dimensional optimization problems.

There are two main approaches for obtaining the adjoint equations, namely the *discrete* and *continuous* approach. The former discretizes the governing equations first, then linearizes them and builds the adjoint equations; the latter first linearizes the governing equations and builds the adjoint problem, and finally proceeds to its discretization. This work makes use of the discrete adjoint technique for computing the gradient of the objective function, and the remainder of this Section presents the discrete adjoint formulation for shape optimization and data assimilation problems.

2.5.1 Shape Optimization

A generic shape optimization problem with a CFD code is a PDE-constrained optimization that can be stated as

$$
\begin{aligned}
\min_{\boldsymbol{\theta}} \quad & \mathcal{J}(\boldsymbol{U}(\boldsymbol{\theta}), \boldsymbol{X}(\boldsymbol{\theta})) \\
\text{s.t.} \quad & \mathcal{R}(\boldsymbol{U}, \boldsymbol{X}) = 0, \\
& \boldsymbol{X} = \mathcal{M}(\boldsymbol{\theta}),
\end{aligned}
\tag{2.28}
$$

where $\mathcal{R}(\boldsymbol{U}, \boldsymbol{X}) = 0$ represent the discrete flow equations, and $\mathcal{M}$ is a mesh deformation operator that maps the design variables $\boldsymbol{\theta}$ to the volume mesh $\boldsymbol{X}$. This problem can also be reformulated as

$$
\min_{\boldsymbol{\theta}} \quad \mathcal{L} = \min_{\boldsymbol{\theta}} \quad \mathcal{J}(\boldsymbol{U}, \boldsymbol{X}) - \boldsymbol{\lambda}^\top \mathcal{R}(\boldsymbol{U}, \boldsymbol{X}) - \boldsymbol{\psi}^\top \left(\mathcal{M}(\boldsymbol{\theta}) - \boldsymbol{X} \right),
\tag{2.29}
$$

where $\mathcal{L}$ is the Lagrangian function and $\boldsymbol{\lambda}$ and $\boldsymbol{\psi}$ are the Lagrange multipliers. Note that $\mathcal{L} = \mathcal{J}$ since the quantities multiplied by the Lagrange multipliers are equal to zero, and the variation of the Lagrangian can be expressed as

$$
d\mathcal{L} = \left(\frac{\partial \mathcal{J}}{\partial \boldsymbol{U}} - \boldsymbol{\lambda}^\top \frac{\partial \mathcal{R}}{\partial \boldsymbol{U}} \right) d\boldsymbol{U} + \left(\frac{\partial \mathcal{J}}{\partial \boldsymbol{X}} - \boldsymbol{\lambda}^\top \frac{\partial \mathcal{R}}{\partial \boldsymbol{X}} + \boldsymbol{\psi}^\top \right) d\boldsymbol{X} - \boldsymbol{\psi}^\top \frac{\partial \mathcal{M}}{\partial \boldsymbol{\theta}} d\boldsymbol{\theta}.
\tag{2.30}
$$

We are interested in computing the gradient $d\mathcal{L}/d\boldsymbol{\theta} = d\mathcal{J}/d\boldsymbol{\theta}$ and therefore the term associated to $d\boldsymbol{U}$ and $d\boldsymbol{X}$ must vanish. This can be done by choosing the Lagrange multipliers such that the following adjoint equations are satisfied:

$$
\frac{\partial \mathcal{J}}{\partial \boldsymbol{U}} - \boldsymbol{\lambda}^\top \frac{\partial \mathcal{R}}{\partial \boldsymbol{U}} = 0 \implies \left(\frac{\partial \mathcal{R}}{\partial \boldsymbol{U}} \right)^\top \boldsymbol{\lambda} = \left(\frac{\partial \mathcal{J}}{\partial \boldsymbol{U}} \right)^\top,
\tag{2.31}
$$

and

$$
\frac{\partial \mathcal{J}}{\partial \boldsymbol{X}} - \boldsymbol{\lambda}^\top \frac{\partial \mathcal{R}}{\partial \boldsymbol{X}} = -\boldsymbol{\psi}^\top,
\tag{2.32}
$$

whereby (2.32) can be solved directly once the solution of (2.31) is known. Hence

$$
d\mathcal{L} = -\boldsymbol{\psi}^\top \frac{\partial \mathcal{M}}{\partial \boldsymbol{\theta}} d\boldsymbol{\theta},
\tag{2.33}
$$

and thus $d\mathcal{L}/d\boldsymbol{\theta}$ is obtained. The discrete adjoint equations can be solved using the same numerical techniques used for iteratively solving the discretized flow equations. The construction of $\frac{\partial \mathcal{R}}{\partial \boldsymbol{U}}$, however, is a grueling task due to the complexity of $\mathcal{R}$ [23]. Hence, we are going to rely on the *algorithmic differentiation* (AD) tool of SU2 [24], which automatically computes the derivatives required to solve the adjoint equations. SU2's discrete adjoint is based on the reformulation of the $\mathcal{R}(\boldsymbol{U}) = 0$ as a fixed-point iteration:

$$
\boldsymbol{U}^{n+1} = \boldsymbol{U}^n - \boldsymbol{B}^{-1} \mathcal{R}(\boldsymbol{U}^n, \boldsymbol{X}) := \mathcal{G}(\boldsymbol{U}^n, \boldsymbol{X}),
\tag{2.34}
$$

where $B \approx \frac{\partial \mathcal{R}(U^n, X)}{\partial U^n}$. If the operator $\mathcal{G}$ is contractive, i.e. $\left\| \frac{\partial \mathcal{G}}{\partial U} \right\| < 1$, the Banach fixed-point theorem [25] admits a unique fixed-point solution U^* such that

$$\mathcal{R}(U^*, X) = 0 \iff U^* = \mathcal{G}(U^*, X). \tag{2.35}$$

Hence, the optimization problem can be reformulated as

$$\min_{\theta} \quad \mathcal{L} = \mathcal{J}(U, X) - \lambda^\top (\mathcal{G}(U, X) - U) - \psi^\top (\mathcal{M}(\theta) - X), \tag{2.36}$$

and the differential of the Lagrangian $\mathcal{L}$ can be expressed as

$$d\mathcal{L} = \left(\frac{\partial \mathcal{J}}{\partial U} - \lambda^\top \frac{\partial \mathcal{G}}{\partial U} + \lambda^\top \right) dU + \left(\frac{\partial \mathcal{J}}{\partial X} - \lambda^\top \frac{\partial \mathcal{G}}{\partial X} + \psi^\top \right) dX - \psi^\top \frac{\partial \mathcal{M}}{\partial \theta} d\theta. \tag{2.37}$$

The adjoint equations are

$$\frac{\partial \mathcal{J}}{\partial U} - \lambda^\top \frac{\partial \mathcal{G}}{\partial U} = -\lambda^\top, \tag{2.38}$$

and

$$\frac{\partial \mathcal{J}}{\partial X} - \lambda^\top \frac{\partial \mathcal{G}}{\partial X} = -\psi^\top. \tag{2.39}$$

Equation (2.38) can be seen as a fixed-point iteration in λ, namely

$$\lambda^{n+1} = \frac{\partial \mathcal{N}}{\partial U}(U^*, \lambda^n), \tag{2.40}$$

where U^* is the numerical solution of (2.35), and $\mathcal{N}$ is a shifted Lagrangian defined as

$$\mathcal{N} = -\mathcal{J}(U, X) + \mathcal{G}^\top(U, X)\lambda. \tag{2.41}$$

If the operator $\mathcal{G}$ is contractive then also $\mathcal{N}$ is contractive:

$$\left\| \frac{\partial}{\partial \lambda} \left(\frac{\partial \mathcal{N}}{\partial U} \right) \right\| = \left\| \frac{\partial \mathcal{G}^\top}{\partial U} \right\| = \left\| \frac{\partial \mathcal{G}}{\partial U} \right\| < 1. \tag{2.42}$$

Thus, according to the fixed-point theorem, (2.40) inherits the same convergence properties of the flow solver. The right-hand side of (2.40) can be computed using algorithmic differentiation applied to the source code of the program that computes $\mathcal{G}$. Finally, the gradient of the objective function with respect to the control parameters can be computed from the converged flow and adjoint solutions using

$$\frac{d\mathcal{L}}{d\theta} = \frac{d\mathcal{J}}{d\theta} = -\psi^\top \frac{\partial \mathcal{M}}{\partial \theta}. \tag{2.43}$$

2.5.2 Data Assimilation

A generic data assimilation problem can be stated as

$$
\begin{aligned}
\min_{\boldsymbol{\theta}} \quad & \mathcal{J}\left(\boldsymbol{U}, \boldsymbol{\theta}\right) \\
\text{s.t.} \quad & \mathcal{R}\left(\boldsymbol{U}, \boldsymbol{\theta}\right) = 0,
\end{aligned}
\tag{2.44}
$$

where $\mathcal{J}$ is a cost function estimating the error of the results of the numerical model from a sparse set of, usually experimental, observations, and $\boldsymbol{\theta}$ is a vector of control parameters to be calibrated whose dimension is often many orders of magnitude higher than the number of observations. The aim of the data assimilation is to exploit the information provided by the experimental observations to calibrate the parameters of the model such that the cost function is minimized.

The Lagrangian associated to this optimization problem is $\mathcal{L} = \mathcal{J}\left(\boldsymbol{U}, \boldsymbol{\theta}\right) - \boldsymbol{\lambda}^{\top} \mathcal{R}\left(\boldsymbol{U}, \boldsymbol{\theta}\right)$, and its variation is given by

$$
d\mathcal{L} = \left(\frac{\partial \mathcal{J}}{\partial \boldsymbol{U}} - \boldsymbol{\lambda}^{\top} \frac{\partial \mathcal{R}}{\partial \boldsymbol{U}}\right) d\boldsymbol{U} + \left(\frac{\partial \mathcal{J}}{\partial \boldsymbol{\theta}} - \boldsymbol{\lambda}^{\top} \frac{\partial \mathcal{R}}{\partial \boldsymbol{\theta}}\right) d\boldsymbol{\theta},
\tag{2.45}
$$

and the adjoint equations are the same as in (2.31). The computation of the sensitivity of $\mathcal{J}$ with respect to the control parameters is obtained by first solving the adjoint equations and finding the value of the adjoint variables $\boldsymbol{\lambda}$, and then substituting it into (2.45). The partial derivatives in these expressions can be computed using algorithmic differentiation as described in the previous section. The adjoint equations are independent of the design variables and so is the computational cost of solving them, thus making it possible to work with a large number of control parameters.

In this dissertation, both the geometric and non-geometric sensitivities will be computed using the open-source CFD solver SU2 [26, 27]. SU2 features a robust, flexible, algorithmic differentiation tool [28] that automatically computes the derivatives necessary for the solution of the adjoint equations, thus conveniently minimizing the required code modifications whenever a new type of control parameter or objective function is implemented. This feature will turn out to be useful in Chapters 4 and 5, where the development of the data assimilation framework will require to define new control parameters and new objective functions, and implement them in SU2's code.

References

[1] Ferziger, J. H. and Peric, M., *Computational methods for fluid dynamics*, Springer Science & Business Media, 2012.

[2] Hirsch, C., *Numerical computation of internal and external flows: The fundamentals of computational fluid dynamics*, Elsevier, 2007.

[3] Wilcox, D. C. et al., *Turbulence modeling for CFD*, DCW industries La Canada, CA, 1998.

[4] Gatski, T. B. and Bonnet, J.-P., *Compressibility, turbulence and high speed flow*, Academic Press, 2013.

[5] Girimaji, S. S., "A new perspective on realizability of turbulence models," *Journal of Fluid Mechanics*, Vol. 512, 2004, pp. 191–210.

[6] Banerjee, S., Krahl, R., Durst, F., and Zenger, C., "Presentation of anisotropy properties of turbulence, invariants versus eigenvalue approaches," *Journal of Turbulence*, 2007.

[7] Emory, M. A., *Estimating model-form uncertainty in Reynolds-averaged Navier-Stokes closures*, Ph.D. thesis, Stanford University, 2014.

[8] Spalart, P. and Allmaras, S., "A one-equation turbulence model for aerodynamic flows," *30th aerospace sciences meeting and exhibit*, 1992.

[9] Menter, F. R., "Two-equation eddy-viscosity turbulence models for engineering applications," *AIAA journal*, Vol. 32, No. 8, 1994, pp. 1598–1605.

[10] Duraisamy, K., Iaccarino, G., and Xiao, H., "Turbulence modeling in the age of data," *Annual Review of Fluid Mechanics*, Vol. 51, 2019, pp. 357–377.

[11] Xiao, H. and Cinnella, P., "Quantification of model uncertainty in RANS simulations: A review," *Progress in Aerospace Sciences*, 2019.

[12] Aster, R. C., Borchers, B., and Thurber, C. H., *Parameter estimation and inverse problems*, Elsevier, 2018.

[13] Nocedal, J. and Wright, S., *Numerical optimization*, Springer Science & Business Media, 2006.

[14] Boggs, P. T. and Tolle, J. W., "Sequential quadratic programming," *Acta numerica*, Vol. 4, 1995, pp. 1–51.

[15] Liu, D. C. and Nocedal, J., "On the limited memory BFGS method for large scale optimization," *Mathematical programming*, Vol. 45, No. 1-3, 1989, pp. 503–528.

[16] Byrd, R. H., Lu, P., Nocedal, J., and Zhu, C., "A limited memory algorithm for bound constrained optimization," *SIAM Journal on Scientific Computing*, Vol. 16, No. 5, 1995, pp. 1190–1208.

[17] Pironneau, O., "Optimal shape design for elliptic systems," *System Modeling and Optimization*, Springer, 1982, pp. 42–66.

[18] Jameson, A., "Aerodynamic design via control theory," *Journal of scientific computing*, Vol. 3, No. 3, 1988, pp. 233–260.

[19] Jameson, A., "Optimum aerodynamic design using CFD and control theory," *12th Computational Fluid Dynamics Conference*, 1995, p. 1729.

[20] Jameson, A., "Re-engineering the design process through computation," *Journal of Aircraft*, Vol. 36, No. 1, 1999, pp. 36–50.

[21] Jameson, A., Martinelli, L., and Pierce, N., "Optimum aerodynamic design using the Navier–Stokes equations," *Theoretical and computational fluid dynamics*, Vol. 10, No. 1-4, 1998, pp. 213–237.

[22] Peter, J. E. and Dwight, R. P., "Numerical sensitivity analysis for aerodynamic optimization: A survey of approaches," *Computers & Fluids*, Vol. 39, No. 3, 2010, pp. 373–391.

[23] Dwight, R. P. and Brezillon, J., "Effect of approximations of the discrete adjoint on gradient-based optimization," *AIAA journal*, Vol. 44, No. 12, 2006, pp. 3022–3031.

[24] Albring, T. A., Sagebaum, M., and Gauger, N. R., "Efficient aerodynamic design using the discrete adjoint method in SU2," *17th AIAA/ISSMO multidisciplinary analysis and optimization conference*, 2016, p. 3518.

[25] Banach, S., "Sur les opérations dans les ensembles abstraits et leur application aux équations intégrales," *Fund. math*, Vol. 3, No. 1, 1922, pp. 133–181.

[26] Palacios, F., Alonso, J., Duraisamy, K., Colonno, M., Hicken, J., Aranake, A., Campos, A., Copeland, S., Economon, T., Lonkar, A., et al., "Stanford university unstructured (su 2): an open-source integrated computational environment for multiphysics simulation and design," *51st AIAA Aerospace Sciences Meeting including the New Horizons Forum and Aerospace Exposition*, 2013, p. 287.

[27] Economon, T. D., Palacios, F., Copeland, S. R., Lukaczyk, T. W., and Alonso, J. J., "SU2: An open-source suite for multiphysics simulation and design," *Aiaa Journal*, Vol. 54, No. 3, 2015, pp. 828–846.

[28] Sagebaum, M., Albring, T., and Gauger, N. R., "High-performance derivative computations using codipack," *ACM Transactions on Mathematical Software (TOMS)*, Vol. 45, No. 4, 2019, pp. 1–26.

3

The Anti-Fairing

Abstract   *Chapter 1 briefly discussed the potential of aerodynamic shape optimization (ASO) to create novel designs. The present Chapter puts this notion into practice by using ASO to create a new geometry for reducing drag at a generic wing/fuselage junction. The new design is called "anti-fairing", for it is entirely different from the typical fairings used on modern airplanes. After introducing the optimization setup and process, the anti-fairing design is validated through a wind-tunnel experiment and additional RANS simulations. Furthermore, its performance in terms of drag reduction is estimated with near-field and far-field techniques and compared to that of two leading-edge fairings.*

3.1   Introduction

Junction flows occur when a boundary layer developing on a smooth wall encounters an obstacle attached to the same surface and separates due to the adverse pressure gradient generated by the obstacle [1]. These flows are present in many aerodynamic and hydro-dynamic situations, e.g. at a wing/fuselage or wing/nacelle intersection on an aircraft, within a turbine or when the water of a river impinges on a bridge pylon. This Chapter focuses on junction flows in aeronautical applications, and wing/body junctions in particular. These kinds of phenomena are characterized by two different types of secondary flow: the horseshoe vortex (HSV) and the corner vortex (CV). These are responsible for the separation of the flow near the leading edge and trailing edge of the obstacle, respectively, thus contributing to the drag with a component called *interference drag*, which can account for up to ten percent of the total drag of a modern aircraft [2]. Indeed, the total drag of a wing/body configuration is more than the sum of the wing drag and body drag when considered separately [3]. This additional component is due to the interaction of the two boundary layers developing on the wing and the body and should be mitigated to improve aerodynamic performance and, consequently, reduce fuel consumption.

Of the two flow phenomena characterizing junction flows, the horseshoe vortex is always present in both laminar and turbulent flows, while the conditions under which corner separation appears have not been fully understood yet [4–6]. Of the two, the HSV is usually the one that has the most significant impact on the drag unless a vast separation area at the corner is present. This is why several flow-control techniques to reduce the impact of the HSV have been developed in the past. Among the active flow-control techniques, boundary-layer suction could reduce the source of vorticity generating the HSV [7], as well as the Reynolds stresses [8], and the size of the vortex [9]. However, it was noted that suction increases the wall shear stresses by creating higher velocity gradients close to the wall, thus potentially contributing to increasing the drag. Besides, the energy required to run an active flow-control system further reduces the theoretical maximum net energy saving.

Several passive drag-reducing techniques for this kind of flow have been tested as well. McGinley [10] used vortex generators downstream a wing/flat-plate junction to produce counter-rotating vortices that reduce the circulation in the wakes of the HSV legs by interacting with them. However, it might not be beneficial to completely remove the horseshoe vortex since it pumps high-momentum fluid into the wake, thus aiding its turbu-

lent diffusion. A number of studies focused on various designs of leading-edge fillets [11–16]. These devices can reduce the adverse pressure gradient generated by the obstacle, thus preventing leading-edge separation, reducing peak turbulence levels, and, in some cases, promoting relaminarization of the flow over the wing. However, it remains unclear whether and by how much the total drag at the junction is reduced [1]. Other notable approaches are those by LaFleur & Langston [17], who experimentally designed a fairing with the ice-formation method which was capable of reducing the drag of a cylinder/flat-plate configuration by 18%, and of Kairouz and Rahai [18] where the strength of the horseshoe vortex was reduced by positioning riblets on the flat plate upstream of a wing.

Modern transport aircraft use a fairing around the junction to obtain streamlined flow with almost no separation [19]. Li et al. [20] also showed that a fairing could improve the lift-to-drag ratio at several angles of attack. Peigin and Epstein [21] reduced the wave drag in transonic conditions by optimizing the existing fairing of a business jet, a result that showed that improvements in the design of this area of the aircraft are still possible. Also Song and Li [22] reduced the total drag of a wing-fuselage configuration by means of numerical optimization. Dwight & Brezillon [23] obtained an interesting-looking fairing design as a result of an optimization of a DLR-F6 wing-body configuration. The fairing reduced the drag of the configuration by 7.1% and looked like a double dent in the fuse-lage. Also Xu et al. [24] performed ASO on the same configuration using a CAD-based parameterization and allowed only outward deformations of the fuselage. Their result also confirms the potential of ASO: their optimized design achieved a drag reduction of 4.4%.

This work draws inspiration by the peculiar double-dented geometry in Dwight & Brezillon [23] and aims at reproducing their results on a simpler geometry to study its main characteristics. This was initially attempted in Belligoli [25] by optimizing a wing/flat-plate junction at subsonic conditions. The optimized geometry had the shape of a very deep dent wrapped around the wing but no final conclusion on whether it effec-tively reduced the drag could be drawn. The present work builds on the lessons learned in [25] and re-performs a similar optimization with the aim of obtaining a shallower design that can be manufactured and tested in a wind-tunnel experiment, and with the additional objective of thoroughly studying the drag-reducing capabilities of the optimized design.

For this purpose, the same starting configuration and flow conditions as in van Oud-heusden et al.'s [13] is selected for the optimization, consisting of a symmetrical NACA 0015 wing, perpendicularly attached to a flat-plate at an angle of attack $\alpha = 0°$. This is done in order to compare the effects of the numerically-optimized geometry with those of van Oudheusden et al.'s leading-edge fairings. Contrary to what is typically done for shape optimizations of wing-body junctions, the optimizer is allowed to modify only the shape of the flat plate in the spanwise direction, while keeping the wing shape fixed. This is done in order to investigate the effect of changes in the body geometry on the junction drag. The optimization produced a design that was able to reduce the interference drag and looked similar but with significant differences to that of Brezillon and Dwight. This new shape is named the *anti-fairing* (AF). In order to validate the numerical optimization results, to study the effect of the anti-fairing on the flow, and to check whether a system-atic drag reduction is obtained, an experimental and an additional numerical study are

carried out. The AF is tested in a wind-tunnel experiment, and the velocity field in the wake of the junction configuration is compared with those of the leading-edge fairings. The experiments produce different incoming boundary layers than that used for numerical optimization, thus preventing an accurate quantitative comparison with numerical optimization. A new set of more accurate CFD simulations was only considered prudent in order to verify that the same features could also be obtained from the numerical calculations when all the configurations share the same incoming boundary layer. We use the latter results to study the influence of the AF on the flow around the entire junction area, and explain its working mechanism.

This Chapter is structured as follows: Section 3.2 details the setup and results of the optimization. Section 3.3 describes the experimental setup and its most insightful results. In Section 3.4, the details of the second set of numerical simulations are presented and linked to the experimental results. The experimental and numerical results are then used in Section 3.5 to estimate the drag reduction of the various geometries analyzed and to formulate a proposal of the working mechanism of the anti-fairing. Finally, Section 3.6 presents the conclusions of this work and recommendations for future studies.

3.2 Aerodynamic Shape Optimization

In this study, ASO is used to minimize the drag of a junction configuration by modifying its shape. The optimization problem can be stated as in equation (2.28), with $X(\theta) = \mathcal{M}(\theta)$ being a mapping from the design variables θ to the volumetric mesh coordinates X. The objective function to minimize is $\mathcal{J} = c_D$, where $c_D = \frac{D}{\frac{1}{2}\rho_\infty U_\infty^2 A_{\text{ref}}}$, with D being the total drag force, and A_{ref} being a reference area whose value is kept constant throughout the optimization.

3.2.1 Numerical Setup

The geometry under consideration comprises a symmetrical NACA 0015 semi-infinite wing at zero angle of attack, perpendicularly attached to a flat plate. The wing chord is $c = 0.75$ m, its thickness is $T = 0.1125$ m, the flow speed is $U_\infty = 20$ m/s, and ambient air conditions are assumed. Note that from now on, all spatial dimensions will be normalized with the wing thickness T, as commonly done in wing/body junction studies, and that the origin of the coordinate system is at the intersection between the wing leading-edge and the flat plate. A structured mesh is chosen for the numerical simulation of this geometry, and the location of the leading edge of the flat plate is such that the momentum thickness at $x/T = -2.313$ is the same as in van Oudheusden et al. [13].

As Fig. 3.1 shows, a rectangular box is chosen as the domain and, since the configuration has a vertical symmetry plane, only half of the domain is meshed to save computational resources. A symmetry boundary condition is imposed at the xz plane, no-slip boundaries are specified at the wing and flat plate (whose leading-edge extends up to the inflow of the domain), and far-field boundary conditions are specified in the rest of the domain. These are placed 40 chord lengths away from the wing in order to avoid

(a) Details of the structured computational mesh in the junction area. FFD box (red) and FFD control points (green) chosen for the optimization.

(b) Close-up of the area where the drag reduction is being monitored.
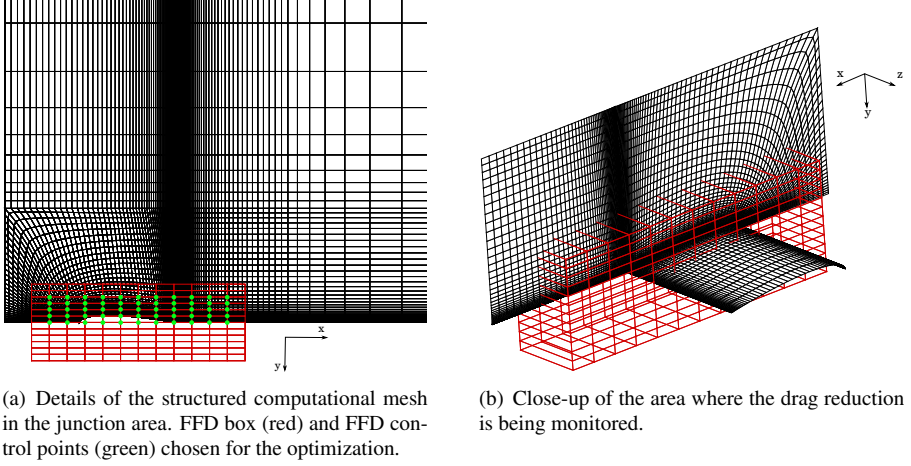
Figure 3.1: Details of the 1.6M-point mesh.

blockage effects and reflections of the characteristic waves back into the domain. After a grid-convergence study, we select a mesh with 1.6 million points and $y^+ \approx 1$. Fig. 3.1(a) shows a close-up of the mesh in the junction area. We discretize the convective fluxes using Roe's second-order scheme [27], and the gradients using the Green-Gauss theorem. Implicit local time stepping is used to converge the simulation to a steady-state solution, and the linear system is solved using the iterative GMRES method with a tolerance of $O(10^{-6})$ on the maximum error. The one-equation Spalart-Allmaras model is chosen as the turbulence model [28]. Several studies tested the performance of this turbulence model in junction flow cases [29–31], finding it able to predict quantities such as the size of the HSV footprint on the body, but unable to estimate the turbulence quantities accurately. This may affect the optimization result, hence the need for experimental tests of the optimized geometry.

3.2.2 Surface Deformation with FFD

Using the mesh nodes on the surface as design variables may lead to discontinuous solutions because all nodes can move independently. Hence, the Free-Form Deformation (FFD) technique [32] is adopted to smoothly deform the junction area. For this, the design area is encapsulated into a box defined by a lattice of control points. An incremental displacement of a point $\boldsymbol{x}_{surf} = (x_s, y_s, z_s)$ on the surface enclosed by the FFD box is given by:

$$\Delta \boldsymbol{x}_{surf} = \sum_{i=0}^{l} \sum_{j=0}^{m} \sum_{k=0}^{n} B_i^l(s) B_j^m(t) B_k^n(u) \Delta \boldsymbol{p}_{ijk}, \tag{3.1}$$

where (s, t, u) is the local coordinate system of the FFD parallelpiped region, $\Delta\boldsymbol{p}_{ijk}$ is the displacement of a certain FFD control point, $B_i^l(s)$, $B_j^m(t)$, and $B_k^n(u)$ are the i-th, j-th, k-th Bernstein polynomials of degree l, m, n, respectively. The degree of the chosen Bernstein polynomials is proportional to the number of FFD control points [33]. If the latter are chosen as design variables, any deformation of the FFD box will result in a smooth deformation of the surface points enclosed in it. In this study, a FFD box was wrapped around the junction area delimited by $-3.5 \leq x/T \leq 11.7$, $-2.7 \leq y/T \leq 2.7$, $-1.8 \leq z/T \leq 1.8$, whereby the leading edge of the wing is chosen as the origin of the coordinate system. The extension of the FFD box in the x and y direction is chosen to realistically represent the area where fairings are usually located on transport aircrafts, whereas the extension in the z can be arbitrarily chosen as long as the FFD box encapsulated the geometry to be deformed.

Equidistant control points in each direction are used to construct the FFD box. Hence, in order to have a sufficient number of control points mapping the area of interest, we select Bernstein polynomials of degree 13, 13, and 2 for the x, y, and z directions, respectively. Of the 338 control points generated, we select as design variables only the fifty shown in Fig. 3.1(a). They are twice as many as in Brezillon & Dwight [23], with a minimum distance between control points of $1.24T$ and $0.44T$ in the x and y direction respectively.

Finally, the drag coefficient is chosen as the objective function, and it is monitored only on the portion of the wing/body junction shown in Fig. 3.1(b). The CFD solver computes the drag force using the classical integration of pressure and viscous forces on the monitored surfaces.

The distinguishing feature of this optimization lies in the deformation constraints imposed on the geometry. In order to study the influence of the body shape on the drag, we keep the wing shape fixed (by not mapping its points onto the FFD box) and allow the flat plate to deform only in the spanwise direction (by constraining the movement of the FFD control points chosen as design variables only in the z direction). A Cauchy convergence criterion is adopted for the flow and adjoint solvers, with a tolerance of 10^{-5} over 500 iterations. For the optimization, we impose no constraints on the lift or other quantities. The sequential least-squares quadratic programming (SLSQP) algorithm is used in combination with the direct and adjoint solutions generated by SU2.

3.2.3 Optimization Results

Figure 3.2(a) shows the convergence history of the optimization: after seventeen flow evaluations and three gradient evaluations, the optimizer reduced the drag by about 16%. The spike in the drag coefficient at iteration 7 is due to a substantial change in the geometry of the junction caused by a too-large step size during the line-search part of the SLSQP optimization routine.

As Fig. 3.2(b) and 3.3 show, the optimized geometry has the form of a relatively shallow, concave dent in the flat plate. It begins $3.5T$ upstream of the wing's leading edge and terminates $5T$ downstream of the trailing edge. It has a half-width of $2.7T$ and a maximum depth of $0.21T$, which is approximately twice the boundary layer thickness at

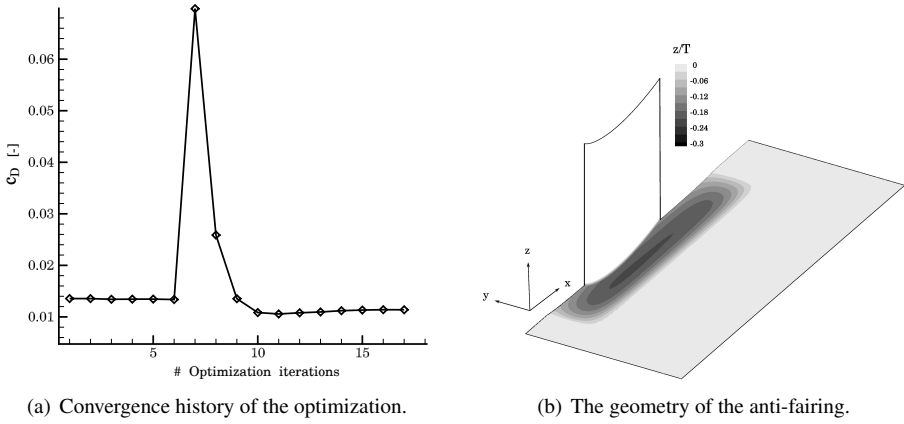(a) Convergence history of the optimization.   (b) The geometry of the anti-fairing.

Figure 3.2: Details and results of the optimization.

$x/T = -2.313$. The FFD box size constrains the dimensions of the optimized configuration. Whether a larger FFD box would produce a similar geometry or not is a question for future optimization studies. The optimized shape is the opposite of that of the fairings currently used on commercial aircraft, and it is not the result of an attempt to reduce wave drag like area-ruled geometries (since $M_\infty = 0.06$). This is why this design, considered entirely novel, was named *anti-fairing* (AF). The AF is somewhat similar to the fairing of Brezillon and Dwight [23] but presents significant differences, namely, it is not a double dent but a single one, as observed in Fig. 3.2(b), and appears to be considerably shallower. Most likely, this is due to the differences in geometries and flow conditions.

Performing a RANS gradient-based optimization requires a non-negligible amount of computational time and resources. For this reason, the computational mesh was fine enough to capture the main flow features and bound the error associated with the numerical discretization of the domain. However, the primary source of error in the RANS computation is due to the approximation of the Reynolds stress tensor computed by the SA turbulence model. Because of this, it is possible that some characteristics of the AF flow were not captured. As a consequence, an experimental investigation of the anti-fairing under similar flow conditions is required in order to validate the observed drag reduction. This is the topic of Section 3.3.

3.3   Experiments

An experiment is carried out in the Low Turbulence Tunnel (LTT) of the Delft University of Technology in the Netherlands for validating the results of the numerical optimization. The LTT is a subsonic ($U_{MAX} = 120$ m/s) low-turbulence ($I = 0.015\%$ at $U_\infty = 20$ m/s), closed-loop wind tunnel with a test section of 1.25 m $\times$ 1.80 m $\times$ 2.6 m in height, width and length, respectively. The tunnel is furnished with seven anti-turbulence screens and
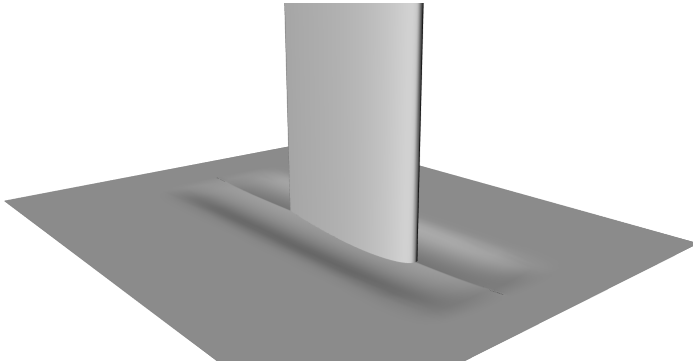
Figure 3.3: CAD representation of the anti-fairing.

has a contraction ratio of 17:1. This experiment aims to estimate the drag reduction of the AF from Section 3.2 with respect to the baseline (BS), and compare its performance to conventional fairings such as the small (SF) and large (LF) leading-edge fairings designed by van Oudheusden et al. [13]. We select stereo PIV as the main measurement technique for this investigation in order to estimate the mean stream-wise velocity field in the wake of the junction.

The NACA 0015 wing is perpendicularly mounted on a flat plate 1.75 m long by 0.65 m wide (block 1 in Fig. 3.4(a)), which, in turn, could be inserted into a larger flat plate (block 2) extending to the wind tunnel walls, such that the wing is aligned with the wind-tunnel centerline. The total size of block 2 was 2.6 m × 1.5 m, and its leading-edge was elliptical. Two versions of block 1 are milled, one in the shape of the flat plate and one in the shape of the anti-fairing (Fig. 3.4(b)). The configuration is lifted from the wind tunnel bottom wall by four wooden beams in order to have a fresh boundary layer starting at the flat plate leading-edge. Due to geometrical constraints (see Appendix A), the height from the wind-tunnel bottom wall of the AF and LF/SF flat plates are different. The distance between the NACA 0015 leading edge and the beginning of the flat plate is 0.398 m, the wing chord is $c = 0.75$ m, and its span $b = 0.9$ m. An interchangeable piece at the wing leading-edge easily allows to obtain van Oudheusden et al.'s LF and SF configurations, as shown in Fig. 3.5(a). We test these configurations at different free-stream flow speeds from $U_\infty = 15$ m/s to $U_\infty = 30$ m/s with intervals of 5 m/s, and at an angle of attack of $\alpha = 0°$.

A stereoscopic PIV (sPIV) setup is used, consisting of two LaVision Imager PRO LX 16MP high-speed cameras with 200 mm focal length Nikon AI MF lenses. The camera resolution is 4872 × 3248 pixels, and the pixel size is 7.4 × 7.4 μm. The snapshot frequency is adjusted according to the flow speed and varied between 20 kHz and 59 kHz. The seeding generator is a SAFEX Fog 2010+ generating droplets with a mean diameter of 1 μm. The particles are illuminated by a 2 mm-thick laser sheet generated by a Quantum Evergreen 200 laser. In order to avoid large uncertainties near the illuminated profile due to surface reflections, the image intensity is calibrated using white-image subtraction
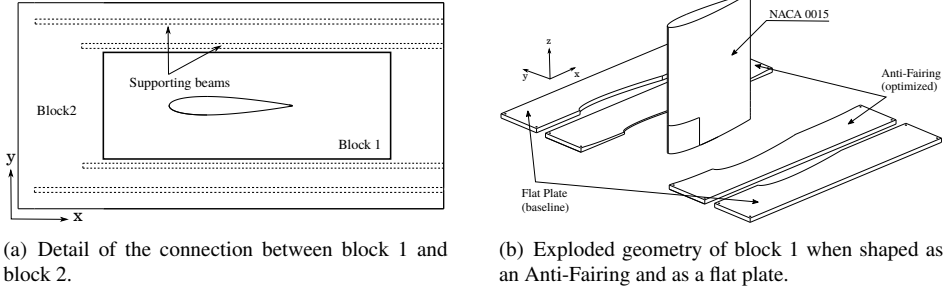
(a) Detail of the connection between block 1 and block 2.

(b) Exploded geometry of block 1 when shaped as an Anti-Fairing and as a flat plate.

Figure 3.4: Details of the geometry used for the experiments.

(a) Different shapes of the interchangeable piece at the wing leading-edge. The dimensions are expressed in millimeters.

(b) Stereo-PIV set-up as seen from a view downstream of the wing trailing-edge.
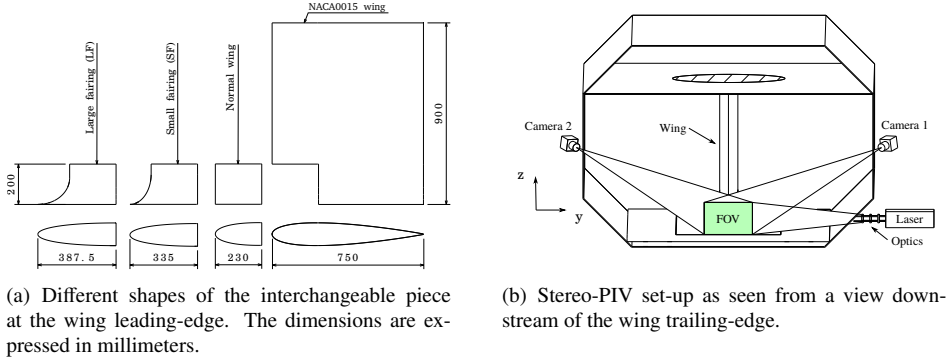
Figure 3.5: Details of the experimental set up.

and background image subtraction. With this setup, we obtain a field of view (FOV) of 0.3 m × 0.2 m in the wake of the flow at $x/T = 5.33$ from the wing's trailing edge. Note that, at this location, the plate is completely flat for all configurations tested. Finally, 500 image pairs per configuration are acquired in order to obtain the mean flow fields. Figure 3.5(b) shows a sketch of the experimental setup.

We compute the velocity vector using the software package DaVis provided by LaVision. Note that only the results for a free-stream velocity of 20 m/s are reported here, given that the flow fields for the other velocities do not present substantial differences.

The wall boundary-layer profile is measured at $x/T = -2.313$ with a pressure probe. Figure 3.6 shows that the measured boundary layer for the AF is thicker than the one measured for LF and SF, which in turn is thicker than the one used in the CFD. This could be due to the effect of blockage underneath the flat plate, forcing some of the tunnel wall boundary layer onto the top side of the ground plane. This situation prevents exact comparisons between the drag reduction of the experiment and that computed with the numerical optimization. The discrepancy between the boundary layers of the AF config-
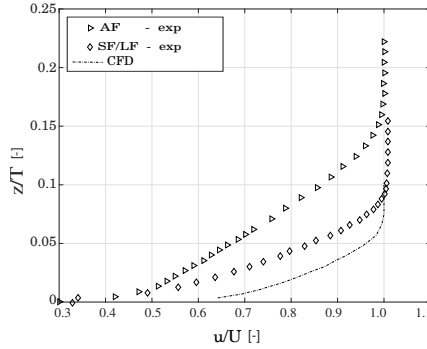
Figure 3.6: Boundary layer profile at $x/T = 2.313$ upstream of the wing leading-edge for the experiment and the CFD.

uration and the SF/LF configurations is justified by the use of different setups for the AF and the LF/SF as explained in Appendix A. Nevertheless, the influence of the AF on the junction flow can still be compared to that of the corresponding baseline geometry, and similarly for the SF/LF.

Figure 3.7(a) shows the velocity field in the wake of the wing for the BS and AF. The velocity fields are normalized with the corresponding free-stream velocity U_∞, calculated by taking the mean of the free-stream velocity area in the PIV images. The velocity deficit at $y/T = 0$ over the entire vertical length of the field is due to the wake of the NACA 0015 wing. This wake is of the same size for both configurations. The legs of the horseshoe vortex are characterized by a lump in the velocity deficit distribution at approximately the same location between $y/T = -0.5$ and $y/T = -1$, with the one of AF being slightly further from the vertical symmetry plane. We link this observation to the considerations of Fleming et al. [34], who correlated the distance between the vortex legs with increasing values of $MDF = Re_\theta Re_T$, where θ is the momentum thickness. Since the wing thickness T does not change, and the free-stream velocity is the same in both configurations, it is possible to conclude that one of the effects of the AF is to increase the momentum thickness of the attached boundary layer upstream of the wing's leading edge. Further away from the wing in the transversal direction, the influence of the horseshoe vortex reduces, and the flat plate boundary layer is recovered outside the borders of the PIV domain.

Figure 3.7(b) compares the stream-wise velocity fields in the wake of the LF and SF configurations. For the former, the footprint of the horseshoe vortex in the wake is almost undetectable, while the latter only reduces the HSV effect on the boundary layer flow, without removing it completely. These effects agree with the expected working mechanism of classical leading-edge fairings, whose design aims at removing the horseshoe vortex by reducing the leading-edge pressure gradient responsible for its formation.

It is clear from the experimental results that both the anti-fairing and the leading-edge fairings have strong but different effects on the junction-flow dynamics. While the

(a) Comparison of baseline (left) and anti-fairing (right) effect on the wake.

(b) Comparison of large-fairing (left) and small-fairing (right) effect on the wake.
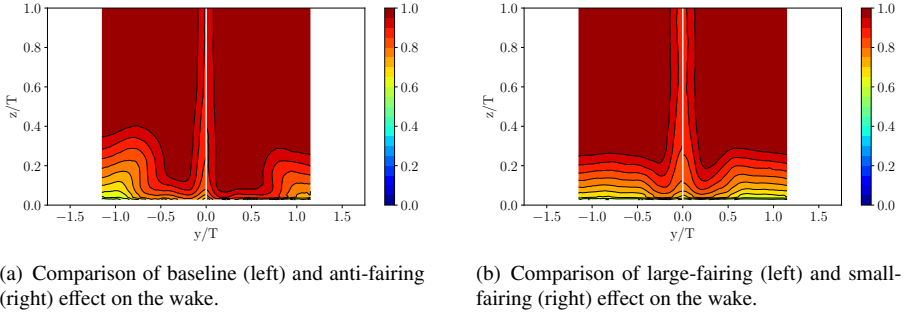
Figure 3.7: Mean stream-wise velocity field at $x/T = 5.33$ downstream of the trailing edge as obtained from stereo-PIV. The white areas in the pictures is where outliers have been removed.

leading-edge fairings act by preventing the formation of the horseshoe vortex, the anti-fairing does not act against it but instead seems to create a situation that prevents excessive momentum loss in the junction. The availability of experimental results in a confined region in the wake, however, does not allow to draw conclusions on the flow behavior over the whole domain. Because of this and the need for comparing the behavior of the various configurations when they share the same upcoming boundary layer, we carry out a new set of RANS simulations in the next Section.

3.4   RANS Simulations

A new set of numerical simulations is carried out in order to compare the effect of the geometries under study when they share the same boundary layer far upstream of the wing leading-edge. Furthermore, CFD makes it possible to obtain data everywhere in the domain, thus providing a complete picture of the flow dynamics around the junction area.

The geometry under investigation is similar to the one used in the optimization and the experiments. The NACA 0015 wing chord is still 0.75 m, its span 0.9 m, and the flat-plate width 1.5 m. The distance between the flat-plate start and the wing leading-edge is 0.65 m, and that from the wing trailing-edge to the flat-plate end is 4.5 m, larger than in the experiments in order avoid having an outlet boundary condition too close to the object. The symmetry of the configuration was exploited by meshing only half of the domain and applying a symmetry boundary condition at the vertical symmetry plane. No-slip boundary conditions were applied at the wind tunnel walls and the wing, the static pressure was set at the subsonic outlet, and a velocity profile was set at the inlet of the domain as shown in Fig. 3.8.

For the grid generation and the simulations, we use STAR-CCM+ instead of SU2 to check the portability of the optimization results across different grids and different CFD codes. A hybrid mesh is used, with structured, hexahedral cells in the boundary layer
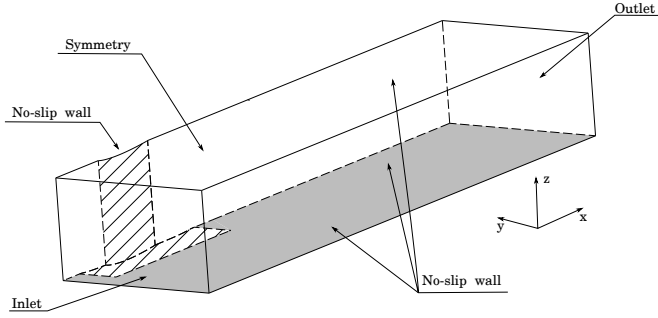
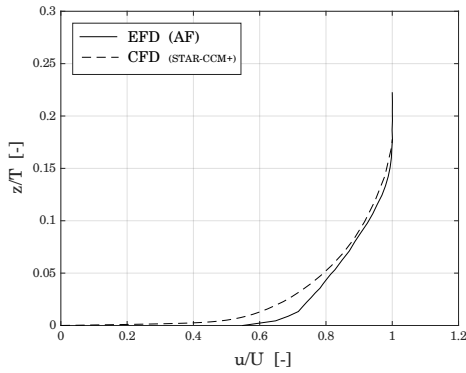Figure 3.8: Geometry and boundary conditions used for the RANS simulations.

Figure 3.9: The numerical and the experimental boundary layers at $x/c = 0.347$ upstream of the wing leading-edge.

(a) Stream-wise velocity fields from the BS (left) and AF (right) configurations.

(b) Stream-wise velocity fields from the LF (left) and SF (right) configurations.
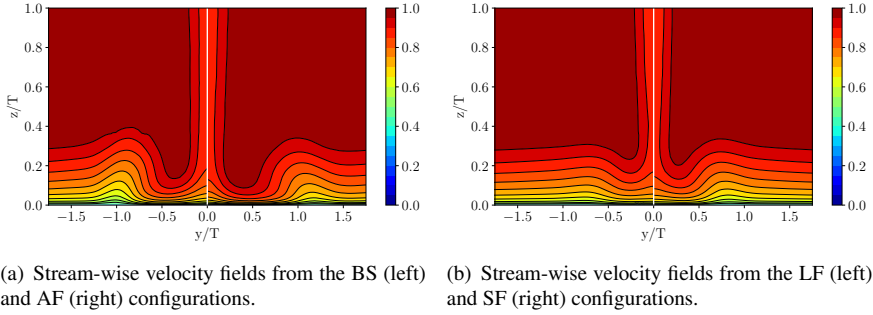
Figure 3.10: Mean stream-wise velocity fields in the wake of the BS, AF, SF, and LF configurations at $x/T = 5.33$ downstream of the trailing edge as obtained from the second round of CFD simulations.

region of the flat plate, wing, and wind-tunnel walls with $y^+ < 1$, and with unstructured mesh cells everywhere else in the domain. After a grid convergence study, a mesh with approximately 11.5 million cells is selected to simulate the baseline, anti-fairing, and leading-edge-fairing performances at ambient air conditions and $U_\infty = 20$ m/s. Steady, incompressible, fully-turbulent RANS simulations are carried out with a Spalart-Allmaras turbulence model. The inlet boundary layer shape is imposed so that a boundary layer thickness as close as possible to that of the anti-fairing experiment is obtained at $x/T = 2.313$ upstream of the wing leading-edge as shown in Fig. 3.9.

Figure 3.10 shows the velocity flow fields normalized by the free-stream speed in the wake of the wing. By comparing these images with those of Fig. 3.7, it is readily observed that the velocity deficit reduction caused by the AF is still present, although more subtly. The displacement of the vortex core further away from the symmetry line at $y/T = 0$ caused by the AF can also be observed in the numerical results of Fig. 3.10(a). This is a good indication of the ability of the CFD to capture significant qualitative effects of the AF on the velocity field.

Another indication of the good agreement between simulations and experiments is obtained by comparing the wake of the SF/LF configuration in Fig. 3.7(b) and Fig. 3.10(b). In both cases, the action of the leading-edge fairing weakens the effect of the horseshoe vortex. Although the action of the horseshoe vortex has been damped, from a visual inspection, it is not clear whether the leading-edge fairings decrease the overall velocity deficit, given the presence of a lower stream-wise velocity in the region $0 \leq |y/T| \leq 0.5$.

In order to understand how the anti-fairing modifies the flow in the junction region, its effects on the pressure and skin-friction coefficient distributions on the wall can be compared with those of the other geometries examined. Figure 3.11 shows the contours of the pressure coefficient c_p on the wall near the junction region. In the baseline case, the incoming boundary layer experiences a weak adverse pressure gradient far from the wing, which gradually increases as the flow approaches the leading-edge, as shown on the

(a) Baseline (bottom) and anti-fairing (top).

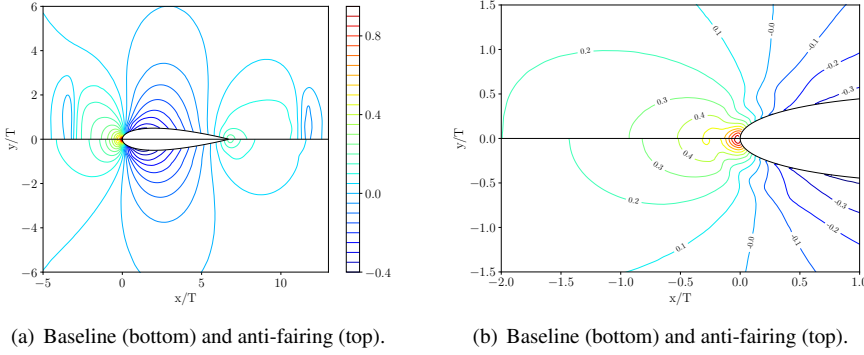(b) Baseline (bottom) and anti-fairing (top).

Figure 3.11: Pressure coefficient contours on the wall in the junction area (left) and near the wing leading-edge (right).

bottom side of Fig. 3.11(a). On the other hand, a low-pressure area forms at the beginning of the anti-fairing at approximately $x/T = -3.5$. This area first creates a favorable pressure gradient, which accelerates the flow, and then a local region of stronger adverse pressure gradient than in the baseline case, between $x/T = -2$ and $x/T = 0$, as observed in Fig. 3.11(b). The anti-fairing also causes a higher negative pressure coefficient at the thickest part of the wing, which causes the flow to have a smaller acceleration over the wing than in the baseline case. After the point of maximum thickness on the wing, the recovery of the pressure starts and continues downstream of the wing trailing edge. Because of viscous losses, the pressure does not entirely recover, and this high-pressure region has a smaller magnitude than that upstream of the leading edge of the wing. In the AF case, a favorable pressure gradient is present at $x/T = 11.5$, which impresses a final acceleration to the flow. Note that the kinked contour lines along the wing nose seen in Fig. 3.11(b) are artifacts produced by the RANS simulations, as noted by Ryu et al. [35].

The effect of the large fairing on the pressure coefficient on the wall can be observed in Fig. 3.12 (the effects of the small fairing are similar). Figure 3.12(a) shows that the pressure contours over and behind the wing do not differ significantly between the LF and BS configuration and that the main differences are observable at the wing's leading-edge. Indeed, as shown in Fig. 3.12(b), the presence of the leading-edge fairing dramatically reduces the adverse pressure gradient experienced by the flow in the baseline configuration, thus postponing the onset of the horseshoe vortex.

Figure 3.13 displays the evolution of the skin-friction coefficient c_f in the junction region. In the baseline case, c_f decreases as the wing is approached due to the adverse pressure gradient encountered, and becomes zero in correspondence of the location where the boundary layer flow lifts from the wall and forms the horseshoe vortex. A region of large skin friction is then present around the wing, thus implying high shear stresses caused by the action of the HSV. During its downward movement, the horseshoe vortex brings high-momentum fluid from the free-stream into the boundary layer close to the
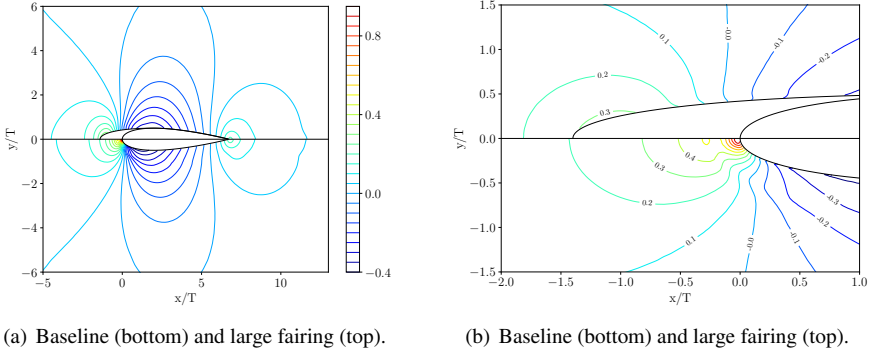
(a) Baseline (bottom) and large fairing (top).

(b) Baseline (bottom) and large fairing (top).

Figure 3.12: Pressure coefficient contours on the wall in the junction area (left) and near the wing leading-edge (right).

(a) Baseline (bottom) and anti-fairing (top).
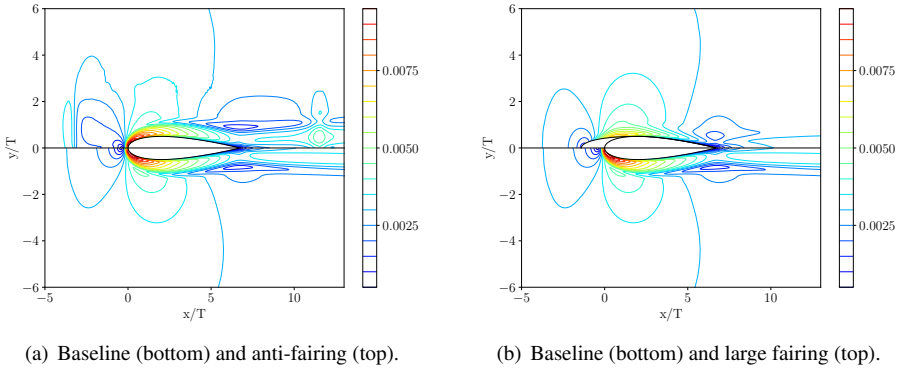
(b) Baseline (bottom) and large fairing (top).

Figure 3.13: Skin-friction coefficient contours on the wall in the junction area.

wing and, conversely, takes low-momentum fluid from the boundary layer into the free-stream as a result of its upward movement. It is this action that causes the blob of low skin friction immediately behind the wing, as shown in Fig. 3.13(a). The same figure also illustrates the differences in c_f distribution between the BS and AF geometry. In the anti-fairing case, regions of higher shear-stress are present at $x/T = -3.5$ and $x/T = 11.5$, in correspondence to the beginning and end of the cavity. This is the result of the combined action of the adverse pressure gradients generated by the concavity and the wing. Note that the limited depth of the anti-fairing ensures that no separation of the flow is present at its origin or termination. Figure 3.13(b) compares the evolution of c_f for the BS and LF configurations. The maximum skin friction is smaller in the LF case than in the BS. However, a region of high skin friction caused by the interaction of the wing and wall boundary layer is still noticeable in the junction region.

(a) Surface streamlines of the BS (top) and AF (bottom) configurations.

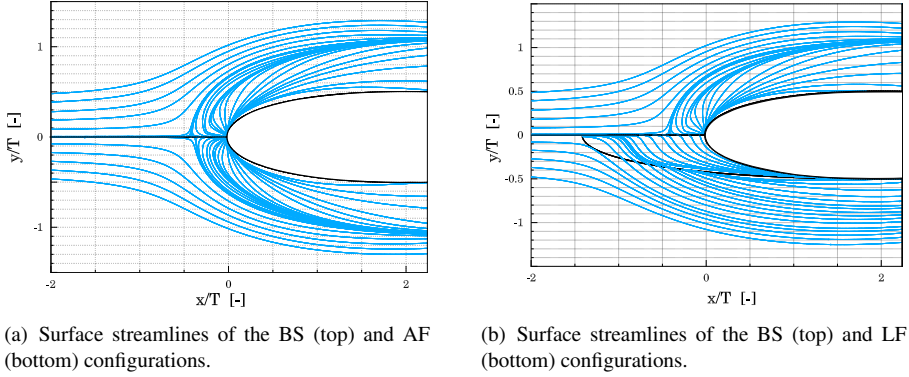(b) Surface streamlines of the BS (top) and LF (bottom) configurations.

Figure 3.14: Surface streamlines on the body for the BS, AF and LF configurations.

One final indication of the effect of the anti-fairing on the flow can be gathered by looking at the surface streamlines on the body of each configuration, as displayed in Fig. 3.14. Examining Fig. 3.14(a), it can be noted how the horseshoe vortex footprint is still present in the AF case, but the location of the separation point is closer to the wing than in the BS case. This phenomenon can be again explained by referring to Fleming et al.'s work [34], in which larger MDFs caused the vortex core and vorticity to move closer to the wing leading-edge. Connecting this observation to the one made in Section 3.3 confirms that the main effect of the anti-fairing on the wall boundary layer ahead of the wing leading-edge is that of increasing the momentum thickness θ. This is due to the slowdown of the boundary layer flow at the beginning of the AF caused by the adverse pressure gradient generated by its concave shape. Indeed, the anti-fairing momentum thickness at $x/T = -1.5$ is 2.337×10^{-2}, while that for the baseline case is 2.179×10^{-2}.

This effect, in turn, could reduce the shear in the boundary layer responsible for the viscous component of drag and form the low skin-friction region ahead of the wing of Fig. 3.13(a). Figure 3.14(b) shows the comparison between the streamlines patterns on the large fairing and the baseline geometry. We notice that the absence of a separation line indicates the complete disappearance of the horseshoe vortex at the leading-edge.

3.5   Drag Analysis

In the following, we derive an approach for the estimation of the *change* in drag force between the AF/SF/LF and the baseline configuration. The estimation of drag from experiments and numerical simulations is subject to a variety of errors and uncertainties [36], hence only drag deltas are presented in this section.

In many applications of technical interest it is sufficient to study the Reynolds-averaged flow quantities. In such cases, the conservation of momentum for a

steady flow in an arbitrary volume Ω and with no source terms can be written as:

$$\int_{\Omega} \nabla \cdot (\rho \boldsymbol{v} \otimes \boldsymbol{v} + p\boldsymbol{I} - \boldsymbol{\tau})d\Omega = 0, \tag{3.2}$$

where $\boldsymbol{v} = v_1\boldsymbol{i} + v_2\boldsymbol{j} + v_3\boldsymbol{k}$ is the velocity vector, $\boldsymbol{i}$, $\boldsymbol{j}$, $\boldsymbol{k}$ are unit vectors of a Cartesian coordinate system, with $\boldsymbol{i}$ aligned with the streamwise direction of the flow; $\boldsymbol{I}$ is the unit tensor, and $\boldsymbol{\tau}$ is the viscous stress tensor for an incompressible flow ($\nabla \cdot \boldsymbol{v} = 0$), with components

$$\tau_{ij} = \mu\left(\frac{\partial v_j}{\partial x_i} + \frac{\partial v_i}{\partial x_j}\right) - \rho v_i' v_j' \approx \mu_{\text{tot}}\left(\frac{\partial v_j}{\partial x_i} + \frac{\partial v_i}{\partial x_j}\right), \tag{3.3}$$

where $v_i' v_j'$ is the Reynolds-stress tensor, and $\mu_{\text{tot}} = \mu + \mu_{\text{turb}}$ is the total viscosity, with μ_{turb} computed with an eddy viscosity turbulence model. Note that the overbar notation typical of Reynolds-averaged quantities has been suppressed for simplicity. After applying Gauss's theorem, (3.2) can be re-written as

$$\int_{S} (\rho \boldsymbol{v}(\boldsymbol{v} \cdot \boldsymbol{n}) + p\boldsymbol{I} \cdot \boldsymbol{n} - \boldsymbol{\tau} \cdot \boldsymbol{n})dS = 0, \tag{3.4}$$

where S is the entire surface boundary of the control volume Ω, and $\boldsymbol{n} = n_1\boldsymbol{i} + n_2\boldsymbol{j} + n_3\boldsymbol{k}$ is an outward-pointing unit normal to S. The domain Ω consists of the rectangular box represented in Fig. 3.15. The box has the same length and width as the rectangular area where the drag of the simulations was monitored, and has a height corresponding to half of that of the computational domain. In this situation, the boundary S of (3.4) can be expressed as $S = S_A \cup S_B \cup S_C \cup S_{D_1} \cup S_{D_2} \cup S_{D_3} \cup S_E \cup S_F$, where S_{D_2} and S_E represent the half-wing and flat-plate boundaries, respectively. Hence, it follows that

$$\int_{S_W} (\rho \boldsymbol{v}(\boldsymbol{v} \cdot \boldsymbol{n}) + p\boldsymbol{I} \cdot \boldsymbol{n} - \boldsymbol{\tau} \cdot \boldsymbol{n})dS = -\int_{S'} (\rho \boldsymbol{v}(\boldsymbol{v} \cdot \boldsymbol{n}) + p\boldsymbol{I} \cdot \boldsymbol{n} - \boldsymbol{\tau} \cdot \boldsymbol{n})dS, \tag{3.5}$$

where $S_W = \{S_{D_2}, S_E\} = \{S_{\text{wing}}, S_{\text{wall}}\}$, and $S' = S \setminus S_W$. The total aerodynamic force $\boldsymbol{F}$ on an object in a steady flow can be computed using either one of the two sides of (3.5) [37]. This result must be multiplied by two because of the symmetry boundary condition at $y/T = 0$. If the integral over the solid boundary is considered, the expression simplifies to:

$$\boldsymbol{F} = \int_{S_W} (p\boldsymbol{I} \cdot \boldsymbol{n} - \boldsymbol{\tau} \cdot \boldsymbol{n})dS, \tag{3.6}$$

and the drag is obtained by projecting $\boldsymbol{F}$ in the freestream direction, which, in our case, is parallel to $\boldsymbol{i}$:

$$D = \int_{S_W} (pn_1 - \tau_{11}n_1 - \tau_{12}n_2 - \tau_{13}n_3)dS. \tag{3.7}$$
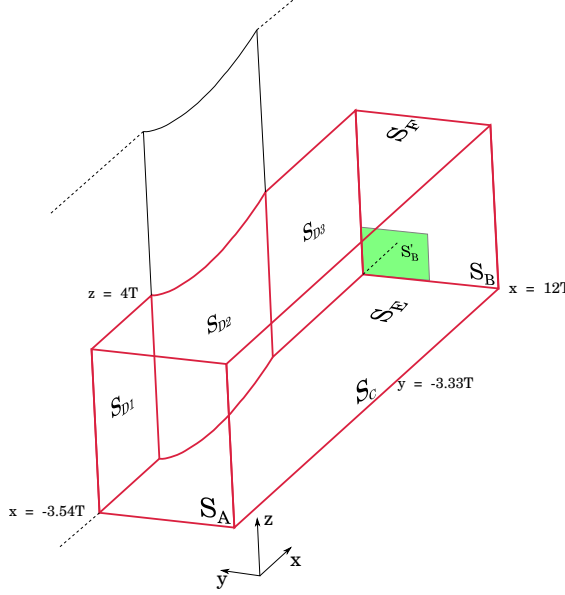
Figure 3.15: Control volume where the drag is evaluated.

Following a similar procedure for the right-hand side of (3.5), the aerodynamic drag can be expressed as:

$$D = - \int_{S'} (\rho v_1 (\boldsymbol{v} \cdot \boldsymbol{n}) + p n_1 - \tau_{11} n_1 - \tau_{12} n_2 - \tau_{13} n_3) dS. \tag{3.8}$$

To correct for any mass conservation error in the flow field, (3.8) can be evaluated as follows [38, 39]:

$$D = - \int_{S'} [\rho(v_1 - U_\infty)(\boldsymbol{v} \cdot \boldsymbol{n}) + (p - P_\infty) n_1 - \tau_{11} n_1 - \tau_{12} n_2 - \tau_{13} n_3] dS. \tag{3.9}$$

Since a symmetry boundary condition is imposed on S_{D_1} and S_{D_3}, their contribution to (3.9) vanishes[1]. Furthermore, when S_C and S_F are located in the freestream, sufficiently far away from the wing and wall respectively, (3.9) can be approximated as:

$$\hat{D} = - \int_{S_A \cup S_B} [\rho(v_1 - U_\infty) v_1 n_1 + (p - P_\infty) n_1 - \tau_{11} n_1] dS. \tag{3.10}$$

The RANS simulations of Section 3.4 were performed with the same inflow conditions for all the geometries. Hence, if S_A is taken sufficiently far upstream from the wing and the

---

[1]This is true only if we mirror the control volume across the symmetry plane when evaluating (3.9).

Table 3.1: Experimental and numerical drag difference computed using equation (3.11). Values in drag counts.

	Experiments	CFD
$\Delta c_{\hat{D}_{LF}}$	+0.084	-0.203
$\Delta c_{\hat{D}_{SF}}$	-0.009	-0.124
$\Delta c_{\hat{D}_{AF}}$	-7.748	-5.956

area were the anti-fairing is acting, the drag difference between the baseline and the other configurations can be estimated by simply taking the difference between the components of (3.10) integrated over the downstream plane S_B only.

3.5.1 Drag Estimation

Using the velocity fields from the experimental results, the drag difference between the anti-fairing and its corresponding baseline geometry can be estimated with

$$\Delta c_{\hat{D}} = \frac{- \int_{S_{B'_{BS}}} \rho(v_1 - U_\infty)v_1 n_1 dS + \int_{S_{B'_{AF}}} \rho(v_1 - U_\infty)v_1 n_1 dS}{\frac{1}{2}\rho_{\text{ref}} U_{\text{ref}}^2 A_{\text{ref}}}, \tag{3.11}$$

where $S_{B'_{[\cdot]}}$ indicates integration over a plane corresponding to the sPIV field of view, $\rho_{\text{ref}} = 1.2\text{kg/m}^3$, $U_{\text{ref}} = 20\text{m/s}$. For simplicity a reference area $A_{\text{ref}} = 1\text{m}^2$ was used, which is of the same order of magnitude of the sum of the wing and anti-fairing area used in this study ($A_{\text{wing}} + A_{AF} = 1.232\text{m}^2$). In equation (3.11), the pressure and viscous terms have been neglected since they have usually lower order of magnitude. The validity of this hypothesis can be tested by comparing the drag differences with those calculated using equation (3.7) or (3.9). The same holds for the drag difference between the small/large fairings and their corresponding baseline configuration. Furthermore, assuming that the drag deltas are not significantly influenced by the boundary-layer thickness makes it possible to compare them among the different experimental configurations and with the corresponding numerical results. The area of $S_{B'}$ where the integral is evaluated has the same dimensions of the sPIV field of view used to plot the results of Fig. 3.7.

Table 3.1 reports the drag differences of the small/large and anti-fairing with respect to the baseline configuration expressed in drag counts. The order of magnitude of the drag deltas from the experiments and the simulation agree well, although their exact values are not identical due to the differences between the results obtained with the two techniques. Nonetheless, it is clear that the anti-fairing reduces the momentum losses in $S_{B'}$ more than the small and large fairings do, and that the numerical results are accurate enough to be used to estimate and compare the drag deltas of the different geometries.

Although the area of $S_{B'}$ for the drag estimation is large enough to capture the main effect of the various configurations on the wall boundary layer, it is reasonable to ask whether a larger integration plane would alter the results. This is why equation (3.11)

Table 3.2: CFD drag difference in drag counts computed using equation (3.11) over S_B, (3.9), and equation (3.7), respectively.

	S_B	far-field	near-field
$\Delta c_{\hat{D}_{LF}}$	-1.121	-0.654	-0.704
$\Delta c_{\hat{D}_{SF}}$	-1.107	-0.462	-0.557
$\Delta c_{\hat{D}_{AF}}$	-7.209	-2.021	-2.634

was evaluated over the S_B plane shown in Fig. 3.15 using the CFD results. The first column of Table 3.2 reports the results of this analysis, and, by comparing them with the values in Table 3.1, we observe that the performance of SF and LF increase compared to both the experimental and numerical values evaluated on a smaller $S_{B'}$ plane. Also, the performance of the AF increases compared to the $\Delta c_{\hat{D}}$ from CFD and gets closer to the one estimated from experiments.

This analysis confirms that the field of view used in the sPIV experiment is big enough to capture the main flow features responsible for a reduction of the stream-wise momentum deficit. However, since S_B is located in the proximity of the wing, one cannot neglect the contribution of the pressure and viscous terms. Furthermore, also the side, top and upstream planes, are in the vicinity of the junction and their contribution to the far-field formulation of drag might be relevant. This is why the drag is also computed using equation (3.7) and equation (3.9). These expressions are also known as near-field and far-field drag, and provide the most accurate drag estimation possible with the available CFD data.

The second and third columns of Table 3.2 returns very similar drag deltas for the two techniques used. Once again, all configurations reduce the drag with respect to the baseline, with the anti-fairing reducing drag the most. There are, however, significant differences between the results obtained when considering only the contribution of the downstream plane and the results obtained using the near-field or far-field methods. This suggests that the data on a plane downstream of the junction can be used only to roughly compare drag performances among different geometries and that the pressure and viscous contributions cannot be neglected. According to the drag analysis, the anti-fairing is between 4 and 5 times more effective at reducing junction drag than the small fairing, and between 3 and 4 times more effective than the large fairing.

3.5.2 The Working Mechanism of the Anti-Fairing

Since the optimization does not modify the wing shape, it is reasonable to assume that the mechanism responsible for the drag reduction is due to the changes to the flat plate shape. Hence, the analysis of the components of the near-field drag of the body could reveal important features about the drag-reducing mechanism of the anti-fairing.

In order to do so, we subdivide S_{wall} into thirtyfive, equally spaced sub-domains, as shown in Fig. 3.16, and calculate the viscous and pressure contribution of each sub-domain using equation (3.7). We note that the anti-fairing has a marginal effect on the
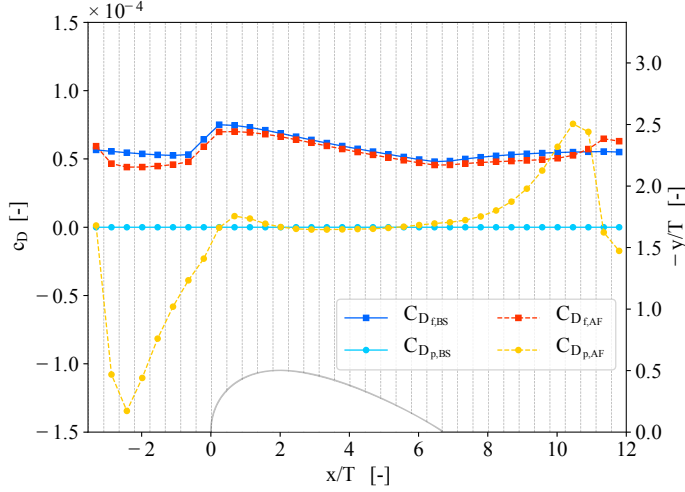
Figure 3.16: Comparison of viscous (c_{D_f}) and pressure (c_{D_p}) components of the near-field drag for the anti-fairing and baseline geometry. The vertical grid lines identify the sub-domains over which each contribution was calculated.

viscous drag, while it radically changes the pressure component.

Upstream of the wing, the viscous drag coefficient of the anti-fairing is smaller than that of the baseline geometry, as already observed in Fig. 3.13(a). This is due to the combined action of the adverse pressure gradient generated by the wing and the front of the concavity. Around the wing, the value of the viscous drag coefficient is approximately the same for both configurations. This is also true downstream of the wing trailing edge up to $x/T = 11$, where a slightly higher viscous component is registered for the anti-fairing as a consequence of the acceleration of the flow caused by the favorable pressure gradient at those locations.

The component of the drag coefficient due to pressure is zero for the baseline configuration, while it displays abrupt changes at the very beginning and at the very end of the anti-fairing, where its curvature is highest. Upstream of the wing, a negative pressure drag component is generated by the anti-fairing, which is only partially counterbalanced by the positive component at the end of the concavity. The anti-fairing therefore produces net negative pressure drag because the recovery of pressure over the wing is incomplete as a result of the action of viscous forces. Hence, the positive pressure drag component downstream of the wing's trailing edge (increasing the drag) is smaller in magnitude than the negative one upstream of the wing leading edge (decreasing the drag). This can also be observed in Fig. 3.17, where the evolution of the pressure coefficient on the symmetry plane at $z/T = 0$, and the anti-fairing cross-section at $y/T = -0.9$ from the

symmetry plane are plotted. The dashed vertical lines delimit the regions where the curvature of the anti-fairing is largest and hence also its contribution to the pressure drag. The yellow-filled regions indicate the high-pressure regions upstream and downstream the wing, while the magenta-filled one indicates a region of low pressure. It is readily observed as the high-pressure area upstream of the wing leading edge is much larger than that downstream of the wing trailing edge. Furthermore, the stream-wise components of the AF's surface normal vector point in opposite directions at the beginning and termination of the concavity. Hence, the combinations of these two effects results in a propulsive force. The interaction of the wing with the concave geometry of the anti-fairing is the key phenomenon that lies at the heart of the drag reduction and should also be observable for laminar flow.

Based on this understanding of the effect, we can speculate on the performance of the anti-fairing at higher Reynolds and Mach numbers. We expect the propulsive effect to be present throughout the subsonic regime. Pressure recovery on an airfoil can never be complete due to the presence of viscous losses as the flow proceeds along the wing. Hence, the pressure difference between the leading-edge region and the trailing-edge region will always create a propulsive effect when an anti-fairing is placed around the junction area. However, higher Reynolds numbers cause the turbulent boundary layer developing on the wing to have a fuller profile, which aids the pressure recovery over the wing [40]. Therefore, even though the anti-fairing will work at higher Reynolds numbers, its effectiveness may decrease. This problem could be mitigated by moving the aft curvature of the anti-fairing far downstream from the trailing edge of the wing, into a region of lower pressure, or even completely removing it, such that the presence of the aft curvature activates no additional pressure force acting in the same direction of the drag force. Whether these benefits are present in reality and also in the transonic and supersonic regimes, is something to investigate in subsequent studies.

3.6 Conclusions

In this Chapter, we carried out a gradient-based optimization of a wing-body junction to analyze the effect of changes to the geometry of the body on the drag. The wing shape was kept fixed, and the body was constrained to deform in the span-wise direction. The optimized geometry presented itself as a shallow dent wrapped around the wing, with a thickness comparable to that of the approaching boundary layer. In order to validate the optimization results, an experiment and new CFD simulations with a finer mesh were performed, and the results compared with two types of leading-edge fairings.

By looking at the stream-wise velocity component in the wake of the configurations studied, both experimental and numerical results indicate that the optimized geometry, named *anti-fairing*, reduces the momentum deficit in the boundary-layer region and pushes the tongues of low momentum further away from the vertical symmetry plane. Thanks to the availability of numerical data everywhere in the domain, we noticed that the stagnation point on the wall ahead of the wing leading-edge moved closer to the wing. These latter two characteristics can be linked to the considerations on the momentum
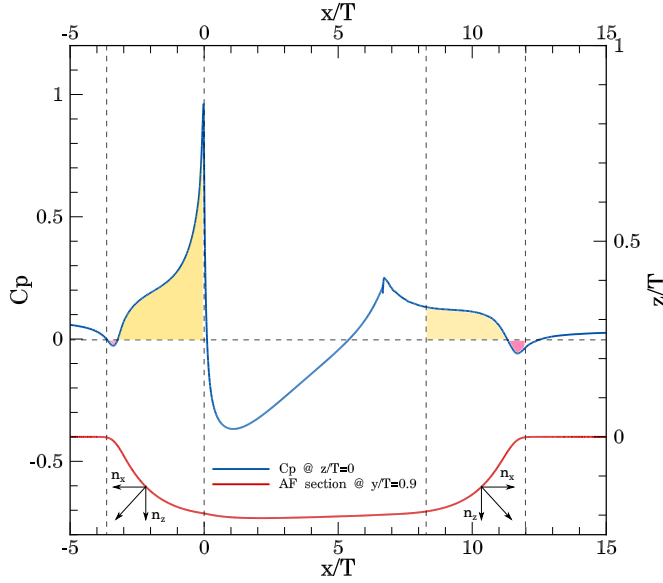
Figure 3.17: Pressure coefficient on the symmetry plane at $z/T = 0$ (blue); AF cross-section at $y/T = 0.9$. The dashed vertical lines delimit the regions of high curvature.

deficit factor to conclude that the momentum thickness θ at the wing leading-edge is increased as an effect of the presence of the anti-fairing.

By exploiting the integral form of the momentum equations, the drag difference between the various configurations and the baseline geometry could be estimated. A clear trend confirmed that the anti-fairing is not only capable of reducing the drag with respect to the baseline geometries, but also outperformed conventional leading-edge fairings. Contrary to traditional methods, the anti-fairing does not seek to suppress the formation of the horseshoe vortex, but instead tries to offer a pocket where it can accommodate. We propose that the combined effects of a decrease in viscous and pressure drag on the body lie at the heart of the reduction in junction drag. In particular, the magnitude of the negative pressure drag component generated at the beginning of the anti-fairing is larger than the positive pressure drag component at the rear of it. This is due to the high-pressure region generated by the combined action of the wing and anti-fairing shape ahead of the wing leading-edge, and by the incomplete pressure recovery at the wing trailing edge.

3.7 Appendix A: Details of the Experimental Setup

Figure 3.18 shows the side-view of the experimental setup described in Section 3.3. In particular, Fig. 3.18(a) shows the configuration for the leading-edge fairings and their corresponding baseline geometry. This is composed by a flat plate (block 1), the wing,
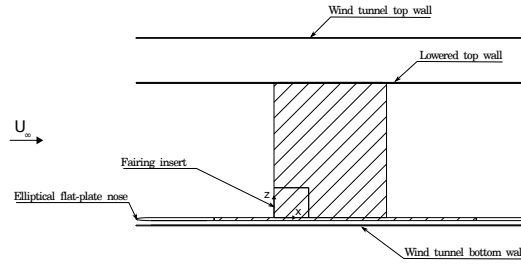
(a) The experimental set-up for the LF and SF configuration.
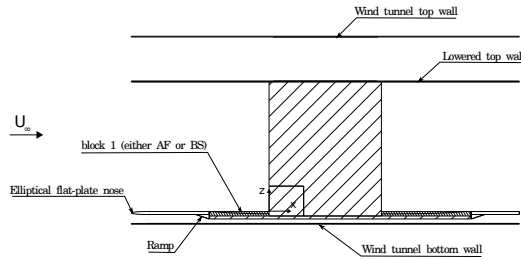
(b) The experimental set-up for the BS and AF configuration.

Figure 3.18: The two slightly different set-ups used during the experiments.

and the elements forming block 2. Since we use the anti-fairing as a retrofit to these simple configurations, some changes had to be made. In particular, we needed to place the anti-fairing block 1 on top of the flat-plate used to test the leading-edge fairings, and block 2 had to be elevated to achieve a smooth connection between the two blocks as shown in Fig. 3.18(b). Similarly, for the flat surface used as block 1 to form the baseline geometry to compare with the anti-fairing.

This modification changes the height of the body surface from the wind-tunnel bottom wall and is probably affecting the flow at the flat plate leading edge, thus causing incoming boundary layers of different thicknesses.

References

[1] Simpson, R., "Junction flows," *Annual Review of Fluid Mechanics*, Vol. 33, No. 1, 2001, pp. 415–443.

[2] Gand, F., Deck, S., Brunet, V., and Sagaut, P., "Flow dynamics past a simplified wing body junction," *Physics of Fluids*, Vol. 22, No. 11, 2010, pp. 115111.

[3] Hoerner, S., "Fluid Dynamic Drag. 1965," *Bricktown, NJ: Published by the author*, 1992.

[4] Gand, F., Brunet, V., and Deck, S., "Experimental and numerical investigation of a wing-body junction flow," *AIAA journal*, Vol. 50, No. 12, 2012, pp. 2711–2719.

[5] Gand, F., Monnier, J.-C., Deluc, J.-M., and Choffat, A., "Experimental study of the corner flow separation on a simplified junction," *AIAA Journal*, Vol. 53, No. 10, 2015, pp. 2869–2877.

[6] Barber, T., "An investigation of strut-wall intersection losses," *Journal of Aircraft*, Vol. 15, No. 10, 1978, pp. 676–681.

[7] Philips, D., Cimbala, J., and Treaster, A., "Suppression of the wing-body junction vortex by body surface suction," *Journal of aircraft*, Vol. 29, No. 1, 1992, pp. 118–122.

[8] Seal, C. and Smith, C., "The control of turbulent end-wall boundary layers using surface suction," *Experiments in Fluids*, Vol. 27, No. 6, 1999, pp. 484–496.

[9] Johnson, M., Ravindra, K., and Andres, R., "Comparative study of the elimination of the wing fuselage junction vortex by boundary layer suction and blowing," *32nd AIAA Aerospace Sciences Meeting and Exhibit, Reno NV, January*, 1994, pp. 10–13.

[10] McGinley, C., "Note on vortex control in simulated sail-hull interaction," *Journal of ship research*, Vol. 31, No. 2, 1987, pp. 136–138.

[11] Devenport, W., Agarwal, N., Dewitz, M., Simpson, R., and Poddar, K., "Effects of a fillet on the flow past a wing-body junction," *AIAA journal*, Vol. 28, No. 12, 1990, pp. 2017–2024.

[12] Bernstein, L. and Hamid, S., "On the effect of a strake-like junction fillet on the lift and drag of a wing," *The Aeronautical Journal (1968)*, Vol. 100, No. 992, 1996, pp. 39–52.

[13] Van Oudheusden, B., Steenaert, C., and Boermans, L., "Attachment-line approach for design of a wing-body leading-edge fairing," *Journal of aircraft*, Vol. 41, No. 2, 2004, pp. 238–246.

[14] Kubendran, L., Bar-Sever, A., and Harvey, W., "Flow control in a wing/fuselage-type juncture," *26th Aerospace Sciences Meeting*, 1988, p. 614.

[15] Green, B. and Whitesides, J., "Method for designing leading-edge fillets to eliminate flow separation," *Journal of Aircraft*, Vol. 40, No. 2, 2003, pp. 282–289.

[16] Hinson, B. and Hoffmann, K., "Parametric Exploration of Wing–Body Junction Flow Using Computational Fluid Dynamics," *Journal of Aircraft*, Vol. 52, No. 5, 2015, pp. 1492–1509.

[17] LaFleur, R. and Langston, L., "Drag reduction of a cylinder/endwall junction using the iceformation method," *Journal of fluids engineering*, Vol. 115, No. 1, 1993, pp. 26–32.

[18] Kairouz, K. and Rahai, H., "Turbulent junction flow with an upstream ribbed surface," *International journal of heat and fluid flow*, Vol. 26, No. 5, 2005, pp. 771–779.

[19] Vassberg, J., Sclafani, A., and DeHaan, M., "A wing-body fairing design for the DLR-F6 model: a DPW-III case study," *23rd AIAA Applied Aerodynamics Conference*, 2005, pp. 4730.

[20] Li, C., Ye, Z., and Wang, G., "Simulation of flow separation at the wing-body junction with different fairings," *Journal of aircraft*, Vol. 45, No. 1, 2008, pp. 258–266.

[21] Peigin, S. and Epstein, B., "Aerodynamic optimization of essentially three-dimensional shapes for wing-body fairing," *AIAA journal*, Vol. 46, No. 7, 2008, pp. 1814–1825.

[22] Song, W. and Lv, P., "Two-level wing-body-fairing optimization of a civil transport aircraft," *Journal of Aircraft*, Vol. 48, No. 6, 2011, pp. 2114–2121.

[23] Brezillon, J. and Dwight, R., "Applications of a discrete viscous adjoint method for aerodynamic shape optimisation of 3D configurations," *CEAS Aeronautical Journal*, Vol. 3, No. 1, 2012, pp. 25–34.

[24] Xu, S., Timme, S., Mykhaskiv, O., and Müller, J., "Wing-body junction optimisation with CAD-based parametrisation including a moving intersection," *Aerospace Science and Technology*, Vol. 68, 2017, pp. 543–551.

[25] Belligoli, Z., *Optimization of a Wing-Body Junction*, Master's thesis, TU Delft, 2015.

[26] White, F. and Corfield, I., *Viscous fluid flow*, Vol. 3, McGraw-Hill New York, 2006.

[27] Roe, P. L., "Approximate Riemann solvers, parameter vectors, and difference schemes," *Journal of computational physics*, Vol. 43, No. 2, 1981, pp. 357–372.

[28] Spalart, P. and Allmaras, S., "A one-equation turbulence model for aerodynamic flows," *30th aerospace sciences meeting and exhibit*, 1992, p. 439.

[29] Apsley, D. and Leschziner, M., "Investigation of advanced turbulence models for the flow in a generic wing-body junction," *Flow, Turbulence and Combustion*, Vol. 67, No. 1, 2001, pp. 25–55.

[30] Fu, S., Xiao, Z., Chen, H., Zhang, Y., and Huang, J., "Simulation of wing-body junction flows with hybrid RANS/LES methods," *International Journal of Heat and Fluid Flow*, Vol. 28, No. 6, 2007, pp. 1379–1390.

[31] Paciorri, R., Bonfiglioli, A., Di Mascio, A., and Favini, B., "RANS simulations of a junction flow," *International Journal of Computational Fluid Dynamics*, Vol. 19, No. 2, 2005, pp. 179–189.

[32] Sederberg, T. W. and Parry, S., "Free-form deformation of solid geometric models," *ACM SIGGRAPH computer graphics*, Vol. 20, No. 4, 1986, pp. 151–160.

[33] Palacios, F., Alonso, J., Duraisamy, K., Colonno, M., Hicken, J., Aranake, A., Campos, A., Copeland, S., Economon, T., Lonkar, A., et al., "Stanford University Unstructured (SU 2): an open-source integrated computational environment for multi-physics simulation and design," *51st AIAA Aerospace Sciences Meeting including the New Horizons Forum and Aerospace Exposition*, 2013, p. 287.

[34] Fleming, J., Simpson, R., Cowling, J., and Devenport, W., "An experimental study of a turbulent wing-body junction and wake flow," *Experiments in fluids*, Vol. 14, No. 5, 1993, pp. 366–378.

[35] Ryu, S., Emory, M., Iaccarino, G., Campos, A., and Duraisamy, K., "Large-Eddy Simulation of a Wing–Body Junction Flow," *AIAA Journal*, Vol. 54, No. 3, 2016, pp. 793–804.

[36] Van Dam, C., "Recent experience with different methods of drag prediction," *Progress in Aerospace Sciences*, Vol. 35, No. 8, 1999, pp. 751–798.

[37] Giles, M. and Cummings, R., "Wake integration for three-dimensional flowfield computations: theoretical development," *Journal of aircraft*, Vol. 36, No. 2, 1999, pp. 357–365.

[38] van Oudheusden, B., Scarano, F., Roosenboom, E., Casimiri, E., and Souverein, L., "Evaluation of integral forces and pressure fields from planar velocimetry data for incompressible and compressible flows," *Experiments in Fluids*, Vol. 43, No. 2-3, 2007, pp. 153–162.

[39] Chao, D. and Van Dam, C., "Wing drag prediction and decomposition," *Journal of Aircraft*, Vol. 43, No. 1, 2006, pp. 82–90.

[40] Kundu, P. K., Cohen, I. M., and Dowling, D. R., "Chapter 9 - Boundary Layers and Related Topics," *Fluid Mechanics (Fifth Edition)*, Academic Press, fifth edition ed., 2012, pp. 361 – 419.

4

Data Assimilation Techniques for Turbulent Flows

Abstract *In Chapter 3, I used a gradient-based optimization technique in combination with a RANS solver to obtain a novel, drag-reducing design for a wing/flat plate junction. To remain computationally tractable, RANS solvers use a turbulence model that is often responsible for uncertainties and errors in the simulation of complex flows. This Chapter addresses the problem of reducing errors caused by a turbulence model using data assimilation (DA), a technique that integrates experimental and numerical results to increase the accuracy of the simulations. First, different types of turbulence modeling errors are discussed together with a short review of DA applications for their correction. Second, two new data assimilation techniques are formally derived from a Bayesian perspective, and their theoretical ability to overcome some issues of previous DA techniques are analyzed. Finally, results obtained with these new techniques are compared with a state-of-the-art method taken as reference, and practical strengths and limitations are discussed.*

4.1   Introduction

Despite the continuous growth in computational power, the routine use of Direct Numerical Simulations (DNS) or Large Eddy Simulations (LES) in many industrial applications is unfeasible due to the extremely high requirements in terms of power, memory, and time. This is why Reynolds-averaged Navier-Stokes (RANS) computer codes are still the workhorse for turbulent simulations of industrial flows. However, RANS numerical results are affected by mesh quality, iterative convergence thresholds, level of detail of the geometry, and modeling of turbulence effects. While techniques exist for minimizing the first three types of error, there is no straightforward way to address errors due to the modeling of turbulence.

According to Duraisamy et al. [1], these can be categorized broadly as (a) *structural* errors, essentially arising from the choice of independent variables of the turbulence model; (b) *functional* errors, due to the choice of the functional form to describe the physical processes of the independent variables; (c) *parametric* errors, caused by the non-universality of the closure coefficients. These factors cause the result of the simulation of a specific flow condition to deviate from the truth.

Data-driven methods make use of the increasing availability of high-fidelity data (from LES, DNS, experiments) either to build predictive models that can correct turbulence-model errors [2–5], or to apply Bayesian inference [6] to compute the optimal values of variables associated with the turbulence model for a particular test case. This Chapter focuses on the latter topic and, in particular, on using variational data assimilation techniques to correct functional and structural errors for optimal flow reconstruction using few sparse high-fidelity data.

Parametric errors are the most tractable because they form a low-dimensional vector which can be re-calibrated by exploiting the full capabilities of a Bayesian inversion procedure. Several studies [7–11] dealt with parametric error correction and showed that re-calibration of the closure coefficients can improve RANS results. However, the effectiveness of correcting parametric errors is limited by their inability to influence more general types of error, such as functional and structural errors.

Dealing with functional and structural errors in turbulence models implies solving high dimensional inverse problems. The most common methods to approach these types of problems are variational or Kalman filtering techniques. Dow and Wang [12, 13] and Duraisamy and co-workers [14, 15] used variational data assimilation to compute a corrective scalar field of the eddy viscosity and of the turbulent production term, respectively. Duraisamy and co-workers showed that their variational technique could work with few high-fidelity data and for high Reynolds number cases. Their work was extended to three-dimensional flows by He et al. [16], while Singh et al. [18] introduced a similar technique for correcting structural errors by using the perturbations to the eigenvalues of the anisotropy tensor as control parameters. In parallel, Xiao and co-workers [20, 21] developed the same concept with the ensemble Kalman filter (EnKF). This technique has the advantage of providing confidence intervals on the elements of the vector of optimal control parameters, but requires mapping the control vector to a lower dimensional space due to the high dimensionality of the inverse problem. Finally, Schmid and co-workers [22] used variational techniques to compute an optimal forcing term corresponding to the divergence of the Reynolds stress tensor. However, this methodology worked only at low Reynolds numbers because of difficulties in computing a physical initial solution to the steady Navier-Stokes equations with zero forcing at high Reynolds numbers [23].

In this Chapter, variational data assimilation is used to correct the Reynolds stress tensor approximated by a turbulence model in two different ways. In the first case, the perturbations to the eigenvalues and eigenvectors of the Reynolds stress tensor are selected as control parameters. In the second case, the random matrix approach [24] is used to ensure the physical realizability of the Reynolds stress tensor by selecting the perturbations to the elements of the upper triangular matrix resulting from its Cholesky decomposition as control variables. These methodologies are compared with the one proposed by Duraisamy and co-workers [14, 15], which is taken as reference for its simplicity and efficacy. High Reynolds number flow problems with phenomena known to be hard to reproduce with standard turbulence models are chosen as validation cases.

This Chapter is structured as follows. In Section 4.2 the structure of a general data assimilation problem starting from Bayes' rule is introduced (Section 4.2.1), and then the derivation of each of the data assimilation variants used in this work is presented (Sections 4.2.2, 4.2.3, 4.2.4). Section 4.3 presents the results of the application of the DA methods to two test cases: one used for validation purposes (section 4.3.1), and the other for an in-depth analysis (section 4.3.2). Finally, Section 4.4 summarizes the main findings and discusses future improvements.

4.2 Proposed Methodology

As explained in Section 2.2, when working with compressible flows, a density-weighted (or Favre) averaging is used. After the averaging process, a term representing the effect of turbulence on the mean flow appears. This is the Reynolds-stress tensor $R_{ij} = \widetilde{v_i'' v_j''}$, whose value in terms of averaged quantities is unknown. RANS closure models construct an approximation of this term, and linear eddy viscosity models based on the Boussinesq

hypothesis are industry's favorite choice. These models assume that R_{ij} is linearly related to the mean rate of strain S_{ij} through a turbulent scalar viscosity ν_{turb}, i.e.:

$$R_{ij} \approx R_{ij}^{\text{ev}} = -2\nu_{\text{turb}}S_{ij} + \frac{2k}{3}\delta_{ij}, \tag{4.1}$$

where $k = R_{nn}^{\text{ev}}/2$ is the turbulent kinetic energy, $S_{ij} = (\partial_j\tilde{v}_i + \partial_i\tilde{v}_j)/2 - \partial_n\tilde{v}_n/3$ is the deviatoric, trace-free part of the strain rate tensor. Eddy-viscosity models introduce additional transport equations for quantities connected to ν_{turb} in order to close the system of equations. In this work, we use Menter's $k - \omega$ shear stress transport (SST) model [25], which uses transport equations for k and the specific dissipation rate ω.

We aim to develop and compare variational data assimilation techniques that correct the errors introduced by eddy viscosity models in order to reconstruct the turbulent flow field at a given flow condition. Variational data assimilation uses a gradient-based algorithm to tune a vector of N_m control parameters $\boldsymbol{\theta}$ in order to minimize an error function expressed as the difference (in a certain norm) between N_d high-fidelity measurements of a quantity and the same quantity as computed by a numerical simulation, where usually $N_d << N_m$.

As explained in Section 2.5, gradient-based methods are suited for this type of high-dimensional optimization thanks to the adjoint approach [26, 27], a mathematical technique that allows one to obtain the gradients of the objective function with respect to *any* number of control parameters at the cost of only one additional flow evaluation [28, 29]. Thanks to the work of Albring et al. [30, 31], the SU2 [32, 33] CFD software comes with a discrete adjoint framework based on algorithmic differentiation that makes it possible to obtain the gradients of many objective functions with minimal source code modifications.

This work makes use of the low-memory Broyden-Fletcher-Goldfarb-Shanno (L-BFGS) [34] optimization algorithm to update the value of $\boldsymbol{\theta}$ and compute the step size of the optimization. The initial values of the control parameters are dependent on the DA methodology, but the general idea is to specify them in such a way that the result of the first optimization iteration is that of a RANS with an uncorrected turbulence model. Finally, the optimization terminates when either

- $\max(|\partial_i\mathcal{J}|) \leq 5 \cdot 10^{-5}$ for $i = 1, ..., N_m$, or

- $\frac{\mathcal{J}^q - \mathcal{J}^{q+1}}{\max\{|\mathcal{J}^q|, |\mathcal{J}^{q+1}|, 1\}} \leq 10^{-3}$,

where q is the q-th optimization iteration, $\mathcal{J}$ is the objective function, $\partial_i\mathcal{J}$ is the gradient of the objective function with respect to the i-th control parameter, and the value of the thresholds are specified by the user.

The result of the DA is valuable both when forecasting the behavior of complex systems and for re-calibrating numerical models for future model development. In the next Section, we use a Bayesian perspective to formulate the data assimilation problem in a general, probabilistic setting.

4.2.1 Bayesian Formulation of the Problem

Quantities $d \in \mathbb{R}^{N_d}$ measured experimentally differ from the true values of those quantities $d_{\text{true}} \in \mathbb{R}^{N_d}$ due to measurement noise, and experimental bias. This discrepancy is modeled statistically as

$$d = d_{\text{true}} + \varepsilon, \quad \varepsilon \sim \mathcal{N}(\mathbf{0}, \sigma_{\text{exp}}^2 I), \tag{4.2}$$

where zero bias is assumed, and noise to be independent identically distributed (i.i.d.) normal random variables with known standard deviation σ_{exp} (obtained from the experimental procedure). Given some flow-state $U = [\rho, \rho v, \rho E, \rho k, \rho \omega]^\top \in \mathcal{U}$, let $\mathcal{B} : \mathcal{U} \to \mathbb{R}^{N_d}$ be a projection which extracts the measured quantities. Under most circumstances – including here – this operator will have negligible error, so that $d = \mathcal{B}(U_{\text{true}}) + \varepsilon$ is a reasonable generalization of equation (4.2) (where $U_{\text{true}} \in \mathcal{U}$ is the true state).

However, U_{true} is unknown and approximated by solving the RANS equations including boundary-conditions

$$\mathcal{R}(\hat{U}) = 0, \tag{4.3}$$

where $\hat{U} \neq U_{\text{true}}$, introducing non-negligible modelling error. Following the seminal work of Kennedy and O'Hagan [6] and previous work in fluid-dynamics [7, 9], we could write

$$d = \psi(x) \cdot \mathcal{B}(\hat{U}) + \varepsilon, \tag{4.4}$$

where $\psi \sim \mathcal{GP}(\mu_\psi, r_\psi)$ is a Gaussian-process needed to account for the errors in $\mathcal{R}(\cdot)$. A function of the spatial location x (e.g. see [8]), its mean $\mu_\psi(\cdot)$ and covariance functions $r_\psi(\cdot, \cdot)$, must be identified from the data (under some priors). This formulation allows predictions of the quantity d at unmeasured locations, but says nothing about other quantities. For example if d are measurements of pressure, ψ represents model-error in pressure, and does not speak to velocity.

Therefore in this work, we deviate from Kennedy and O'Hagan's formulation by moving the statistical term representing model error into the operator $\mathcal{R}$. This is logical: the source of error is within $\mathcal{R}$, and identification of this error will allow us to make predictions of unmeasured quantities. Let this discrepancy term be $\theta \in \Theta$, and modify the governing equations as

$$\mathcal{R}(\hat{U}, \theta) = 0. \tag{4.5}$$

By the implicit function theorem, equation (4.5) defines a function $\hat{U} : \Theta \to \mathcal{U}$, so that we can construct the statistical model

$$d = d_{\text{true}} + \varepsilon = \mathcal{B}(U(\theta)) + \varepsilon, \tag{4.6}$$

as an alternative to equation (4.4). To complete the model, it remains to define priors on θ.

The scope of the methods presented in this work is to find the maximum *a posteriori* (MAP) estimate of θ, minimizing the difference between experimental data and simulated

prediction, subject to reasonable priors on the model-error. This is an inverse problem and can be formulated in a general way using Bayes' theorem:

$$p(\boldsymbol{\theta}|\boldsymbol{d}) \propto p(\boldsymbol{d}|\boldsymbol{\theta})p_0(\boldsymbol{\theta}), \tag{4.7}$$

where $p_0(\boldsymbol{\theta})$ is represents available knowledge about $\boldsymbol{\theta}$ in the absence of $\boldsymbol{d}$; $p(\boldsymbol{d}|\boldsymbol{\theta})$ is the likelihood which represents the probability of observing the data given a certain value of $\boldsymbol{\theta}$, modelled with equation (4.6); and $p(\boldsymbol{\theta}|\boldsymbol{d})$ is the posterior probability distribution, that is the updated probability of $\boldsymbol{\theta}$ informed by the data. The posterior is not a single parameter vector, but a distribution over the parameter space. Therefore, when a representative realization of control parameters must be chosen, one reasonable choice is the maximum a posteriori (MAP) estimate of $p(\boldsymbol{\theta}|\boldsymbol{d})$. Since we assumed that the noise elements are i.i.d., the likelihood function can be written as $p(\boldsymbol{d}|\boldsymbol{\theta}) = p(d_1|\boldsymbol{\theta}) \cdot p(d_2|\boldsymbol{\theta}) \cdot ...p(d_{N_d}|\boldsymbol{\theta})$. Furthermore, we assumed that they are normally distributed with standard deviation $\sigma_{\exp}$ with mean given by $\mathcal{B}(\boldsymbol{\theta}) := \mathcal{B}(\hat{\boldsymbol{U}}(\boldsymbol{\theta}))$. Hence the likelihood is

$$p(\boldsymbol{d}|\boldsymbol{\theta}) = \left(\frac{1}{\sigma_{\exp}\sqrt{2\pi}}\right)^{N_d} \exp\left\{-\sum_{i=1}^{N_d}\frac{[\mathcal{B}(\boldsymbol{\theta})_i - d_i]^2}{2\sigma_{\exp}^2}\right\}. \tag{4.8}$$

In case of uninformative objective priors, we have that $p(\boldsymbol{\theta}|\boldsymbol{d}) \propto p(\boldsymbol{d}|\boldsymbol{\theta})$, and the MAP estimate can be found by minimizing the negative of the exponent of the likelihood function as

$$\min_{\boldsymbol{\theta}} \hat{\mathcal{J}} = \min_{\boldsymbol{\theta}} \sum_{i=1}^{N_d}\frac{[\mathcal{B}(\boldsymbol{\theta})_i - d_i]^2}{2\sigma_{\exp}^2}. \tag{4.9}$$

If, on the other hand, we choose to specify a prior probability density function for our control parameters $\boldsymbol{\theta}$, and we assume they are independent and normally distributed with mean given by $\theta_{j,\text{prior}}$ for $j = 1, ..., N_m$, and standard deviation $\sigma_{j,\theta}$, the MAP can be obtained as

$$\min_{\boldsymbol{\theta}} \mathcal{J} = \min_{\boldsymbol{\theta}} \sum_{i=1}^{N_d}\frac{[\mathcal{B}(\boldsymbol{\theta})_i - d_i]^2}{2\sigma_{\exp}^2} + \sum_{j=1}^{N_m}\frac{\left(\theta_{j,\text{true}} - \theta_{j,\text{prior}}\right)^2}{2\sigma_{j,\theta}^2}. \tag{4.10}$$

The second term in (4.10) acts as a regularization term that penalizes departures of the the parameter vector from its presumed value. The methodologies presented in Section 4.2.2 and 4.2.3 have an objective function similar to that of (4.10). In general, the type of prior specified determines the form of the regularization term, thus affecting the outcome of the minimization problem. The methodology presented in Section 4.2.4 uses a combination of Gaussian and gamma distributions for its priors and thus will present a different form of the regularization term.

4.2.2 Turbulent Production Perturbation (TPP) Method

For a general $k - \omega$ turbulence model, the structure of the transport equations for k and ω is:

$$\frac{D(\rho k)}{Dt} = P_k(\boldsymbol{U}) - D_k(\boldsymbol{U}) + T_k(\boldsymbol{U}) \tag{4.11}$$

$$\frac{D(\rho \omega)}{Dt} = P_\omega(\boldsymbol{U}) - D_\omega(\boldsymbol{U}) + T_\omega(\boldsymbol{U}), \tag{4.12}$$

where $P_i(\cdot)$, $D_i(\cdot)$, and $T_i(\cdot)$ are the production, destruction, and cross-production terms, respectively. Following Duraisamy and co-workers [14, 15], a multiplicative corrective term is introduced in the turbulence model in order to correct the functional form of the model discrepancy. This is achieved by re-writing the production term in one of the transport equations, for example as $\beta(\boldsymbol{x}) \cdot P_\omega(\boldsymbol{U})$, with β being a spatially-varying scalar field defined everywhere in the domain. The corrective term can take both positive and negative values, thus being able to influence the balance of terms of the transport equation. After the discretization of the RANS equations, $\boldsymbol{\beta}$ becomes a high-dimensional vector, with as many elements as the mesh points. Hence, in this case $\boldsymbol{\theta} = \boldsymbol{\theta}_{\text{TPP}} \equiv \boldsymbol{\beta}$. We take as prior $\boldsymbol{\theta}_{\text{TPP}} \sim \mathcal{N}(\mathbf{1}, \sigma_\beta^2 \boldsymbol{I})$ so that the objective function in (4.10) becomes:

$$\mathcal{J} = \sum_{i=1}^{N_d} \frac{[\mathcal{B}(\boldsymbol{\theta})_i - d_i]^2}{2\sigma_{\text{exp}}^2} + \sum_{j=1}^{N_m} \frac{\left(\beta_j - 1.0\right)^2}{2\sigma_\beta^2} \tag{4.13}$$

where N_d, N_m are the number of high-fidelity data and mesh points, respectively, and the value of σ_β is based on the user's knowledge of the particular problem at hand.

In practice, this technique re-calibrates the balance of terms within the transport equation, thus correcting functional errors. It has been applied for a variety of test cases [16, 17, 19], proving to be robust and effective. This is why we chose it as a reference for comparing the performances of the two techniques presented in Section 4.2.3 and Section 4.2.4.

4.2.3 Anisotropy Tensor Perturbation (ATP) Method

The correction proposed in Section 4.2.2 can influence the balance of terms in the turbulent transport equations. However, its range of action is constrained by the Boussinesq hypothesis, and the correction can only address functional errors. Structural errors can be tackled by directly correcting the values of the Reynolds stress tensor computed by a turbulence model. To this end, it is useful to decompose R_{ij} into factors determining its amplitude, shape, and orientation [35]. The Reynolds stress tensor is a symmetric positive-semidefinite tensor and, as such, can be decomposed in an anisotropic and isotropic components as

$$R_{ij} = 2k \left(b_{ij} + \frac{\delta_{ij}}{3} \right) \tag{4.14}$$

65

where $b_{ij} = R_{ij}/2k - \delta_{ij}/3$ is the normalized anisotropy tensor, and the tilde notation has been omitted for simplicity. The symmetry of the Reynolds stress implies b_{ij} is also symmetric and the trace of the turbulence anisotropy is zero by construction. The requirement of physical realizability imposes that R_{ij} has to be positive semi-definite, which can be expressed through constraints on the elements of b_{ij}, namely that $b_{ij} \in [-1/3, 2/3]$ for $i = j$, and $b_{ij} \in [-1/2, 1/2]$ for $i \neq j$ [36]. In addition, the anisotropy tensor can be factored into

$$\boldsymbol{b} = \boldsymbol{X}\boldsymbol{\Lambda}\boldsymbol{X}^T \tag{4.15}$$

where $\boldsymbol{X}$ is a matrix whose columns are orthonormal eigenvectors, and $\boldsymbol{\Lambda}$ is the diagonal matrix of real eigenvalues such that $\lambda_1 \geq \lambda_2 \geq \lambda_3$. Since b_{ij} has zero trace, then we can write $\lambda_3 = -(\lambda_1 + \lambda_2)$. The eigenvalues of the Reynolds stress (φ_i) and those of the turbulence anisotropy (λ_i) are related via

$$\lambda_i = \frac{\varphi_i}{2k} - \frac{1}{3}. \tag{4.16}$$

These considerations permit to describe different limiting behaviors of turbulence in relation to φ_i, which can be visualized using the barycentric map, as explained in Section 2.2. In order to correct the Reynolds stress tensor computed with a turbulence model, we perturb R_{ij} computed from a precursor RANS simulation as

$$R_{ij}^* = 2k^* \left(\boldsymbol{X}^* \boldsymbol{\Lambda}^* \boldsymbol{X}^{\top*} + \frac{\delta_{ij}}{3} \right), \tag{4.17}$$

where $k^* = k + \Delta k$, $\boldsymbol{\Lambda}^*$ is the matrix of perturbed eigenvalues, and $\boldsymbol{X}^*$ is the matrix of perturbed eigenvectors. The perturbed eigenvalues are implicitly defined through perturbations to the coordinates of the barycentric map $\boldsymbol{x}_B^* = (x_B + \Delta x_B, y_b + \Delta y_B)$. The perturbed eigenvector matrix is defined as $\boldsymbol{X}^* = \boldsymbol{Q}^*\boldsymbol{X}$, where $\boldsymbol{Q}$ is a rotation matrix expressed by a combination of the elements of the unit quaternion

$$\begin{aligned} \boldsymbol{h} &= \left[\cos\frac{\phi}{2}, n_1 \sin\frac{\phi}{2}, n_2 \sin\frac{\phi}{2}, n_3 \sin\frac{\phi}{2} \right] = \\ &= \cos\frac{\phi}{2} + n_1 \sin\frac{\phi}{2}\boldsymbol{i} + n_2 \sin\frac{\phi}{2}\boldsymbol{j} + n_3 \sin\frac{\phi}{2}\boldsymbol{k} = \\ &= h_r + h_i\boldsymbol{i} + h_j\boldsymbol{j} + h_k\boldsymbol{k}. \end{aligned} \tag{4.18}$$

Given two sets of orthonormal eigenvectors $\boldsymbol{X}$ and $\boldsymbol{X}^*$ sharing the same origin O, the Euler's rotation theorem states that there exists a unique axis of *unit* vector $\boldsymbol{n}$ and angle ϕ such that $\boldsymbol{X}^*$ can be obtained by rotating $\boldsymbol{X}$ by ϕ about an axis $\boldsymbol{n}$ that runs through the origin O. The rotation matrix is defined as:

$$\boldsymbol{Q} = \begin{pmatrix} 1 - 2(h_j^2 + h_k^2) & 2(h_ih_j - h_kh_r) & 2(h_ih_k + h_jh_r) \\ 2(h_ih_j + h_kh_r) & 1 - 2(h_i^2 + h_k^2) & 2(h_jh_k - h_ih_r) \\ 2(h_ih_k - h_jh_r) & 2(h_jh_k + h_ih_r) & 1 - 2(h_i^2 + h_j^2) \end{pmatrix}. \tag{4.19}$$

In 2D, the only parameter needed to uniquely identify Q is the rotation angle ϕ, since any rotation can only be about the z-axis such that $n_1 = n_2 = 0$ and $n_3 = 1$. The baseline rotation matrix has $\phi = 0$ and thus coincides with the identity matrix, i.e. $Q = I$, and Q^* is constructed by perturbing the rotation angle and the vector components as $\phi + \Delta\phi$, $n_i + \Delta n_i$ for $i = 1, 2, 3$. Note that representing the eigenvector perturbations as a rigid body rotation automatically preserves their orthonormality. With this formulation structural errors in the modeling of turbulence can be corrected by directly assimilating perturbations to the eigenvectors and eigenvalues of the baseline Reynolds stress tensor. Theoretically, once a perturbed Reynolds stress tensor is computed one can run a CFD simulation without a turbulence model. In practice, however, this makes the simulation difficult to converge as shown in the work of Symon et al. [23]. Hence, a turbulence model is still used for stabilizing the RANS simulation via an adaptive under-relaxation technique. This consists in expressing the Reynolds stress tensor as

$$R_{ij} \approx (1 - \gamma)R_{ij}^{\text{ev}} + \gamma R_{ij}^* \tag{4.20}$$

where $\gamma_n = \gamma_{\max} \min\left\{1, \frac{n}{n_{\max}}\right\}$, and $n_{\max}$ is the iteration count after which γ is fixed to the value of $\gamma_{\max}$. Note that the value of k^* in (4.14) could, in principle, be assimilated as well. However, in this work, it is extracted from the transport equation of the turbulence model and hence $\Delta k = 0$. Furthermore, the same Reynolds stress tensor computed in (4.20) is also used in the turbulent transport equations of k and ω to compute a modified production term, in line with the approach of Mishra et al. [37], and Kaandorp & Dwight [4].

In the ATP technique, the vector of control parameters comprehends six perturbation fields: two for the perturbation of the barycentric coordinates, and four for the perturbations of the eigenvectors. Hence, the total number of control variables is six times the number of mesh points and $\boldsymbol{\theta} = \boldsymbol{\theta}_{\text{ATP}} \equiv [\Delta\boldsymbol{x}_B, \Delta\boldsymbol{y}_B, \Delta\boldsymbol{\phi}, \Delta\boldsymbol{n}_1, \Delta\boldsymbol{n}_2, \Delta\boldsymbol{n}_3]^\top$. We assume the priors of each random field of $\boldsymbol{\theta}_{\text{ATP}}$ to be $\Delta\boldsymbol{x}_B \sim \mathcal{N}(\boldsymbol{0}, \sigma_{x_B}^2 \boldsymbol{I})$, $\Delta\boldsymbol{y}_B \sim \mathcal{N}(\boldsymbol{0}, \sigma_{y_B}^2 \boldsymbol{I})$, $\Delta\boldsymbol{\phi} \sim \mathcal{N}(\boldsymbol{0}, \sigma_\phi^2 \boldsymbol{I})$, $\Delta\boldsymbol{n}_i \sim \mathcal{N}(\boldsymbol{0}, \sigma_{n_i}^2 \boldsymbol{I})$ for $i = 1, 2, 3$, we can write the objective function in (4.10) as:

$$\mathcal{J} = \sum_{i=1}^{N_d} \frac{[\mathcal{B}(\boldsymbol{\theta})_i - d_i]^2}{2\sigma_{\exp}^2} + \sum_{j=1}^{N_m} \left[\frac{\Delta\phi_j^2}{2\sigma_\phi^2} + \frac{\Delta x_{B,j}^2}{2\sigma_{x_B}^2} + \frac{\Delta y_{B,j}^2}{2\sigma_{y_B}^2} + \frac{\Delta n_{1,j}^2}{2\sigma_{n_1}^2} + \frac{\Delta n_{2,j}^2}{2\sigma_{n_2}^2} + \frac{\Delta n_{3,j}^2}{2\sigma_{n_3}^2} \right], \tag{4.21}$$

which has the same structure of (4.13), but a different regularization term due to a different choice of design variables.

4.2.4 Random Matrix Perturbation (RMP) Method

In general, a Reynolds stress tensor computed with an eddy-viscosity model may not be physically realizable [38]; that is, its eigenvalues may lie outside of the barycentric triangle. The framework presented in Section 4.2.3 does not guarantee the realizability of R_{ij}, and additional constraints must be enforced for this to happen. For example, every time

a point is displaced outside of the barycentric map by the perturbations to the barycentric coordinates, it could be projected back to the closest border of the triangle [20]. The ideal solution is a procedure that automatically guarantees realizability without imposing additional constraints. This is the case for the random matrix approach [24, 39], which models the Reynolds stress tensor as a random matrix defined on the set $\mathbb{M}_d^{+0}$ of positive semi-definite matrices of rank $d-1$, where d is the spatial dimension of the problem. Note that only the positive definite case is considered here since it is easily obtainable from a positive semi-definite matrix by adding a small positive quantity on its diagonal elements.

Xiao et al. [24] demonstrated that this constraint is sufficient to guarantee the realizability of each realization of the random matrix. Furthermore, it allows one to impose the minimum amount of constraints on the prior of the control parameters, thus making the data assimilation procedure able to explore wider portions of the barycentric map. This is achieved by using the maximum entropy principle to specify the distribution of the Reynolds stress tensor, which states that, among all the probability density functions (PDFs) mapping from $\mathbb{M}_d^{+0}$ to $\mathbb{R}^+$, the most non-committal is the one that satisfies all available constraints without introducing additional artificial ones. This is obtained by maximizing the entropy $S(p)$ of the PDF $p(\boldsymbol{R})$ of a random Reynolds stress tensor $[\boldsymbol{R}]$:

$$S(p) = -\int_{\mathbb{M}_d^{+0}} p(\boldsymbol{R}) \ln p(\boldsymbol{R}) d\boldsymbol{R} \tag{4.22}$$

where $\boldsymbol{R}$ is a realization of the random Reynolds stress tensor, and we use the notation $[\cdot]$ for random matrices. For RANS turbulence modeling, the constraints that must be satisfied are:

- All realizations $\boldsymbol{R}$ must be realizable. This constraint is automatically satisfied by defining the random Reynolds stress tensor on the set $\mathbb{M}_d^{+0}$.

- The integral of the PDF over the set must be equal to unity: $\int_{\mathbb{M}_d^{+0}} p(\boldsymbol{R}) d\boldsymbol{R} = 1$.

In practice, it is easier to work with a normalized positive definite random matrix whose mean is the identity matrix, i.e. $\mathbb{E}\{[\boldsymbol{G}]\} = \boldsymbol{I}$. We can write:

$$[\boldsymbol{R}] = \boldsymbol{L}_R^\top [\boldsymbol{G}] \boldsymbol{L}_R \tag{4.23}$$

where $\boldsymbol{L}_R$ is an upper triangular matrix with non-negative diagonal entries obtained from the Cholesky factorization of $\boldsymbol{R}$, which is assumed to be the best estimation of $[\boldsymbol{R}]$ obtained from a precursor RANS simulation and is taken to be the mean of $[\boldsymbol{R}]$, i.e. $\mathbb{E}\{[\boldsymbol{R}]\} = \boldsymbol{R}$. The probability density function of $[\boldsymbol{G}]$ must also satisfy the maximum entropy principle. Taking this into consideration, and after using the Cholesky factorization such that $[\boldsymbol{G}] = [\boldsymbol{L}]^\top [\boldsymbol{L}]$, it can be shown that [24]:

- The off-diagonal elements of the upper triangular random matrix $[\boldsymbol{L}]$ are $[L_{ij}] = \sigma_d w_{ij}$, with $\sigma_d = \delta \times (d+1)^{-1/2}$, δ being a user-defined dispersion parameter such that $0 < \delta < \sqrt{2}/2$ for $d = 3$, and w_{ij} are independent Gaussian random variables with zero mean and unit variance.

- The diagonal elements are $[L_{ii}] = \sigma_d \sqrt{2u_i}$, where u_i is a positive-valued gamma random variable with the following probability density function:

$$p(u) = \mathbb{1}_{\mathbb{R}^+}(u) \frac{\zeta^\alpha u^{\alpha-1} \exp(-\zeta u)}{\Gamma(\alpha)} \tag{4.24}$$

which is the classical expression of a gamma PDF with $u, \alpha, \zeta > 0$. In the random matrix approach we have $\zeta = 1$ and $\alpha = \frac{d+1}{2\delta^2} + \frac{1-i}{2}$. Note that $\mathbb{1}_{\mathbb{R}^+}(u)$ is an indicator function, i.e. it is one if $u \in \mathbb{R}^+$, and zero otherwise.

The RMP technique uses the three diagonal and three off-diagonal elements of $[\boldsymbol{L}]$ at every mesh point as control parameters. Hence, the total number of control variables is six times the number of mesh points and $\boldsymbol{\theta} = \boldsymbol{\theta}_{\text{RMP}} \equiv [\boldsymbol{L_{11}}, \boldsymbol{L_{12}}, \boldsymbol{L_{13}}, \boldsymbol{L_{22}}, \boldsymbol{L_{23}}, \boldsymbol{L_{33}}]^\top$. Because the prior of the diagonal elements is not Gaussian, the regularization term of the objective function does not have the structure of (4.10), but rather:

$$\mathcal{J} = \sum_{i=1}^{N_d} \frac{[\mathcal{B}(\boldsymbol{\theta})_i - d_i]^2}{\sigma_{\text{exp}}^2} + \sum_{j=1}^{N_m} \left\{ \frac{L_{12,j}^2 + L_{13,j}^2 + L_{23,j}^2 + L_{11,j}^2 + L_{22,j}^2 + L_{33,j}^2}{2\sigma_d^2} + \right.$$
$$\left. - \ln \left[\mathbb{1}_{\mathbb{R}_0^+}(L_{11,j}) L_{11,j}^{s_1-1} \cdot \mathbb{1}_{\mathbb{R}_0^+}(L_{22,j}) L_{22,j}^{s_2-1} \cdot \mathbb{1}_{\mathbb{R}_0^+}(L_{33,j}) L_{33,j}^{s_3-1} \right] \right\}, \tag{4.25}$$

where $s_i = \frac{4}{\delta^2} + 1 - i$, L_{ij} are realizations of the random variables $[L_{ij}]$, and we assumed no spatial correlation for the elements of $[\boldsymbol{L}]$. The complete derivation of the objective function can be found in Appendix A. The presence of the logarithmic term penalizes negative and small values of the diagonal terms so as to keep them positive. In this way, $\boldsymbol{G}$ will be positive definite and so will $\boldsymbol{R}$, thus automatically making it realizable, without the need to impose additional constraints as for the ATP method.

4.3   Results

In this Section, the data assimilation techniques proposed in Section 4.2 are used to reconstruct the flow field of cases for which eddy viscosity models are known to perform poorly. These are the flow over an S809 airfoil at a high angle of attack, and the separated flow behind a wall-mounted hump. Singh & Duraisamy used the first case in their work [15, 40], and it was chosen to validate the novel methods presented in this paper. The second test case is part of the *NASA Turbulence Modeling Resource* database [41], and it is known to be challenging for eddy viscosity turbulence models. While the frameworks presented in this dissertation can be used with different types of high-fidelity data (e.g. velocity, pressure, skin friction), we choose to use only surface pressure data since these are one of the most common data obtainable from experiments. This choice also allows us to observe to what extent the data assimilation frameworks of this study can reconstruct unobserved quantities such as the velocity field.
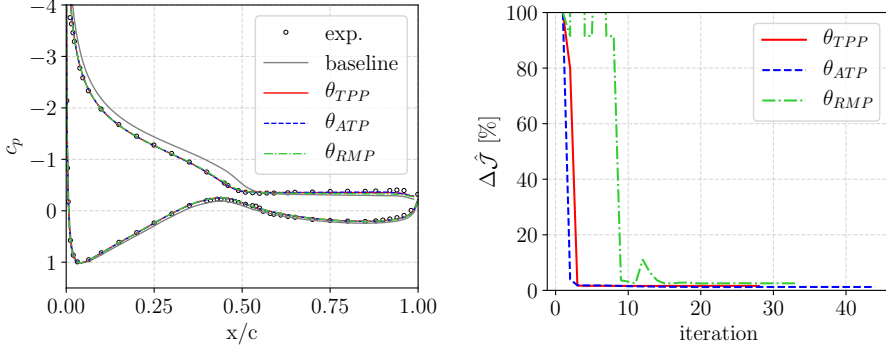
Figure 4.1: Left: Pressure coefficient over the S809 airfoil as computed by the TPP, ATP, RMP methods. Right: Optimization history as a percentage reduction with respect to the initial value of $\hat{\mathcal{J}}$.

4.3.1 S809 Airfoil

The S809 airfoil is commonly used for the design of the blades of horizontal axis wind turbines and was chosen by Singh & Duraisamy [15, 40] as the test case for their field-inversion machine-learning (FIML) framework. Experimental data at $Re_c = 2 \times 10^6$, $M_\infty = 0.2$, and at a variety of angles of attack are available from the study of Somers et al. [42]. In the present case, the inversion is performed at the highest angle of attack of the database, i.e. $\alpha_\infty = 14.24°$, for which an adverse pressure gradient induces a large region of separated flow. The same structured C-grid with approximately 5.5×10^4 points as in Singh & Duraisamy [15] was used. The grid convergence index (GCI) based on the separation location is approximately 2% and can be used as an estimation of the discretization error [43]. The pressure coefficient from the experiment of Somers et al. [42] is chosen as training data for the objective function. Because extracting the data is prone to errors in proximity of regions with high gradients, only the suction pressure data in the range $0.05 < x/c < 0.8$ were used. The value of γ was set to 0.5 for both the ATP and RMP methods, $\sigma_{\exp} = 10^{-2}$, and all the other standard deviations were set to unity.

Figure 4.1 shows the baseline and assimilated pressure coefficients over the airfoil and the optimization histories for the different methods. The baseline SST model does a poor job and overpredicts the pressure on the suction side as well as the location of the separation point. All three assimilations are capable of correcting this error, and no substantial differences among them are observed. However, by looking at Table 4.1, which shows the values of $\hat{\mathcal{J}}$, one can notice that the ATP method has the best agreement with the experimental data, followed by the TPP method and the RMP method. The RMP method has a higher $\hat{\mathcal{J}}$ than the TPP method because the optimization converged to a local minimum. This is a known problem of gradient-based optimizations, for which reaching a global optimum remains a subject of research.
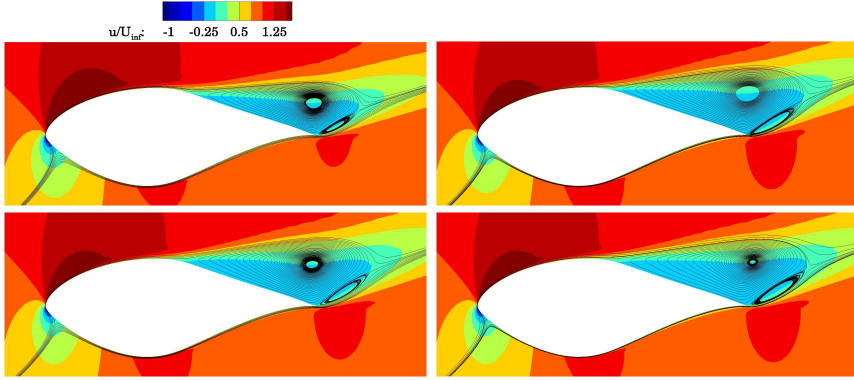
Figure 4.2: Normalized streamwise velocity as computed by the baseline SST model (top left), the TPP (top right), the ATP (bottom left), and the RMP (bottom right) methods.

Table 4.1: Comparison of the value of the error function $\hat{\mathcal{J}}$, the lift coefficient c_L, the separation location x/c, and the number of optimization iterations among the baseline result and the MAP of the TPP, ATP, and RMP methods.

case	$\hat{\mathcal{J}}$	c_L	x/c	iter
Baseline SST	1.416	1.243	0.55	n.a.
TPP	0.0227	1.105	0.49	28
ATP	0.0163	1.108	0.50	44
RMP	0.0298	1.101	0.51	33

Figure 4.2 compares the near-wall streamlines for the baseline SST model, and the TPP, ATP, and RMP methods. The DA results display a significantly larger separation bubble than that of the baseline. This implies that the flow separates earlier, and thus that turbulent production is decreased.

In the experiments, the separation is observed at mid-chord, while it is predicted to be at $x/c = 0.55$ by the baseline SST model. All the assimilations, on the other hand, predict the separation location to be very close to $x/c = 0.50$, as shown in the last column of Table 4.1. The same Table also compares the posterior lift coefficients c_L, the experimental one being $c_{L,\text{exp}} = 1.083$. Once again, we observe a decisive improvement over the baseline results.

Figure 4.3 shows the perturbations to the barycentric coordinates Δx_b, Δy_b and the unit quaternion component h_r for the ATP and RMP methods. The former two are a function of the eigenvalue perturbations, while the latter is a function of the eigenvector perturbations which, for 2D cases, are given by a rotation about the axis perpendicular to the domain. The anisotropy perturbations are concentrated close to the wall and in the separated region, and are much stronger for the ATP method than the RMP method. This is in line with the fact that the RMP method has reached a different local minimum than
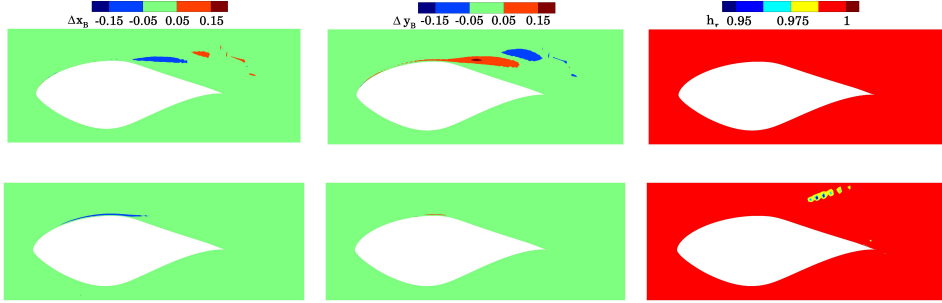
Figure 4.3: Perturbations to barycentric coordinates Δx_B (left), Δy_B (middle), and h_r (right) for the ATP (top) and RMP (bottom) methods. The components h_i, h_j, and h_k are omitted here since, for 2D flows, the rotation axis is aligned along spanwise direction.

the ATP method, due to a different, possibly rougher, topology of the optimization space. For both methods, the Δx_B perturbations tend to move the anisotropy towards the axisymmetric contraction line (i.e. the line joining the $2c$ and $3c$ corners of the barycentric map) and away from the two component limit (i.e. the line connecting the $2c$ and $1c$ corners of the barycentric map). The eigenvalue perturbations are driving the correction to the turbulence model, since the value of h_r is close to unity everywhere in the domain for both the ATP and RMP methods. The only noticeable perturbations are visible for the RMP method and are located at the edge of the separated region, in an area untouched by the anisotropy perturbations. For the sake of completeness, the corrective field β from the TPP method is presented in Appendix B.

4.3.2 Hump in a Channel

The flow over a 2D hump is one of the test cases selected by NASA for the validation of turbulence models. It presents separated flow behind a smooth hump protruding from a flat wall, as shown in Fig. 4.4. Linear eddy viscosity turbulence models underpredict the turbulent stresses in the separated region, thus causing too-long a separation bubble. The domain consists of a rectangular channel with an inlet and an outlet, a solid bottom wall with the hump, and an upper boundary to which a symmetry boundary condition is applied. The Reynolds number based on the hump length c is 9.36×10^5, and the Mach number is 0.1. The structured mesh has 4.5×10^4 points, with $y^+ \approx 0.7$. The upstream length of the channel was set to allow the natural development of the fully-turbulent boundary layer in order to achieve the experimental boundary layer thickness of $\delta^{99} = 0.0035$ m at $x/c = -2.14$ [44]. The grid convergence index (GCI) based on the reattachment location is less than 1%. For the assimilation, experimental pressure coefficients on the surface of the hump in the interval $-0.8 < x/c < 2.2$ are used as training data (note that $x/c = 0$ corresponds to the hump's leading edge). The value of σ_{exp} is set to 10^{-3}, as specified in the experiment of Greenblatt et al. [44], while all the other standard deviations are set to unity.
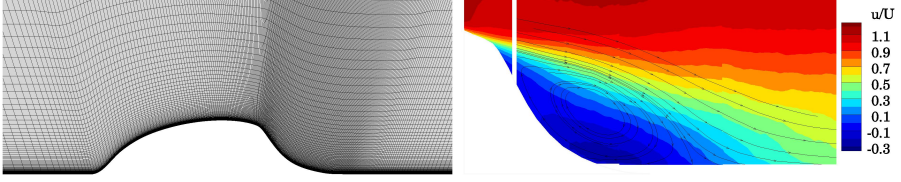
Figure 4.4: Close-up of the mesh in proximity of the hump (left) and the stream-wise velocity field obtained from PIV [45] (right).
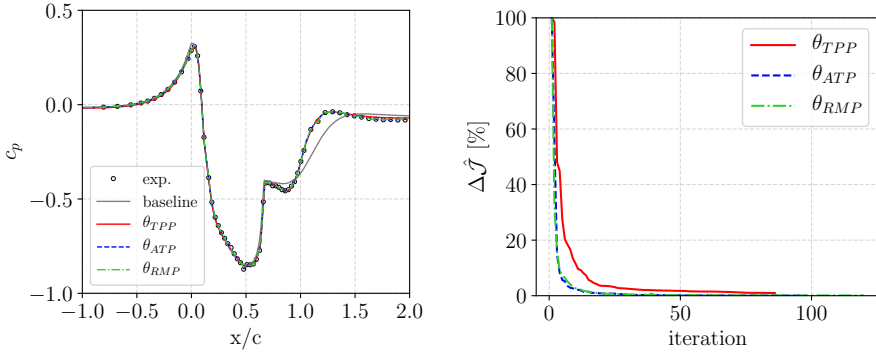

Figure 4.5: Left: Pressure coefficient over the hump as computed by the TPP, ATP, RMP methods. Right: Optimization history as a percentage reduction with respect to the initial value of $\hat{\mathcal{J}}$.

The surface pressure coefficient c_p over the hump for the three data assimilations is shown in Fig. 4.5. The baseline SST model overpredicts the pressure valley at $x/c \approx 0.8$ and underpredicts the pressure peak at $x/c \approx 1.3$. This is a known issue with eddy viscosity models in presence of separated flow. All data assimilation methods significantly improve the baseline results, with the ATP and RMP methods showing an almost perfect agreement with the reference. In particular, we highlight their ability to capture subtle features such as the pressure kinks at $x/c = 0.5$ and $x/c = 1.2$. The TPP method obtains better results than the baseline but not as good as the two methods presented in this work, especially downstream of the reattachment point and in correspondence of the pressure kinks.

Figure 4.6 shows the normalized stream-wise velocity in the separated region. The baseline model predicts too strong a reversed flow after $x/c = 1.0$, which causes a large separation region. All the data assimilations do a better job, in particular for $x/c > 0.9$. The ATP and RMP methods predict similar velocity profiles, with an excellent agreement for $y/c > 0.10$, although they predict a slower stream-wise velocity in the central part of the region $0.05 \leq y/c \leq 0.10$, where the TPP method is slightly more accurate. In
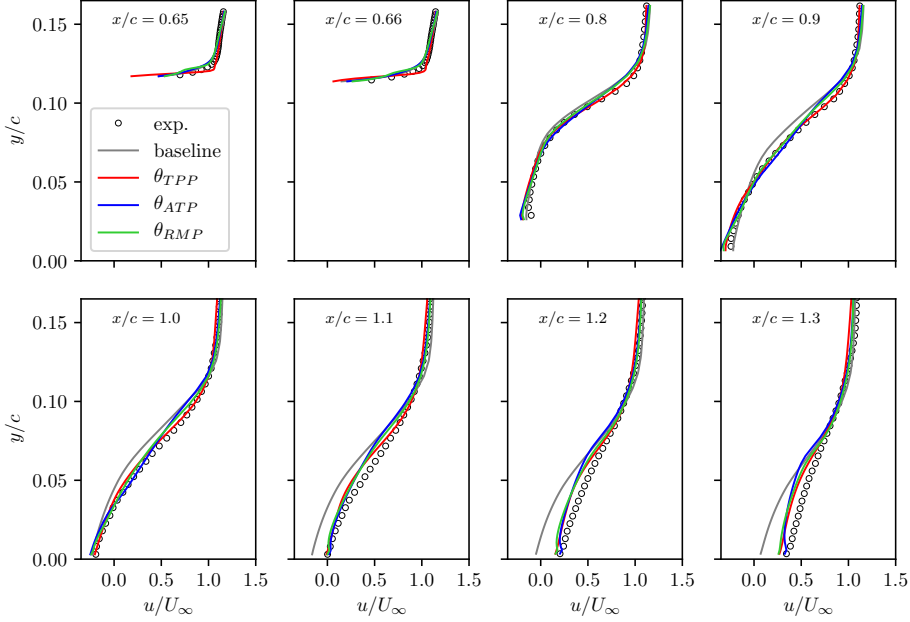
Figure 4.6: Stream-wise velocity profiles in the separation bubble.

any case, the differences among the DA methods are minimal, whereas the improvement over the baseline is evident. This result also demonstrates that it is sometimes possible to use only high-fidelity pressure data to better predict unobserved quantities such as the velocity.

Figure 4.7 shows that, for the ATP and RMP methods, the anisotropy perturbations are concentrated in the recirculation region behind the hump and persist downstream of it in the wake of the flow. The ATP method is capable of stronger perturbations to Δx_B and Δy_B than the RMP method, although they are quantitatively similar. On the other hand, no significant perturbations to h_r can be observed for both methods, thus suggesting that, for this particular test case, the eigenvector orientations remain aligned with the mean rate of strain and do not play a significant role in correcting the errors of the turbulence model.

Figure 4.8 shows the barycentric map of the points extracted along a vertical line at $x/c = 0.8$. The Reynolds stress tensor was computed using (4.20) with $\gamma = 0.5$ for the RMP and ATP methods, and $\gamma = 0$ for the TPP method. The ATP method perturbs the barycentric coordinates of the sampled points away from the plane strain line, towards the $1c$ corner. On the contrary, the RMP method translates all the points to the left of the plane strain line, away from the $1c$ corner. It is interesting to note that the perturbations from the baseline, i.e. the distance of the ATP and RMP barycentric coordinates from the plane strain line, are relatively small. Nonetheless, they are sufficient to generate a Reynolds
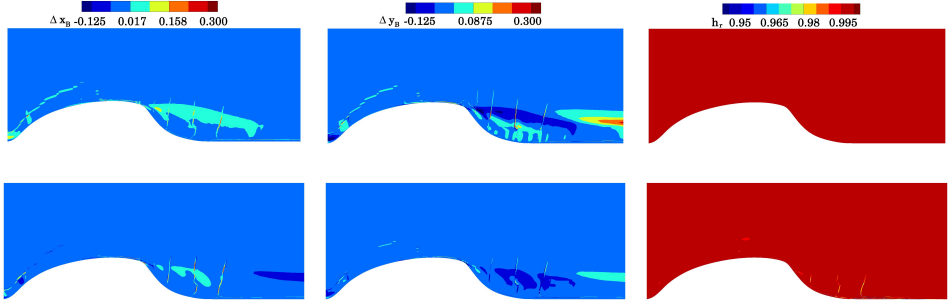
Figure 4.7: Perturbations to barycentric coordinates Δx_B (left), Δy_B (middle), and h_r (right) for the ATP (top) and RMP (bottom) methods. The components h_i, h_j, and h_k are omitted here since, for 2D flows, the rotation axis is aligned along spanwise direction.

stress tensor capable of dramatically improving the agreement with the high-fidelity data, as shown in Fig. 4.5. This suggests that it could be sufficient to explore a neighborhood of the plane strain line to significantly improve eddy viscosity models, at least for 2D flow problems.

In principle, the ATP and RMP techniques can perturb the points in the barycentric triangle in the same way. This, however, does not happen, most likely due to different solution-space topologies of the two optimization problems, which cause the optimized result to lay in two different local minima.

Figure 4.9 shows the normalized streamwise velocity field in proximity of the hump. The results of the three DAs are qualitatively similar, as they all have a smaller recirculation region immediately behind the hump than the baseline case, with approximately the same size of the one obtained from PIV data shown in Fig. 4.4.

Table 4.2 shows the values of the error function $\hat{\mathcal{J}}$, the stream-wise location of the reattachment point, and the number of optimization iterations required to compute the MAP. It is evident that using data assimilation techniques to correct the errors due to turbulence models is an effective strategy, and the ATP and RMP methods do a better job than the TPP because they are not subject to the limitations of the eddy viscosity hypothesis. In the experiments, the recirculation region extended to $x/c = 1.11 \pm 0.003$, and the DAs are all capable of predicting this characteristic more accurately than the baseline by reducing the size of the recirculation bubble.

Furthermore, Tables 4.1 and 4.2 show that the number of optimization iterations necessary to meet the stopping criteria for the ATP and RMP methods is higher than for the TPP method; hence a longer computational time is needed for those techniques. On the other hand, the time per iteration of the ATP and RMP methods is practically the same as that of the TPP method, because only few additional matrix products are needed for their implementation.

In conclusion, we observed that DA techniques are effective for reconstructing the flow field of a particular test case by correcting the errors due to the turbulence model
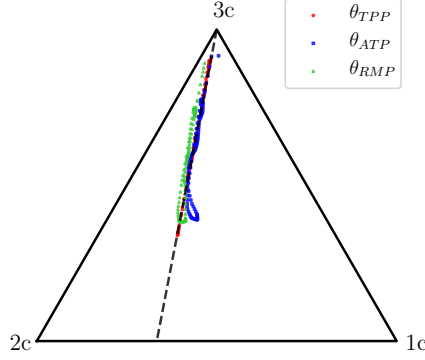
Figure 4.8: Barycentric map of R_{ij} extracted along a vertical line at $x/c = 0.8$ in the interval $0 < y/c < 1.4$.
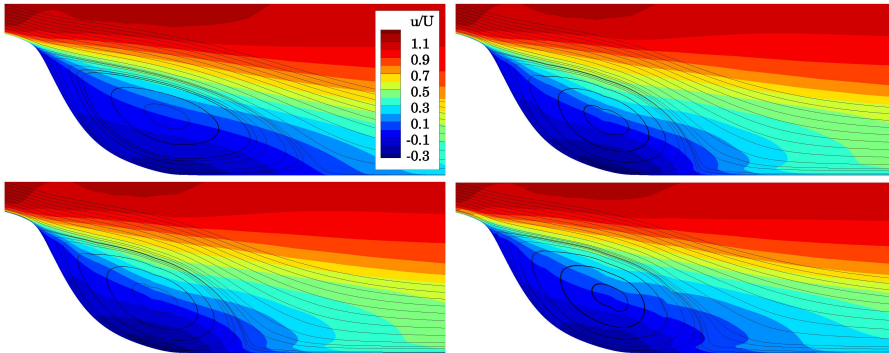

Figure 4.9: Normalized streamwise velocity behind the hump as computed by the baseline SST model(top left), the TPP (top right), the ATP (bottom left), and the RMP (bottom right) methods.

Table 4.2: Comparison of the value of the error function $\hat{\mathcal{J}}$, the separation location x/c, and the number of optimization iterations among the baseline result and the MAP of the TPP, ATP, and RMP methods.

case	$\hat{\mathcal{J}}$	x/c	iter
Baseline SST	0.8897	1.26	n.a.
TPP	0.0086	1.12	85
ATP	0.0005	1.13	99
RMP	0.0011	1.15	121

using sparse high-fidelity data. In particular, the ATP and RMP methods have a better agreement with the high-fidelity pressure data used in the objective function than the TPP method used as a reference. All the methodologies tested were also able to correct unobserved quantities such as the velocity field, the extent of the recirculation region, and the location of the reattachment point.

4.4 Conclusions

This Chapter presented two novel variational data assimilation frameworks for the reconstruction of turbulent flow fields by correcting functional and structural errors introduced by linear eddy viscosity turbulence models. The two approaches differ from each other in the choice of control parameters: the ATP method uses the eigenvalues and eigenvectors of the normalized anisotropy tensor, while the RMP method uses the components of a positive-definite random matrix that ensures realizability of the Reynolds stress tensor. Two high Reynolds number flow cases known to be hard to simulate with eddy viscosity models were chosen for testing. The ATP and RMP methods showed substantial improvements with respect to the results of a baseline simulation and comparable or better performance than a state-of-the-art variational data assimilation technique used as a reference. In particular, the ATP and RMP frameworks were able to reconstruct extremely well the experimental pressure data used in the objective function, and largely improve the reconstruction of unobserved quantities such as the velocity field, the location of reattachment, and the size of the separation bubble. Furthermore, we noted that only small perturbations to the control parameters were necessary to achieve considerable improvements over the baseline results, and that correcting the eigenvector orientations does not seem to have a decisive influence in improving the reconstruction of the flow field. The ATP and RMP methods are, however, computationally more expensive than the reference data assimilation technique considered due to a six-fold increase in the number of control parameters. Future work involves applying these techniques to 3D test cases and more practical problems such as the correction of wind-tunnel wall interference. This is the topic of Chapter 5.

4.5 Appendix A: Derivation of the RMP Objective Function

In order to fulfill the maximum entropy principle, the random matrix approach requires the specifications of non-normal priors [24]. In our case, we are interested in specifying the priors of the upper triangular matrix $[L]$ obtained from the Cholesky factorization of $[G]$. At this point, we assume that these six random vectors are statistically independent, which means that their probability density functions have the following property:

$$p(L_{ij}) = p(L_{11}, L_{12}, L_{13}, L_{22}, L_{23}, L_{33}) = p(L_{11}) \cdot p(L_{12}) \cdot p(L_{13}) \cdot p(L_{22}) \cdot p(L_{23}) \cdot p(L_{33}),$$

(4.26)

hence we can write, for a single point in the mesh:

$$p(L_{ij}|\boldsymbol{d}) \propto p(\boldsymbol{d}|L_{ij})p(L_{ij}) = p(\boldsymbol{d}|L_{ij}) \cdot p(L_{11}) \cdot p(L_{12}) \cdot p(L_{13}) \cdot p(L_{22}) \cdot p(L_{23}) \cdot p(L_{33}), \quad (4.27)$$

which implies that we can independently specify the probability distribution of each element of $[L]$. Therefore, all we have to do is derive the expressions of $p(L_{ij})$ from those for w_{ij} and u_i.

4.5.1 Off-Diagonal Elements

We saw that $[L_{ij}] = \sigma_d w_{ij}$ with $w_{ij} \sim \mathcal{N}(0,1)$. For a family of normal distributions, if $X \sim \mathcal{N}(\mu, \sigma^2)$ and $Y = aX + b$, with $a, b \in \mathbb{R}$, then $Y \sim \mathcal{N}(a\mu + b, a^2\sigma^2)$. Hence, in this case we have $[L_{ij}] \sim \mathcal{N}(0, \sigma_d^2)$, and therefore:

$$p(L_{ij}) \propto \exp\left(-\frac{(L_{ij})^2}{2\sigma_d^2}\right)$$

(4.28)

4.5.2 Diagonal Elements

We want to obtain the pdf of $[L_{ii}] = \sigma_d \sqrt{2u_i}$, with u_i being a gamma random variable (RV). For gamma RVs, if $X \sim \Gamma(\alpha, \zeta)$, then $cX \sim \Gamma(\alpha, \frac{\zeta}{c})$, with $\alpha, \zeta, c > 0$. Hence $2u_i \sim \Gamma(\alpha, \frac{1}{2}) = \Gamma(\alpha, \frac{\zeta}{2})$.

Furthermore, it holds that if $X \sim \Gamma(\alpha, \zeta)$, then $X^q \sim GG(r, s, t)$ with $r = \frac{1}{\zeta}^q$, $s = \frac{\alpha}{q}$, and $t = \frac{1}{q}$ with $GG(r, s, t)$ being a generalized gamma distribution. The generalized gamma distribution is a continuous probability distribution with three parameters, and

$$p(x; r, s, t) = \mathbb{1}_{\mathbb{R}_0^+}(x)\frac{tx^{s-1}\exp\left(-(\frac{x}{r})^t\right)}{r^s\Gamma(\frac{s}{t})}.$$

(4.29)

Hence, in our case:

$$\sqrt{2u_i} \sim GG\left(\sqrt{\frac{2}{\zeta}}, 2\alpha, 2\right).$$

(4.30)

 Finally, for any probability distribution it holds that if $Y = g(X) = kX$ is the transformation from $X = \{x|x > 0\}$ to $\mathcal{Y} = \{y|y > 0\}$, with inverse $X = g^{-1}(Y) = \frac{Y}{k}$ and Jacobian $\frac{dX}{dY} = \frac{1}{k}$, then the probability distribution of Y is:

$$p_y(y) = p_x(x)\left|\frac{dx}{dy}\right| = p_x(g^{-1}(y))\left|\frac{dx}{dy}\right|. \tag{4.31}$$

In our case we have:

$$
\begin{aligned}
= \sigma_d \sqrt{2u_i} &\sim GG(\frac{y}{\sigma_d}; r, s, t)\left|\frac{1}{\sigma_d}\right| = \frac{ty^{s-1}\exp\left(-(\frac{y}{\sigma_d r})^t\right)}{r^t\sigma_d^{(s-1)}\Gamma(\frac{s}{t})}\left|\frac{1}{\sigma_d}\right| = \\
&= \frac{ty^{s-1}\exp\left(-(\frac{y}{\sigma_d r})^t\right)}{(r\sigma_d)^s\Gamma(\frac{s}{t})} = GG(y; r\sigma_d, s, t)
\end{aligned}
\tag{4.32}
$$

We have the following expressions for r, s, t:

$$
\begin{aligned}
r &= \sqrt{\frac{2}{\zeta}} = \sqrt{2} \\
s_i &= 2\alpha = 2\left(\frac{d+1}{2\delta^2} + \frac{1-i}{2}\right) = \\
&= \frac{d+1}{\delta^2} + 1 - i = \frac{4}{\delta^2} + 1 - i \\
t &= 2
\end{aligned}
\tag{4.33}
$$

Hence we can write out the full expression for $p(L_{ii})$:

$$p(L_{ii}) = \mathbb{1}_{\mathbb{R}_0^+}(L_{ii})\frac{2L_{ii}^{\frac{4}{\delta^2}-i}\exp\left(-\left(\frac{L_{ii}}{\sqrt{2}\sigma_d}\right)^2\right)}{(\sqrt{2}\sigma_d)^{\frac{4}{\delta^2}+1-i}\Gamma\left(\frac{s}{2}\right)}. \tag{4.34}$$

The Gamma function is defined as $\Gamma(z) = \int_0^\infty x^{z-1}e^{-x}dx$ and can be easily approximated once the value of z is fixed. In order to fix the value of z, we need to fix s, which implies choosing a value for the dispersion parameter δ.

4.5.3   The Expression of the Objective Function

These modification have an effect on the expression of the objective function which is derived as the MAP of the posterior PDF.

$$
p(\boldsymbol{x}|\boldsymbol{d}) \propto p(\boldsymbol{d}|\boldsymbol{x})p(\boldsymbol{x}) = \exp\left[-\sum_{i=1}^{N_d}\frac{(\mathcal{B}(\boldsymbol{\theta})_i - d_i)^2}{2\sigma_{\exp}^2}\right]\cdot
$$

$$
\cdot\prod_{j=1}^{N_m} p(L_{11,j})p(L_{12,j})p(L_{13,j})p(L_{22,j})p(L_{23,j})p(L_{33,j}) =
$$

$$
= \exp\left[-\sum_{i=1}^{N_d}\frac{(\mathcal{B}(\boldsymbol{\theta})_i - d_i)^2}{2\sigma_{\exp}^2}\right]\cdot\prod_{j=1}^{N_m}\left[\exp\left(-\frac{L_{12,j}^2}{2\sigma_d^2}\right)\cdot\exp\left(-\frac{L_{13,j}^2}{2\sigma_d^2}\right)\cdot\exp\left(-\frac{L_{23,j}^2}{2\sigma_d^2}\right)\cdot\right.
$$

$$
\left.\cdot\, p(L_{11,j})p(L_{22,j})p(L_{33,j})\right] =
$$

$$
= \exp\left[-\sum_{i=1}^{N_d}\frac{[\mathcal{B}(\boldsymbol{\theta})_i - d_i]^2}{2\sigma_{\exp}^2}\right]\cdot\exp\left[-\sum_{j=1}^{N_m}\frac{L_{12,j}^2 + L_{13,j}^2 + L_{23,j}^2}{2\sigma_d^2}\right]\cdot
$$

$$
\cdot\prod_{j=1}^{N_m}\left[p(L_{11,j})p(L_{22,j})p(L_{33,j})\right] =
$$

$$
= \exp\left[-\sum_{i=1}^{N_d}\frac{(\mathcal{B}(\boldsymbol{\theta})_i - d_i)^2}{2\sigma_{\exp}^2} - \sum_{j=1}^{N_m}\frac{L_{12,j}^2 + L_{13,j}^2 + L_{23,j}^2}{2\sigma_d^2}\right]\cdot
$$

$$
\cdot\prod_{n=1}^{3}\prod_{j=1}^{N_m}\frac{2\cdot\mathbb{1}_{\mathbb{R}_0^+}(\boldsymbol{L}_{nn,j})\cdot\boldsymbol{L}_{nn,j}^{s_n-1}\exp\left[-\left(\frac{\boldsymbol{L}_{nn,j}}{\sigma_d r}\right)^2\right]}{(r\sigma_d)^{s_n}\Gamma(\frac{s_n}{2})} =
$$

$$
= \exp\left[-\sum_{i=1}^{N_d}\frac{(\mathcal{B}(\boldsymbol{\theta})_i - d_i)^2}{2\sigma_{\exp}^2} - \sum_{j=1}^{N_m}\frac{L_{12,j}^2 + L_{13,j}^2 + L_{23,j}^2}{2\sigma_d^2}\right]\cdot
$$

$$
\cdot\prod_{j=1}^{N_m}2^3\exp\left[-\frac{L_{11,j}^2 + L_{22,j}^2 + L_{33,j}^2}{(\sigma_d r)^2}\right]\cdot\prod_{n=1}^{3}\prod_{j=1}^{N_m}\frac{\mathbb{1}_{\mathbb{R}_0^+}(\boldsymbol{L}_{nn,j})\cdot\boldsymbol{L}_{nn,j}^{s_n-1}}{(r\sigma_d)^{s_n}\Gamma(\frac{s_n}{2})} =
$$

$$
= (2^3)^{N_m}\cdot\exp\left[-\sum_{i=1}^{N_d}\frac{(\mathcal{B}(\boldsymbol{\theta})_i - d_i)^2}{2\sigma_{\exp}^2} - \sum_{j=1}^{N_m}\frac{L_{12,j}^2 + L_{13,j}^2 + L_{23,j}^2}{2\sigma_d^2} + \right.
$$

$$
\left.-\sum_{j=1}^{N_m}\frac{L_{11,j}^2 + L_{22,j}^2 + L_{33,j}^2}{(\sigma_d r)^2}\right]\cdot\prod_{n=1}^{3}\prod_{j=1}^{N_m}\frac{\mathbb{1}_{\mathbb{R}_0^+}(\boldsymbol{L}_{nn,j})\cdot\boldsymbol{L}_{nn,j}^{s_n-1}}{(r\sigma_d)^{s_n}\Gamma(\frac{s_n}{2})}.
$$

The MAP estimate is obtained by maximizing the log of the posterior PDF. Since we are interested in a minimization problem, our objective function is the negative of the

logarithm of the posterior:

$$\mathcal{J} = -\ln(p(\boldsymbol{x}|\boldsymbol{d})) = -\ln(2^{3N_m}) + \sum_{i=1}^{N_d} \frac{(\mathcal{B}(\boldsymbol{\theta})_i - d_i)^2}{2\sigma_{\exp}^2} + \sum_{j=1}^{N_m} \frac{L_{12,j}^2 + L_{13,j}^2 + L_{23,j}^2}{2\sigma_d^2} +$$

$$+ \sum_{j=1}^{N_m} \frac{L_{11,j}^2 + L_{22,j}^2 + L_{33,j}^2}{(\sigma_d r)^2} - \sum_{j=1}^{N_m} \ln\left(\prod_{n=1}^{3} \frac{\mathbb{1}_{\mathbb{R}_0^+}(\boldsymbol{L}_{nn,j}) \cdot \boldsymbol{L}_{nn,j}^{s_n-1}}{(r\sigma_d)^{s_n} \Gamma(\frac{s_n}{2})}\right),$$

with $\sigma_d = \delta \times (d+1)^{-1/2} = \frac{\delta}{2}$, and δ being a user-specified dispersion parameter such that $0 < \delta < \sqrt{2}/2$ for $d = 3$; $r = \sqrt{2}$, $s_i = \frac{4}{\delta^2} + 1 - i$, and we used the logarithmic property $\ln(a \cdot b) = \ln(a) + \ln(b)$ for deriving the above expressions. Constant terms do not influence the location of the optima, hence the objective function can be simplified to (4.25).

4.6 Appendix B: Corrective field from TPP method

Figure 4.10 shows the corrective field $\boldsymbol{\beta}$ obtained by using the TPP data assimilation methodology. The results for the s809 airfoil show a thin region close to the surface where $\beta > 1$, thus indicating that Menter's SST turbulence model underpredicts the turbulent dissipation. As a consequence, the flow remains attached to the airfoil for longer and this is the reason why the separation location for the baseline model is located more downstream than that of the TPP method.

In the hump test case, the corrective field is active within the separated region behind the crest of the hump, in the shear layer above the separated region, and in the wake of the flow. The corrective field increases the dissipation in the separated region which makes the flow reattach more upstream than in the baseline case. Furthermore, we observe that the turbulence model underpredicts the turbulent dissipation and overpredicts it in the shear layer above the recirculation region and in the wake of the flow, respectively.

Figure 4.10: Corrective field $\boldsymbol{\beta}$ for the s809 (left) and hump (right) cases.

References

[1] Duraisamy, K., Iaccarino, G., and Xiao, H., "Turbulence modeling in the age of data," *Annual Review of Fluid Mechanics*, Vol. 51, 2019, pp. 357–377.

[2] Ling, J., Kurzawski, A., and Templeton, J., "Reynolds averaged turbulence modelling using deep neural networks with embedded invariance," *Journal of Fluid Mechanics*, Vol. 807, 2016, pp. 155–166.

[3] Wu, J.-L., Sun, R., Laizet, S., and Xiao, H., "Representation of stress tensor perturbations with application in machine-learning-assisted turbulence modeling," *Computer Methods in Applied Mechanics and Engineering*, Vol. 346, 2019, pp. 707–726.

[4] Kaandorp, M. L. and Dwight, R. P., "Stochastic Random Forests with Invariance for RANS Turbulence Modelling," *arXiv preprint arXiv:1810.08794*, 2018.

[5] Schmelzer, M., Dwight, R. P., and Cinnella, P., "Machine Learning of Algebraic Stress Models using Deterministic Symbolic Regression," *arXiv preprint arXiv:1905.07510*, 2019.

[6] Kennedy, M. C. and O'Hagan, A., "Bayesian calibration of computer models," *Journal of the Royal Statistical Society: Series B (Statistical Methodology)*, Vol. 63, No. 3, 2001, pp. 425–464.

[7] Cheung, S. H., Oliver, T. A., Prudencio, E. E., Prudhomme, S., and Moser, R. D., "Bayesian uncertainty analysis with applications to turbulence modeling," *Reliability Engineering & System Safety*, Vol. 96, No. 9, 2011, pp. 1137–1149.

[8] Edeling, W., Cinnella, P., Dwight, R. P., and Bijl, H., "Bayesian estimates of parameter variability in the k–ε turbulence model," *Journal of Computational Physics*, Vol. 258, 2014, pp. 73–94.

[9] Edeling, W., Cinnella, P., and Dwight, R. P., "Predictive RANS simulations via Bayesian model-scenario averaging," *Journal of Computational Physics*, Vol. 275, 2014, pp. 65–91.

[10] Kato, H., Yoshizawa, A., Ueno, G., and Obayashi, S., "A data assimilation methodology for reconstructing turbulent flows around aircraft," *Journal of Computational Physics*, Vol. 283, 2015, pp. 559–581.

[11] Li, Z., Zhang, H., Bailey, S. C., Hoagg, J. B., and Martin, A., "A data-driven adaptive Reynolds-averaged Navier–Stokes k–ω model for turbulent flow," *Journal of Computational Physics*, Vol. 345, 2017, pp. 111–131.

[12] Dow, E. and Wang, Q., "Uncertainty quantification of structural uncertainties in RANS simulations of complex flows," *20th AIAA Computational Fluid Dynamics Conference*, 2011, p. 3865.

[13] Dow, E. and Wang, Q., "Quantification of Structural Uncertainties in the k-w Turbulence Model," *52nd AIAA/ASME/ASCE/AHS/ASC Structures, Structural Dynamics and Materials Conference 19th AIAA/ASME/AHS Adaptive Structures Conference 13t*, 2011, p. 1762.

[14] Parish, E. J. and Duraisamy, K., "A paradigm for data-driven predictive modeling using field inversion and machine learning," *Journal of Computational Physics*, Vol. 305, 2016, pp. 758–774.

[15] Singh, A. P. and Duraisamy, K., "Using field inversion to quantify functional errors in turbulence closures," *Physics of Fluids*, Vol. 28, No. 4, 2016, pp. 045110.

[16] He, C., Liu, Y., and Gan, L., "A data assimilation model for turbulent flows using continuous adjoint formulation," *Physics of Fluids*, Vol. 30, No. 10, 2018, pp. 105108.

[17] Belligoli, Z., Dwight, R., and Eitelberg, G., "Assessment of a Data Assimilation Technique for Wind Tunnel Wall Interference Corrections," *AIAA Scitech 2019 Forum*, 2019, p. 0939.

[18] Singh, A. P., Duraisamy, K., and Zhang, Z. J., "Augmentation of turbulence models using field inversion and machine learning," *55th AIAA Aerospace Sciences Meeting*, 2017, p. 0993.

[19] Belligoli, Z., Dwight, R., and Eitelberg, G., "RANS Data Assimilation Techniques for Wind-Tunnel Wall Interference Corrections," *AIAA Aviation 2019 Forum*, 2019, p. 2976.

[20] Xiao, H., Wu, J.-L., Wang, J.-X., Sun, R., and Roy, C., "Quantifying and reducing model-form uncertainties in Reynolds-averaged Navier–Stokes simulations: A data-driven, physics-informed Bayesian approach," *Journal of Computational Physics*, Vol. 324, 2016, pp. 115–136.

[21] Wang, J.-X. and Xiao, H., "Data-driven CFD modeling of turbulent flows through complex structures," *International Journal of Heat and Fluid Flow*, Vol. 62, 2016, pp. 138–149.

[22] Foures, D. P., Dovetta, N., Sipp, D., and Schmid, P. J., "A data-assimilation method for Reynolds-averaged Navier–Stokes-driven mean flow reconstruction," *Journal of Fluid Mechanics*, Vol. 759, 2014, pp. 404–431.

[23] Symon, S., Dovetta, N., McKeon, B. J., Sipp, D., and Schmid, P. J., "Data assimilation of mean velocity from 2D PIV measurements of flow over an idealized airfoil," *Experiments in fluids*, Vol. 58, No. 5, 2017, pp. 61.

[24] Xiao, H., Wang, J.-X., and Ghanem, R. G., "A random matrix approach for quantifying model-form uncertainties in turbulence modeling," *Computer Methods in Applied Mechanics and Engineering*, Vol. 313, 2017, pp. 941–965.

[25] Menter, F. R., Kuntz, M., and Langtry, R., "Ten years of industrial experience with the SST turbulence model," *Turbulence, heat and mass transfer*, Vol. 4, No. 1, 2003, pp. 625–632.

[26] Giles, M. B. and Pierce, N. A., "An introduction to the adjoint approach to design," *Flow, turbulence and combustion*, Vol. 65, No. 3-4, 2000, pp. 393–415.

[27] Pironneau, O., "On optimum design in fluid mechanics," *Journal of Fluid Mechanics*, Vol. 64, No. 1, 1974, pp. 97–110.

[28] Dwight, R. P. and Brezillon, J., "Effect of approximations of the discrete adjoint on gradient-based optimization," *AIAA journal*, Vol. 44, No. 12, 2006, pp. 3022–3031.

[29] Peter, J. E. and Dwight, R. P., "Numerical sensitivity analysis for aerodynamic optimization: A survey of approaches," *Computers & Fluids*, Vol. 39, No. 3, 2010, pp. 373–391.

[30] Albring, T. A., Sagebaum, M., and Gauger, N. R., "Development of a consistent discrete adjoint solver in an evolving aerodynamic design framework," *16th AIAA/ISSMO Multidisciplinary Analysis and Optimization Conference*, 2015, p. 3240.

[31] Albring, T. A., Sagebaum, M., and Gauger, N. R., "Efficient aerodynamic design using the discrete adjoint method in su2," *17th AIAA/ISSMO multidisciplinary analysis and optimization conference*, 2016, p. 3518.

[32] Economon, T. D., Palacios, F., Copeland, S. R., Lukaczyk, T. W., and Alonso, J. J., "SU2: An open-source suite for multiphysics simulation and design," *Aiaa Journal*, Vol. 54, No. 3, 2016, pp. 828–846.

[33] Vitale, S., Gori, G., Pini, M., Guardone, A., Economon, T. D., Palacios, F., Alonso, J. J., and Colonna, P., "Extension of the su2 open source cfd code to the simulation of turbulent flows of fuids modelled with complex thermophysical laws," *22nd AIAA Computational Fluid Dynamics Conference*, 2015, p. 2760.

[34] Liu, D. C. and Nocedal, J., "On the limited memory BFGS method for large scale optimization," *Mathematical programming*, Vol. 45, No. 1-3, 1989, pp. 503–528.

[35] Emory, M., Larsson, J., and Iaccarino, G., "Modeling of structural uncertainties in Reynolds-averaged Navier-Stokes closures," *Physics of Fluids*, Vol. 25, No. 11, 2013, pp. 110822.

[36] Banerjee, S., Krahl, R., Durst, F., and Zenger, C., "Presentation of anisotropy properties of turbulence, invariants versus eigenvalue approaches," *Journal of Turbulence*, 2007, pp. N32.

[37] Mishra, A. A., Mukhopadhaya, J., Iaccarino, G., and Alonso, J., "Uncertainty Estimation Module for Turbulence Model Predictions in SU2," *AIAA Journal*, Vol. 57, No. 3, 2018, pp. 1066–1077.

[38] Edeling, W. N., Iaccarino, G., and Cinnella, P., "Data-free and data-driven RANS predictions with quantified uncertainty," *Flow, Turbulence and Combustion*, Vol. 100, No. 3, 2018, pp. 593–616.

[39] Soize, C., "Random matrix theory for modeling uncertainties in computational mechanics," *Computer methods in applied mechanics and engineering*, Vol. 194, No. 12-16, 2005, pp. 1333–1366.

[40] Singh, A. P., Medida, S., and Duraisamy, K., "Machine-learning-augmented predictive modeling of turbulent separated flows over airfoils," *AIAA Journal*, 2017, pp. 2215–2227.

[41] Rumsey, C. L., "Recent developments on the turbulence modeling resource website," *22nd AIAA Computational Fluid Dynamics Conference*, 2015, p. 2927.

[42] Somers, D. M., "Design and experimental results for the S809 airfoil," Tech. rep., National Renewable Energy Lab., Golden, CO (United States), 1997.

[43] Roy, C., "Review of discretization error estimators in scientific computing," *48th AIAA Aerospace Sciences Meeting Including the New Horizons Forum and Aerospace Exposition*, 2010, p. 126.

[44] Greenblatt, D., Paschal, K. B., Yao, C. S., Harris, J., Schaeffler, N. W., and Washburn, A. E., "Experimental investigation of separation control part 1: baseline and steady suction," *AIAA journal*, Vol. 44, No. 12, 2006, pp. 2820–2830.

[45] NASA, "Turbulence Modeling Resource," `https://turbmodels.larc.nasa.gov/`, 2019.

5

Non-Linear Wind-Tunnel Wall Interference Corrections

Abstract   *In Chapter 3, a wind-tunnel experiment was done to validate the results of a numerical optimization. In general, wind-tunnel testing is a fundamental component of the development cycle of new aerodynamic designs. However, at high Mach number and/or angle of attack, the presence of the walls makes the in-tunnel flow differ significantly from what it would be in free-air. Finding the free-air conditions corresponding to the in-tunnel ones is the aim of wall-interference corrections. In Chapter 4, the ability of variational data assimilation to use experimental data to correct turbulence modeling errors was demonstrated. The present Chapter extends and applies the same concept to the problem of wind-tunnel wall interferences. After briefly introducing the problem of non-linear wind-tunnel wall interference corrections, one of the data assimilation techniques of Chapter 4 is reformulated to correct the free-stream Mach number and angle of attack. The technique is then tested on 2D and 3D cases, and its advantages and areas of possible improvements are finally discussed at the end of the Chapter.*

5.1   Introduction

The design of an air vehicle depends on techniques to assess performance in free air. These can either be experimental fluid dynamics (EFD) or computational fluid dynamics (CFD) techniques. Typically, EFD involves an experiment in a wind tunnel and has been the dominant tool for testing aeronautic designs for the majority of the twentieth century. However, due to the increase in computational speed and accuracy, there has been a steady decline in the wind tunnel testing time relative to the CFD testing time [1]. Currently, CFD and EFD coexist, with the latter being used to test the design in the most challenging regions of the flight envelope, where uncertainties due to approximations in the CFD models become substantial.

However, wind-tunnel experiments themselves have uncertainties. One of the most critical is due to the presence of the wind-tunnel walls, which alter the flow field around the test object, making it different from what it would be in free-air. The existence of a free-air flow giving the same forces and moments as those measured in the tunnel is the fundamental assumption of the entire practice of wind-tunnel corrections [2]. If the flow is subsonic, the angle of attack is small, and the cross-section of the test object relative to the wind-tunnel is small, then corrections can be based on linearized, inviscid potential flow theory, hence the name *linear corrections*. When one of these conditions is not satisfied, significant errors result. Despite these considerations, the majority of wind-tunnel operators still makes use of linear corrections in the non-linear regime, or do not correct the data at all when non-linear effects become too strong [3].

Several techniques have been proposed for non-linear wind-tunnel wall interference corrections. One of the most popular consists in taking the difference between a turbulent CFD simulation of the test object in the wind tunnel and in free flight [4–7], and using this information to adjust the experimental Mach number, angle of attack and, in some cases, force coefficients. The main challenges of this approach are the need to model the geometry of the wind tunnel accurately, the boundary conditions at ventilated walls [2, 8], and the effect of turbulence. The first problem can be solved by using a detailed CAD file

of the wind-tunnel geometry, although meshing such a domain is a time-consuming, little-automated activity which results in an extremely large number of cells, thus significantly increasing the computational cost of the simulation. For the second problem, there exist many different formulations of the porous/ventilated wall boundary condition for which, however, characterization of the cross-flow at the wall remains problematic [9, 10]. Finally, even if the first two problems were solved, modeling turbulent flow in the non-linear regime remains one of the most challenging tasks for the CFD community, as current turbulence models prove to be inaccurate in those conditions [11, 12]. All these factors affect the quality of the wall-interference correction because, in essence, wall-interference correction techniques are strictly dependent on the computational methods used to obtain them.

This study proposes a variational data assimilation (DA) approach combining experimental and numerical results in a systematic way, to simultaneously correct for wind-tunnel wall interference and errors in the RANS turbulence model, without needing to model the wind-tunnel geometry or the boundary conditions at the ventilated walls. The method minimizes the discrepancy between high-fidelity experimental observations and the numerical prediction of those same quantities by modifying the free-stream Mach number, angle of attack, and a local corrective term for the turbulence model. In this way, experimental data are used to correct the CFD simulations and, in turn, the CFD simulations are used to correct the Mach number and angle of attack of the experiments, thus returning the free-air conditions corresponding to the in-tunnel flow field. The numerical optimization is carried out directly in free-air, thus simplifying the meshing process and reducing the total number of mesh points thanks to the absence of the wind-tunnel walls.

To our knowledge, only a few studies have addressed the problem of wind-tunnel interference corrections using data assimilation. The idea of injecting experimental data into computer simulations for correcting wall interference was first introduced by Murman [13], who proposed to minimize the difference between the experimental and numerical pressures on a supercritical airfoil by using the free-stream Mach number and angle of attack as control parameters. This approach was tested with success on synthetic data but did not take into account the influence of viscosity in a comprehensive manner. Only recently, Ma et al. [14] extended it to a viscous code using a variational data assimilation procedure on 2D airfoils in the transonic regime. Their results showed that the methodology was able, not only to obtain pressure contours that closely match the experimental ones, but also accurate estimations of the lift and pitching moment coefficients. However, they did not take into account the errors associated with the choice of turbulence model, which could yield misleading results for the corrected angle of attack and Mach number, especially in strongly non-linear conditions. This problem was acknowledged by Kato et al. [15], who proposed a DA framework, based on the ensemble Kalman filter, with the capability to estimate not only the angle of attack and Mach number but also other parameters influencing the turbulence model, such as the von Karman constant. By doing this, they were able to address the uncertainty associated with the values of (one of) the closure coefficients of the turbulence model, thus providing insights into the variability of the model outputs. Nevertheless, this technique is limited in scope since the functional form of the turbulence model is frozen, thus preventing corrections to the balance

of terms within it, which is an important factor for the accurate prediction of turbulent flows [16]. Having acknowledged this, Duraisamy and co-workers [16–19] recently developed a variational data assimilation framework for the correction of RANS turbulence modeling errors using a corrective scalar field as a multiplicative factor to the production term in the turbulence model (see Section 4.2.2).

In its essence, the methodology proposed in this work combines the ideas of Murman [13] and Ma et al. [14] with the seminal work of Duraisamy and co-workers [16–19], to build a variational data assimilation technique capable of correcting the experimental angle of attack and Mach number, as well as the functional errors in the turbulence model.

Here, we formally derive the expression of the objective function from a probabilistic point of view (Section 5.2), we apply the methodology to both 2D and 3D cases and compare it to linear correction methods (Section 5.3). Furthermore, we discuss the capabilities of the DA framework to correctly infer unobserved quantities, such as the velocity field around the test object. Finally, we summarize the main conclusions and propose further developments in Section 5.4.

5.2   Methodology

This section lays the foundations of the data assimilation methodology for correcting non-linear wind-tunnel wall interference. Strong non-linear flow effects can only be described by a non-linear model. Because non-linearities are often associated with transonic conditions, we choose the compressible Reynolds-averaged Navier-Stokes (RANS) equations as our non-linear model. If a sufficiently refined CAD model and mesh are used, as well as adequate thresholds for the convergence of iterative numerical methods, the largest source of error in a RANS code is due to the turbulence model. In principle, if this error were removed, the RANS equations would be able to exactly predict the mean flow, and wind-tunnel experiments would become almost redundant.

In practice, the present work uses experimental data to correct turbulence-modeling errors, thus connecting CFD and EFD to obtain accurate and additional information about the flow configuration under study. To do so, we propose a variational data assimilation framework that uses a gradient-based algorithm to optimize the values of the free-stream angle of attack, Mach number, and a corrective term of the turbulence model by minimizing the difference between sparse experimental observations and their numerical prediction with a RANS code.

This is an ill-posed inverse problem, for which the solution is non-unique. Hence, while it is theoretically possible to reconstruct the true flow field, in practice this seldom happens, and the numerical flow field is somewhat different from the true one. The optimization problem is

$$\min_{\boldsymbol{\theta}} \quad \mathcal{J}$$
$$\text{s.t.} \quad \mathcal{R}(\boldsymbol{U}, \boldsymbol{\theta}) = 0 \tag{5.1}$$

where $\mathcal{J} = \|\boldsymbol{d}_{\text{CFD}}(\boldsymbol{\theta}) - \boldsymbol{d}_{\text{EXP}}\|_p + \|\boldsymbol{\theta}\|_p$, $\|\cdot\|_p$ is the L_p-norm, $\boldsymbol{d}_{\text{EXP}}$, $\boldsymbol{d}_{\text{CFD}}$ are the experimental

and numerical observations, respectively, $\boldsymbol{\theta}$ is the high-dimensional vector of control parameters, and $\mathcal{R}$ is the operator representing the RANS equations, the turbulence model, and their boundary conditions. The first term in $\mathcal{J}$ is the difference between experimental and numerical quantities in a certain norm, while the second is a regularization term that selects one particular solution form the large space of possible ones.

The Bayesian formulation of the problems essentially follows that of Section 4.2.1, with the only difference that the vector of control parameters is augmented with the free-stream Mach number and angle of attack. All the three data assimilation techniques presented in Chapter 4 could be used for the problem of wall-interference corrections but here we only consider the TPP method of Section 4.2.2 for explicative purposes. Hence, the objective function is

$$\mathcal{J} = \sum_{i=1}^{N_d} \frac{[\mathcal{B}(\boldsymbol{\theta})_i - d_i]^2}{2\sigma_{\text{exp}}^2} + \sum_{j=1}^{N_m} \frac{\left(\beta_j - 1.0\right)^2}{2\sigma_{\beta}^2} + \frac{\left(M_\infty - M_{\infty,\text{prior}}\right)^2}{2\sigma_M^2} + \frac{\left(\alpha_\infty - \alpha_{\infty,\text{prior}}\right)^2}{2\sigma_\alpha^2}, \quad (5.2)$$

with $\boldsymbol{\theta} = [\alpha_\infty, M_\infty, \boldsymbol{\beta}]^\top$ being a high-dimensional vector with $N_m + 2$ parameters, where $\boldsymbol{\beta}$ corrects functional errors in the RANS turbulence model, while the optimum α_∞ and M_∞ are the interference-free angle of attack and Mach number.

As explained in Section 2.5, gradient-based algorithms are suited for this type of high-dimensional optimization, and this work makes use of the low-memory Broyden-Fletcher-Goldfarb-Shanno (L-BFGS) [28] optimization algorithm to update the value of the control parameters and compute the step size of the optimization. The initial angle of attack and Mach number can be specified to be the in-tunnel ones, while the initial corrective term can be specified in such a way that the result of the first optimization iteration is that of a RANS simulation with an uncorrected turbulence model. Finally, the optimization terminates when either

- $\max(|\partial_i \mathcal{J}|) \leq 5 \cdot 10^{-5}$ for $i = 1, ..., N_m + 2$, or

- $\frac{\mathcal{J}^q - \mathcal{J}^{q+1}}{\max\{|\mathcal{J}^q|, |\mathcal{J}^{q+1}|, 1\}} \leq 10^{-3}$,

where q is the q-th optimization iteration, $\partial_i \mathcal{J}$ is the gradient of the objective function with respect to the i-th control parameter, and the values of the thresholds are specified by the user.

The optimum solution gives the best agreement between the experimental and numerical quantities. It directly provides the corrected values of the free-stream angle of attack and Mach number while also minimizing the error due to the approximation of the Reynolds stress tensor by the turbulence model. It is worth noting that this method can work with any kind of experimental data, e.g. $\boldsymbol{d}_{\text{EXP}}$ may be a 3D velocity field from particle image velocimetry (PIV), or pressure on a surface, or a combination of both.

The drawback of this methodology is that the optimization procedure is computationally time-consuming, especially in three dimensions or in the presence of complicated flow cases and therefore can only be performed off-line at the end of the experimental campaign. This may not be ideal when the correctability of the data has to be assessed

during an experiment. In that case, simpler but faster techniques should be used. Besides, non-uniqueness of the solution and convergence to local minima tend to make the final corrections sub-optimal. Although these problems influence the accuracy of the corrections and of the reconstructed flow field, in practice their effect is limited, provided the objective function is regularized and the initial value of the vector of control parameters lies in a neighborhood of the true optimum.

5.3   Results

In this section, the data assimilation methodology is used to obtain the wind-tunnel wall interference corrections for 2D and 3D experiments with non-linear effects. The selected test cases are the high Mach number, low angle of attack experiment on the RAE 2822 airfoil conducted by Cook et al. in 1979 [36], the low Mach number, high angle of attack experiment on the S809 airfoil by Somers [37], and the high Mach number, low angle of attack experiment on the ONERA M6 wing [38]. While the framework presented in this work can be used with different types of experimental data (e.g. velocity, pressure, skin friction), we choose to use only surface pressure data since these are one of the most common types of data obtainable from experiments. For the purpose of this work, the data of Cook et al. [36] and Somers [37] are considered to be perfectly 2D and thus free of sidewall interference. However, it should be acknowledged that sidewall effects may be present due to the relatively small aspect ratio ($AR < 4$) of the wings used for the experiments.

The initial Mach number and angle of attack for each optimization are set to the values obtained from a conventional correction procedure. Furthermore, the results of the data assimilation methodology using $\boldsymbol{\theta}_\beta = [\alpha_\infty, M_\infty, \boldsymbol{\beta}]^\top$ as vector of control parameters will be compared with those of a data assimilation using $\boldsymbol{\theta} = [\alpha_\infty, M_\infty]^\top$, in order to show how correcting functional errors in the turbulence model affects the final wall interference corrections.

5.3.1   RAE 2822 - Case 10

Among all the configurations tested by Cook et al. [36], the one at $M_\infty = 0.75$ and $\alpha_\infty = 3.06$ degrees (case 10) presents shock-induced boundary layer separation, which makes it hard to find adequate wall interference corrections using linear techniques and has proven challenging to simulate with CFD. A correction to these values was proposed by Rudnik [39], who kept the same Mach number while lowering the angle of attack to 2.80 degrees. Rudnik's correction is adopted as the initial condition for α_∞ and M_∞ of the data assimilation methodology. A value of $\sigma_{\exp} = 2.6 \times 10^{-3}$ is selected in accordance with the data in [36]. A standard deviation of unity is assigned to all the other parameters.

A hybrid O-mesh geometry is used, with the far-field boundary placed 100 chord lengths away from the airfoil to avoid reflections of characteristic waves back into the domain. A no-slip adiabatic boundary condition is imposed on the airfoil, while

(a) The complete computational domain.

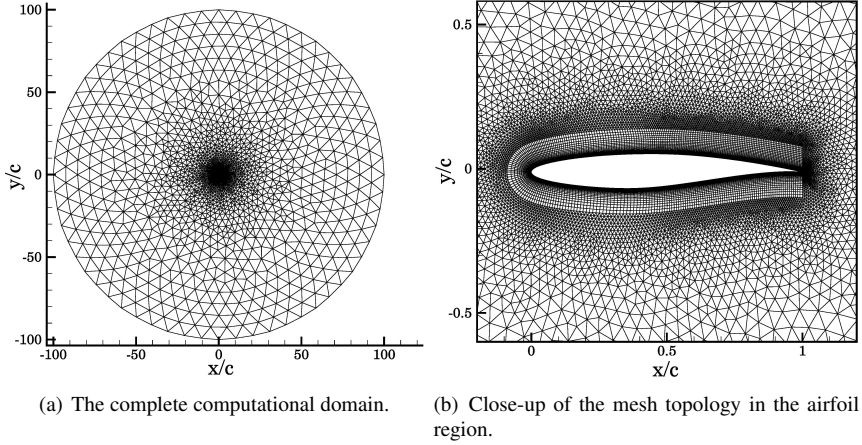(b) Close-up of the mesh topology in the airfoil region.

Figure 5.1: Details of the hybrid computational mesh for the RAE 2822 airfoil.

characteristic-based boundary conditions are specified at the far-field. A layer of structured cells is wrapped around the airfoil, while the rest of the domain is filled with triangular cells. The maximum cell height in the boundary layer mesh is selected such that $y^+ \approx 1$. The mesh, which has 24,086 points and with 287 edges on the airfoil surface, can be seen in Figure 5.1.

The convective fluxes are discretized with a second-order Jameson-Schmidt-Turkel (JST) scheme [40], and the gradients for the viscous fluxes are computed using a weighted least squares method. Implicit local time stepping is used to converge the simulation to a steady-state solution, and the linear system is solved using the iterative GMRES method with a tolerance of $O(10^{-6})$ on the maximum error.

Figure 5.2 shows the optimization history for the case with $\boldsymbol{\theta}_\beta$, and $\boldsymbol{\theta}$ (which corresponds to the technique proposed by Ma et al. [14]). Both techniques are capable of reducing the difference between the numerical and experimental pressure coefficient on the airfoil compared to the initial state. Both optimization histories show the same behavior for the first 20 iterations, indicating that the bulk of the improvements is due to changes to the angle of attack and Mach number. However, when $\boldsymbol{\beta}$ is included in the vector of control parameters, an additional reduction of $\hat{\mathcal{J}} = \sum_{i=1}^{N_d} \frac{[\mathcal{B}(\boldsymbol{\theta})_i - d_i]^2}{2\sigma_{\exp}^2}$ is observed thanks to corrections of inadequacies in the turbulence model. This comes at the cost of a higher number of optimization iterations. Indeed, since $\boldsymbol{\theta}_\beta$ is a high-dimensional vector with more than twenty thousand control parameters, the optimization algorithm searches in a comparatively high-dimensional space, hence the larger number of optimization iterations compared to the case with $\boldsymbol{\theta}$, which is only a bi-dimensional vector.

Figure 5.3 shows the initial c_p distribution for the baseline case (obtained with angle of attack and Mach number proposed by Rudink [39]), the final c_p distributions from the optimizations with $\boldsymbol{\theta}$, and $\boldsymbol{\theta}_\beta$, and the experimental data. The optimized results better
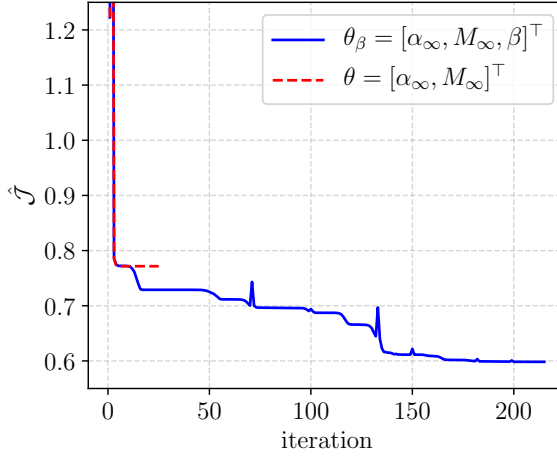
93

Figure 5.2: Optimization histories for the RAE 2822 test case.

Table 5.1: Comparison of results from proposed methodology with different wind-tunnel wall interference correction techniques used as benchmark for the RAE 2822 case.

	$\hat{\mathcal{J}}$	α_∞ [deg]	M_∞	c_l	c_m
Experimental data	-	3.19	0.750	0.743	−0.1060
Baseline	1.223	2.80	0.750	0.747	−0.1007
$\boldsymbol{\theta}$	0.7716	3.00	0.759	0.720	−0.0997
$\boldsymbol{\theta}_\beta$	0.5983	2.90	0.758	0.736	−0.1069

capture the shock location but slightly underestimate the magnitude of the pressure peak at the leading edge. In addition, the optimization with $\boldsymbol{\theta}_\beta$ accurately reproduces the pressure distribution after the shock, while the optimization with $\boldsymbol{\theta}$ still shows some disagreement due to its inability to correct the errors due to the turbulence model.

Table 5.1 summarizes some of the results for this test case. We observe that the c_l and c_m predicted by the data assimilation technique proposed in this work are very close to those measured in the experiment. This is not surprising since the lift and the pitching moment coefficients are closely related to the pressure distribution over the airfoil. The optimization with $\boldsymbol{\theta}_\beta$ as vector of control parameters reduces the value of the initial $\hat{\mathcal{J}}$ by more than 50%, that with $\boldsymbol{\theta}$ only by 30%. The optimum angle of attack and Mach number from both data assimilation techniques are higher than the baseline case. However, they substantially differ from each other, especially in the proposed angle of attack correction, thus showing that including $\boldsymbol{\beta}$ in the vector of control parameters has a profound effect on the wall-interference corrections.

Finally, by looking at the boundary layer comparison of Fig. 5.4, one can observe
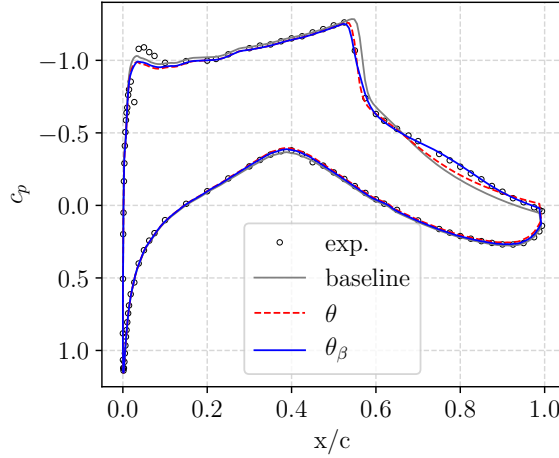
Figure 5.3: Comparison of the c_p distribution from the optimizations, the experiment, and the baseline simulation (obtained by running a turbulent CFD simulation with M_∞ and α_∞ from [39]).

that it is easy for the CFD solver to reproduce the boundary layer shape before the shock location, but much harder to do so consistently downstream of it. Indeed, the boundary layer shape from the optimizations agrees well with the experimental one at $x/c = 0.75$ but not at $x/c = 0.9$, and vice-versa for the baseline results. This is an indication that there might not be an equivalent free-air condition to the in-tunnel one, and thus the results are uncorrectable, possibly due to the presence of sidewall effects. It is also likely that the experimental pressure coefficient is not sufficiently informative to precisely reconstruct unobserved quantities (like the velocity field) all over the computational domain. Alternatively, it could be that the flow physics behind the shock and close to the wall cannot be reproduced entirely by eddy viscosity models, even when corrected with the methodology proposed in this work. In order to increase the quality of the reconstruction of the velocity field, one could also incorporate the experimental data for the boundary layers in the objective function and, in general, all available experimental data. This would constrain the optimizer to agree as best as it can with all the different sources of experimental data used in the objective function, thus making it less likely to observe large deviations like the one in Fig. 5.4(d).

5.3.2 S809 Airfoil

The S809 airfoil is commonly used for the design of the blades of horizontal axis wind turbines. Experimental data at $Re_c = 2 \times 10^6$, $M_\infty = 0.2$, and at a variety of angles of attack are available from the study of Somers [37]. In our case, we perform the inversion
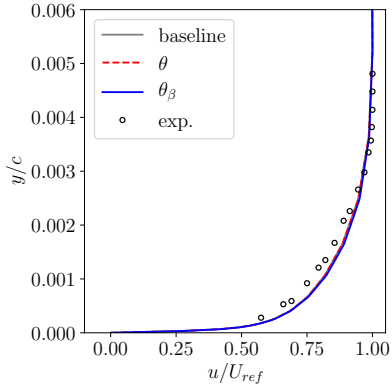
(a) $x/c = 0.179$.
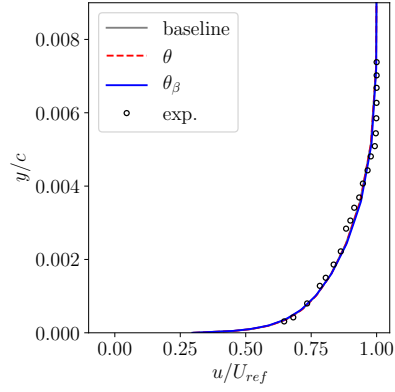
(b) $x/c = 0.319$.
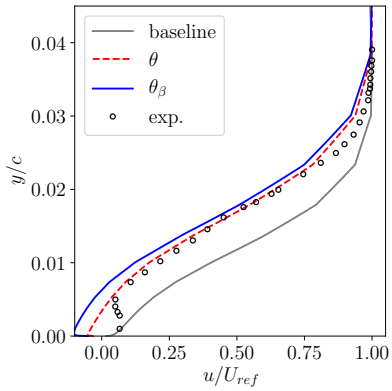
(c) $x/c = 0.750$.
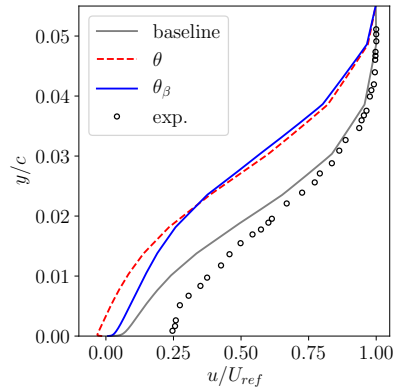
(d) $x/c = 0.900$.

Figure 5.4: Comparison of boundary layers at different x/c locations on the upper surface of the RAE 2822 airfoil.
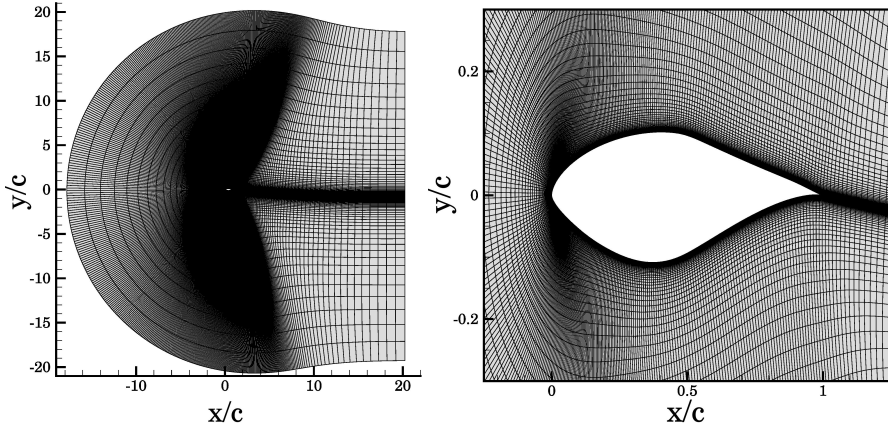
(a) The complete computational domain for the (b) Close-up of the mesh topology in the airfoil region.
s809 test case.

Figure 5.5: Details of the structured computational mesh.

at the highest angle of attack of the database, i.e. $\alpha_\infty = 14.24°$, for which a large region of turbulent separation due to an adverse pressure gradient is present. Note that this value for the angle of attack was obtained using a linear correction technique and is used as initial α_∞ for the optimization. Figure 5.5 shows the computational mesh used for this test case, which is the same structured C-grid with approximately 5.5×10^4 points and a $y^+ \approx 1$ and with the same boundary conditions as in Section 4.3.1. The pressure coefficient from the experiment of Somers [37] is chosen as training data for the objective function and $\sigma_{exp} = 0.02$. Because extracting the data is prone to errors in proximity of regions with high gradients, only the suction-side pressure data in the range $0.05 < x/c < 0.8$ were used. The same spatial and time discretizations, linear solver, and optimization algorithm as in Section 5.3.1 were used. Since compressibility effects are limited, the Mach number is excluded from the control parameters used for the correction procedures such that $\boldsymbol{\theta} = \alpha_\infty$, and $\boldsymbol{\theta}_\beta = [\alpha_\infty, \boldsymbol{\beta}]^\top$.

The optimization history of Fig. 5.6 shows that only correcting the angle of attack has a minimal impact on the error between experiments and simulations. The proposed correction to the angle of attack may very well be right, but there is no way to assess this since the value of $\hat{\mathcal{J}}$ – which indicates the accuracy of the corrections – remains high because errors due to the turbulence model are affecting the simulation results. Hence, the importance of having the corrective term $\boldsymbol{\beta}$ among the control parameters. It is evident that the high $\hat{\mathcal{J}}$ is due to turbulence modeling error; by correcting this error, an estimate of the accuracy of the corrections can thus be obtained.

Figure 5.7 shows the baseline and assimilated pressure and skin-friction coefficients over the airfoil. The SST model overpredicts the pressure on the suction side and predicts the location of the separation point more downstream than in the experiments. As already
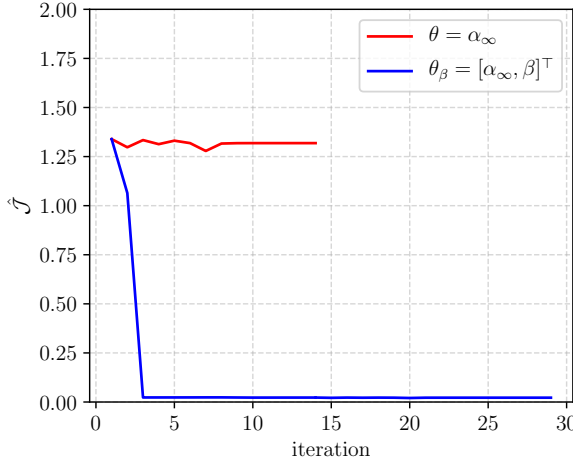
Figure 5.6: Optimization histories for the s809 test case.

observed, correcting only the angle of attack does not change the pressure distribution, while correcting the functional errors in the turbulence model produces an almost-perfect match with the experimental data.

The turbulent viscosity μ_{turb} for the baseline and corrected results is shown in Fig. 5.8. A significant increase of its value in the wake region is produced by the correction procedure proposed in this paper, as shown in Fig. 5.8(c), which indicates the presence of a stronger turbulent flow enhancing the mixing in that region. These considerations can be useful during the development phase of an aerodynamic design since they complement the sparse information of the experimental results with full-field data corresponding to the numerical simulation that best match the experiments.

Table 5.2 summarizes the results for this test case. The methodology proposed in this work is compared with the results from the baseline case, i.e. the initial condition of the optimization with the in-tunnel angle of attack and Mach number and β equal to unity, and a benchmark case which only optimizes the angle of attack. Although the corrections to the angle of attack are small, the agreement with the experimental lift coefficient is significantly improved by the methodology proposed in this work, while that with the pitching-moment coefficient is slightly degraded. Hence, we can conclude that, for this test case, no significant wall interference was present, and a linear correction procedure is appropriate. However, the data assimilation methodology not only finds the corrected angle of attack but also corrects the numerical model so that its full-field results can be used to analyze the flow dynamics of the test object reliably. Furthermore, the value of $\hat{\mathcal{J}}$ can be used to estimate the reliability of the proposed corrections based on the agreement between experimental and numerical data.

(a) Pressure coeffiecient.
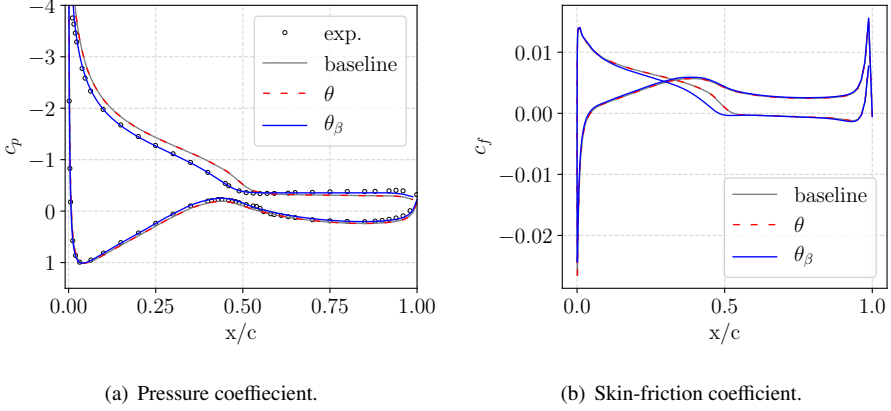
(b) Skin-friction coefficient.

Figure 5.7: Comparison of the c_p and c_f distributions from the optimizations, the experimental data, and the baseline simulation for the s809 test case.
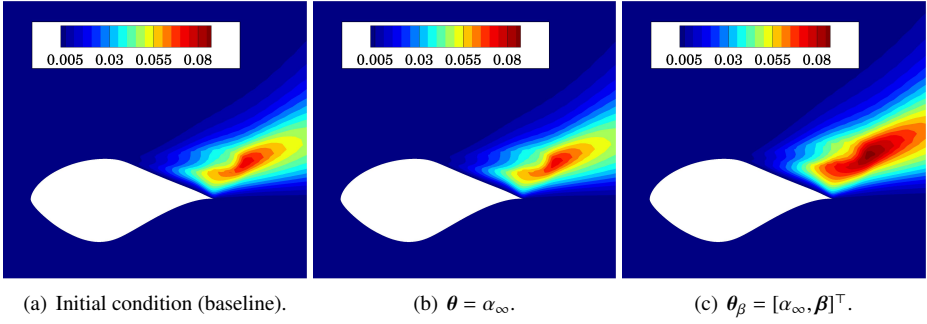

(a) Initial condition (baseline).

(b) $\theta = \alpha_\infty$.

(c) $\theta_\beta = [\alpha_\infty, \beta]^\top$.

Figure 5.8: Comparison turbulent viscosity μ_{turb} for the s809 test case.

Table 5.2: Comparison of results from proposed methodology with different baseline and benchmark results for the s809 case.

	$\hat{\mathcal{J}}$	α_∞ [deg]	M_∞	c_l	c_m
Experimental data	-	14.24	0.2	1.083	−0.0451
Baseline	1.339	14.24	0.2	1.240	−0.0450
θ	1.331	14.21	0.2	1.239	−0.0450
θ_β	0.022	14.23	0.2	1.105	−0.0440

5.3.3 Onera M6 Wing

The ONERA M6 wing is a widely used test case for the validation of numerical models thanks to the availability of experimental data for a variety of flow conditions [38]. In this work, the Reynolds number based on the mean aerodynamic chord is 11.72×10^6, $M_\infty = 0.8395$, and $\alpha_\infty = 3.06$ degrees. For these flow conditions, the leading-edge acceleration leads to supersonic flow, which is terminated by a shock wave. From there, the flow is re-accelerated to supersonic conditions again until a second shock is formed. This creates a lambda-shaped low-pressure area between the two shocks, as shown in Fig. 5.11(a). A structured semi-spherical mesh is used for the simulations, with the flat side being the plane of symmetry of the domain and the wing. Characteristic boundary conditions are specified at the far-field, and the no-slip condition are used for the wing surface. In total, the mesh had 6.6×10^5 points and a y^+ of approximately unity. Experimental pressure coefficients at spanwise locations $y/b = 0.2, 0.44, 0.65, 0.8, 0.9, 0.95, 0.99$ are selected as the observed quantities for $\hat{\mathcal{J}}$, and $\sigma_{\text{exp}} = 0.02$ is used. The same spatial and time discretization, linear solver, and optimization algorithm as in Section 5.3.1 are used. It is worth noting that the half-wing model was attached to a rotating plate in the experiment, while a symmetry boundary condition is employed at $y = 0$ in the numerical domain, and this may alter the flow physics at the wing root. Nonetheless, we attribute these differences to wall-interference effects and focus our analysis on the feasibility of using the proposed methodology for correcting wind-tunnel wall interference, rather than exactly reproducing the flow physics.

The optimization history of Fig.5.9 shows that the results of the proposed methodology have a better agreement between the experimental and numerical data than the baseline and benchmark cases. Compared to the 2D cases, $\hat{\mathcal{J}}$ is orders of magnitude larger since there are many more experimental data points contributing to its value. As a consequence, judging the accuracy of the corrections based on the value of $\hat{\mathcal{J}}$ is dependent on the number of experimental observations. To overcome this limitation, one can simply look at the mean squared error $\hat{\mathcal{J}}/N_m$.

The methodology proposed in this work improves the agreement with the experimental pressure distributions compared to the baseline and benchmark cases, especially at $y/b = 0.2$, where it correctly predicts the location of the second shock. However, there are still differences at $y/b = 0.65$ and at $y/b = 0.8$, where the strength of the first shock is not fully captured. This could be due to discretization errors, but the study of Mayeur et al. [42] shows that this phenomenon is present even for meshes of 10 million points. This suggests that the underestimation of the shock strength is purely due to turbulence model inadequacies. While our correction procedure can change the balance of terms in the functional form of the model, it is still forced to operate within the boundaries imposed by the Boussinesq hypothesis. Hence, more general corrective models like the one presented in Sections 4.2.3 and 4.2.4 should be examined for solving these issues.

By looking at the turbulent viscosity fields of Fig. 5.11, we observe no significant differences between the initial solution and the optimum solution found by the optimization with $\boldsymbol{\theta}$ as vector of control parameters. On the other hand, when $\boldsymbol{\theta}_\beta$ is used, a significant change to the μ_{turb} field close to the wing root is observed. This looks unphysical, and it
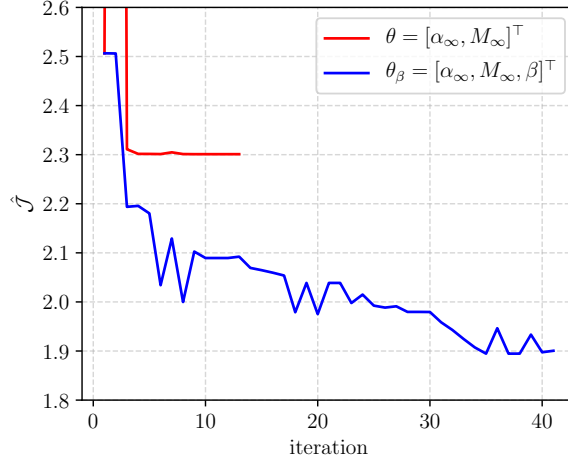
Figure 5.9: Optimization histories for the ONERA M6 test case.

(a) Section 1 - $y/b = 0.2$.

(b) Section 2 - $y/b = 0.44$.

(c) Section 3 - $y/b = 0.65$.

(d) Section 4 - $y/b = 0.8$.

(e) Section 5 - $y/b = 0.9$.

(f) Section 6 - $y/b = 0.95$.
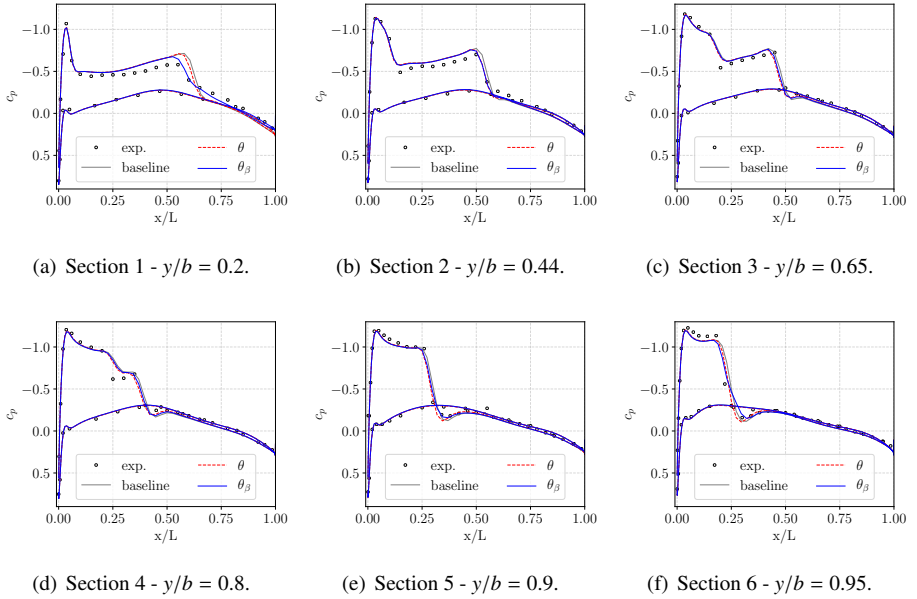
Figure 5.10: Comparison of c_p distributions at six of the seven locations where experimental data are available.

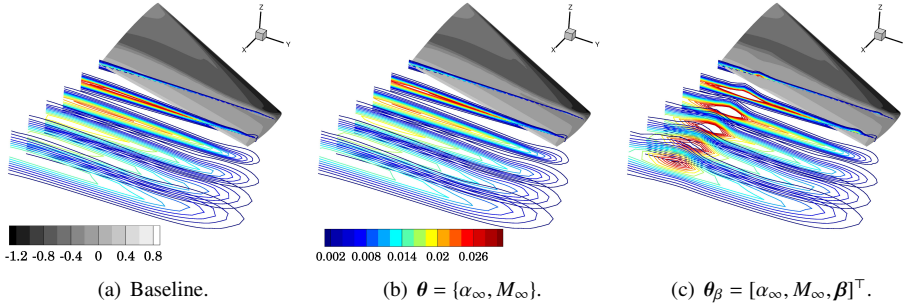(a) Baseline.　　　　　　　(b) $\theta = \{\alpha_\infty, M_\infty\}$.　　　　　(c) $\theta_\beta = [\alpha_\infty, M_\infty, \beta]^\top$.

Figure 5.11: Comparison of c_p contours (grayscale) on the wing and μ_{turb} iso-surfaces (colorscale) in the wake for the ONERA M6 test case.

Table 5.3: Comparison of results from proposed methodology with different baseline and benchmark results for the ONERA M6 case.

	$\hat{\mathcal{J}}$	α_∞ [deg]	M_∞
Experimental data	-	3.060	0.8395
Baseline	2.507	3.060	0.8395
θ	2.301	3.026	0.8367
θ_β	1.888	3.055	0.8389

is probably due to different boundary conditions between the experiment and the simulations. Indeed, the simulations employ a symmetry boundary condition at $y = 0$, while a wall was present at the same location in the experiment. This is an indication of the failure of half-model testing to reproduce the properties of a symmetry plane.

To complete the analysis, we report the values of $\hat{\mathcal{J}}$, α_∞, and M_∞ in Table 5.3, where we can see how only small changes to the angle of attack and Mach number are obtained after using the framework proposed in this work. Nonetheless, together with the corrections to the functional errors in the turbulence model operated by β, they contribute to reducing the least-square error $\hat{\mathcal{J}}$ between experimental data and corresponding numerical data by about 25%.

5.4　Conclusions

The wall-interference correction methodology presented in this work was developed for the non-linear flow regime. For this, we make use of the compressible RANS equations and a turbulence model for capturing viscous phenomena. A gradient-based optimization problem must be solved to obtain the optimum corrections. The progress in computer hardware and numerical algorithms made it possible to carry out this process within a few days at the most (depending on the available computational resources, number of mesh

points, and size of the vector of control parameters). However, wind-tunnel operators usually prefer to have on-line corrections to analyze immediately whether the interference is small. In this view, the non-linear correction technique of this work can be used as an off-line tool to obtain more accurate wall-interference corrections and to augment the experimental data with full-field information of the case at hand.

The optimum solution found by the optimization gives the best possible agreement with the experimental data used in the objective function $\mathcal{J}$, given the initial conditions, and the mathematical model used. However, the solution to this ill-posed inverse problem is non-unique. The regularization term in the objective function makes sure that the optimum solution lies in a neighborhood of the initial state by penalizing substantial departures of the control variables from their initial values.

One of the fundamental assumptions of the data assimilation methodology is that the experimental data are the ground truth and that there exists a free-air condition that gives the same in-tunnel results. Traditionally, this assumption was not always used, and linear techniques corrected not only the flow conditions but also the force coefficients. In our methodology, this choice is left to the user: based on her knowledge, she can either use the experimental data as ground truth and use the value of the mean squared error $\hat{\mathcal{J}}/N_m$ to estimate the accuracy of the corrections, or decide to accept the numerically obtained pressure distribution in place of the experimental one.

For simplicity, we have only used experimental pressure coefficients on the wing surface for the test cases of Section 4.3. However, any type of physical quantity obtainable from an experiment can be inserted in the objective function, and multiple physical quantities can co-exist (e.g. velocity and pressure). Hence, one can make use of all the experimental data at disposal for finding the optimum value of the corrections.

Finally, it is worth reminding that this technique does not require to represent and model the wind-tunnel walls since the optimization is directly carried out in free-air. This removes a considerable burden from the correction procedure, namely that of finding an accurate model for the ventilated boundary condition and that of meshing the entire geometry of the wind-tunnel walls to represent the flow through the ventilated surfaces accurately.

On the other hand, the process is more time-consuming than linear correction techniques and can only be carried out off-line. Additionally, the proposed correction to the turbulence model is limited in scope as it must comply with the Boussinesq hypothesis, and it can only address errors within its functional form. Hence, future work should focus on testing more general corrections to the errors introduced by the modeling of turbulence and on the combination of different types of experimental data (e.g. velocity and pressure) into the same objective function.

References

[1] Melanson, M., Chang, M., and Baker II, W., "Wind tunnel testing's future: A vision of the next generation of wind tunnel test requirements and facilities," *48th AIAA Aerospace Sciences Meeting Including the New Horizons Forum and Aerospace Exposition*, 2010, p. 142.

[2] Ewald, B., "Wind Tunnel Wall Correction," Tech. rep., ADVISORY GROUP FOR AEROSPACE RESEARCH AND DEVELOPMENT NEUILLY-SUR-SEINE (FRANCE), 1998.

[3] Davis, T. W., "Review of transonic wall interference corrections and considerations for development," *AIAA Aviation 2019 Forum*, 2019, p. 3094.

[4] Rueger, M. and Crites, R., "Wind tunnel boundary interference prediction and correction," *30th Aerospace Sciences Meeting and Exhibit*, 1992, p. 36.

[5] Martin, JR, F., Sickles, W., and Stanley, S., "Transonic wind tunnel wall interference analysis for the space shuttle launch vehicle," *31st Aerospace Sciences Meeting*, 1993, p. 420.

[6] Hantrais-Gervois, J.-L., Piat, J.-F., and Hantrais, J.-L., "A Methodology to Derive Wind Tunnel Wall Corrections from RANS Simulations," *Integration*, 2012.

[7] Nambu, T., Hashimoto, A., Aoyama, T., and Sato, T., "Numerical Analysis of the ONERA-M6 Wing with Wind Tunnel Wall Interference," *Transactions of the Japan Society for Aeronautical and Space Sciences*, Vol. 58, No. 1, 2015, pp. 7–14.

[8] Nambu, T., Hashimoto, A., Ueno, M., Murakami, K., and Sato, T., "Evaluation of wall-interference correction method using numerical analysis and porous wall model," *Journal of Aircraft*, Vol. 52, No. 1, 2015, pp. 226–234.

[9] Hashimoto, A., Aoyama, T., Kohzai, M., and Yamamoto, K., "Transonic wind tunnel simulation with porous wall and support devices," *27th AIAA Aerodynamic Measurement Technology and Ground Testing Conference*, 2010, p. 4201.

[10] Krynytzky, A., Fleming, M., Sommerfield, D., and Li, P., "Computational modeling of a slotted wall test section," *28th Aerodynamic Measurement Technology, Ground Testing, and Flight Testing Conference including the Aerospace T&E Days Forum*, 2012, p. 2863.

[11] Xiao, H. and Cinnella, P., "Quantification of model uncertainty in RANS simulations: A review," *Progress in Aerospace Sciences*, 2019.

[12] Duraisamy, K., Iaccarino, G., and Xiao, H., "Turbulence modeling in the age of data," *Annual Review of Fluid Mechanics*, Vol. 51, 2019, pp. 357–377.

[13] Murman, E. M., "A Correction Method for Transonic Wind Tunnel Wall Interference," *12th Fluid and Plasma Dynamics Conference*, 1979, p. 1533.

[14] Ma, B., Wang, G., Ye, Z., and Xu, L., "A numerical method for transonic wind tunnel wall interference correction in airfoil testing," *34th AIAA Applied Aerodynamics Conference*, 2016, p. 3575.

[15] Kato, H., Yoshizawa, A., Ueno, G., and Obayashi, S., "A data assimilation methodology for reconstructing turbulent flows around aircraft," *Journal of Computational Physics*, Vol. 283, 2015, pp. 559–581.

[16] Singh, A. P. and Duraisamy, K., "Using field inversion to quantify functional errors in turbulence closures," *Physics of Fluids*, Vol. 28, No. 4, 2016, pp. 045110.

[17] Duraisamy, K., Zhang, Z. J., and Singh, A. P., "New approaches in turbulence and transition modeling using data-driven techniques," *53rd AIAA Aerospace Sciences Meeting*, 2015, p. 1284.

[18] Parish, E. J. and Duraisamy, K., "A paradigm for data-driven predictive modeling using field inversion and machine learning," *Journal of Computational Physics*, Vol. 305, 2016, pp. 758–774.

[19] Singh, A. P., Duraisamy, K., and Zhang, Z. J., "Augmentation of turbulence models using field inversion and machine learning," *55th AIAA Aerospace Sciences Meeting*, 2017, p. 0993.

[20] Giles, M. B. and Pierce, N. A., "An introduction to the adjoint approach to design," *Flow, turbulence and combustion*, Vol. 65, No. 3-4, 2000, pp. 393–415.

[21] Pironneau, O., "On optimum design in fluid mechanics," *Journal of Fluid Mechanics*, Vol. 64, No. 1, 1974, pp. 97–110.

[22] Dwight, R. P. and Brezillon, J., "Effect of approximations of the discrete adjoint on gradient-based optimization," *AIAA journal*, Vol. 44, No. 12, 2006, pp. 3022–3031.

[23] Peter, J. E. and Dwight, R. P., "Numerical sensitivity analysis for aerodynamic optimization: A survey of approaches," *Computers & Fluids*, Vol. 39, No. 3, 2010, pp. 373–391.

[24] Albring, T. A., Sagebaum, M., and Gauger, N. R., "Development of a consistent discrete adjoint solver in an evolving aerodynamic design framework," *16th AIAA/ISSMO Multidisciplinary Analysis and Optimization Conference*, 2015, p. 3240.

[25] Albring, T. A., Sagebaum, M., and Gauger, N. R., "Efficient aerodynamic design using the discrete adjoint method in su2," *17th AIAA/ISSMO multidisciplinary analysis and optimization conference*, 2016, p. 3518.

[26] Economon, T. D., Palacios, F., Copeland, S. R., Lukaczyk, T. W., and Alonso, J. J., "SU2: An open-source suite for multiphysics simulation and design," *Aiaa Journal*, Vol. 54, No. 3, 2016, pp. 828–846.

[27] Vitale, S., Gori, G., Pini, M., Guardone, A., Economon, T. D., Palacios, F., Alonso, J. J., and Colonna, P., "Extension of the su2 open source cfd code to the simulation of turbulent flows of fuids modelled with complex thermophysical laws," *22nd AIAA Computational Fluid Dynamics Conference*, 2015, p. 2760.

[28] Liu, D. C. and Nocedal, J., "On the limited memory BFGS method for large scale optimization," *Mathematical programming*, Vol. 45, No. 1-3, 1989, pp. 503–528.

[29] Wilcox, D. C. et al., *Turbulence modeling for CFD*, Vol. 2, DCW industries La Canada, CA, 1998.

[30] Gatski, T. B. and Bonnet, J.-P., *Compressibility, turbulence and high speed flow*, Academic Press, 2013.

[31] Menter, F. R., "Two-equation eddy-viscosity turbulence models for engineering applications," *AIAA journal*, Vol. 32, No. 8, 1994, pp. 1598–1605.

[32] Kennedy, M. C. and O'Hagan, A., "Bayesian calibration of computer models," *Journal of the Royal Statistical Society: Series B (Statistical Methodology)*, Vol. 63, No. 3, 2001, pp. 425–464.

[33] Edeling, W., Cinnella, P., and Dwight, R. P., "Predictive RANS simulations via Bayesian model-scenario averaging," *Journal of Computational Physics*, Vol. 275, 2014, pp. 65–91.

[34] Cheung, S. H., Oliver, T. A., Prudencio, E. E., Prudhomme, S., and Moser, R. D., "Bayesian uncertainty analysis with applications to turbulence modeling," *Reliability Engineering & System Safety*, Vol. 96, No. 9, 2011, pp. 1137–1149.

[35] Edeling, W., Cinnella, P., Dwight, R. P., and Bijl, H., "Bayesian estimates of parameter variability in the k–ε turbulence model," *Journal of Computational Physics*, Vol. 258, 2014, pp. 73–94.

[36] Cook, P., Firmin, M., and McDonald, M., *Aerofoil RAE 2822: pressure distributions, and boundary layer and wake measurements*, RAE, 1977.

[37] Somers, D. M., "Design and experimental results for the S809 airfoil," Tech. rep., National Renewable Energy Lab., Golden, CO (United States), 1997.

[38] Schmitt, V., "Pressure distributions on the ONERA M6-wing at transonic mach numbers, experimental data base for computer program assessment," *AGARD AR-138*, 1979.

[39] Rudnik, R., "Untersuchung der Leistungsfähigkeit von Zweigleichungs-Turbulenzmodellen bei Profilumströmungen," *FORSCHUNGSBERICHT-DEUTSCHES ZENTRUM FUR LUFT UND RAUMFAHRT*, 1997.

[40] Jameson, A., Schmidt, W., and Turkel, E., "Numerical solution of the Euler equations by finite volume methods using Runge Kutta time stepping schemes," *14th fluid and plasma dynamics conference*, 1981, p. 1259.

[41] Singh, A. P., Medida, S., and Duraisamy, K., "Machine-learning-augmented predictive modeling of turbulent separated flows over airfoils," *AIAA Journal*, 2017, pp. 2215–2227.

[42] Mayeur, J., Dumont, A., Destarac, D., and Gleize, V., "RANS simulations on TMR test cases and M6 wing with the Onera elsA flow solver," *AIAA Paper*, Vol. 1745, 2015.

[43] Belligoli, Z., Dwight, R., and Eitelberg, G., "RANS Data Assimilation Techniques for Wind-Tunnel Wall Interference Corrections," *AIAA Aviation 2019 Forum*, 2019, p. 2976.

6
Conclusions

The use of automated design based on the adjoint method is one of the most widespread techniques for aerodynamic shape optimization problems. The first part of this dissertation showed its application for the optimization of a wing-body configuration to minimize the drag force. The novelty lays in the choice of deforming the body instead of the wing, and in removing any constraint on the direction of the deformation. The optimized body shape looks like a shallow dent wrapped around the junction region and reduces drag by activating a propulsive pressure force that would otherwise be dormant.

However, the uncertainties and errors in Reynolds-averaged Navier-Stokes (RANS) CFD simulations and wind-tunnel experiments of complex flow phenomena constitute a bottleneck for the complete validation of any aerodynamic design. This is why the second part of this dissertation focused on accurately reconstructing turbulent flow fields at high Reynolds numbers by reducing turbulence modeling errors, and correcting wind-tunnel wall interference effects. This objective was achieved by developing two variational data assimilation (DA) frameworks that inject sparse experimental data into a RANS code in order to correct the Reynolds stress tensor (RST) computed by a linear eddy viscosity turbulence model. The two DA techniques are characterized by two different choices of control parameters, and demonstrated an excellent ability to reconstruct complex flow fields while guaranteeing the physical realizability of the RST. Finally, one of the DA framework was extended to incorporate corrections to the experimental angle of attack and Mach number, thus being able to simultaneously correct turbulence modeling and wind-tunnel wall interference errors.

The main contribution of this dissertation can be summarized as follows:

- A novel geometry reducing drag at wing-body junctions was discovered through automatic design techniques based on the adjoint method. The new design is radically different from conventional aircraft fairings and works by generating a pressure force opposite to the drag force thanks to the interaction between the deformed body and the wing leading-edge.

- Two variational data assimilation techniques for the correction of the Reynolds stress tensor computed by an eddy viscosity turbulence model were developed. One uses the eigenvalues *and* eigenvectors of the RST as control parameters, while the other uses the components of the matrix resulting from the Cholesky factorization of the RST as control parameters and an objective function that penalizes perturbations that make the RST physically unrealizable.

- The application of the data assimilation frameworks to high Reynolds number test cases shows that only small perturbations to the eigenvalues are necessary to significantly improve the flow field reconstruction, and that the influence of the eigenvectors on this process is negligible.

- A new procedure based on the integration of experimental data and turbulent CFD simulations to correct non-linear wind-tunnel wall interference has been developed. The methodology can be applied as is to any type of wind tunnel, and requires to model neither the wind-tunnel walls, nor the ventilated wall boundary condition

as it directly corrects the in-tunnel results to free air conditions, thus considerably reducing the modeling effort.

6.1 Limitations and Recommendations

The following limitations and recommendations are outlined based on the findings presented in this work:

- The uncertainties associated to the RANS turbulence model prevent an accurate study of the anti-fairing's flow physics in the junction region. Hence, a detailed Large Eddy Simulation (LES) study should be carried out to analyze the evolution and changes to the secondary flow in presence of the anti-fairing.

- The anti-fairing's performance has been studied for the simple wing/flat plate configuration and at a single flow condition. A thorough sensitivity study at various flow conditions and with more complex geometries should be carried out to investigate the robustness of the design.

- The data assimilation frameworks of this work assume that the observational and prior covariance matrices are diagonal with constant variance. The effect of more complex covariance matrices on the quality of the final reconstruction should be investigated.

- The data assimilation frameworks of this dissertation use only pressure data as observations. However, they can be easily extended to incorporate other quantities, such as the velocity field, and/or the force coefficients. This would make the frameworks more flexible – as they can work with different types of observations – and also increase the accuracy of the reconstructed flow fields – as a larger number of observations provides more information for the inversion process.

Acknowledgements

There are also people with whom you intensely shared your life for some years but were driven away from you by the circumstances. Your relationship feeds off sporadic meetings or phone calls, maybe a WhatsApp chat. No matter how much time has passed from the last contact, it is always as if they never left. Notable mentions of this group are Steve, whom I put on a pedestal for his incredible ability to think with his own head, free from external influence, and Paride, whose restless search for meaning fills him with eternal energy.

I would also like to thank Martina, Matteo, Roberta, Giuliano, Marianna, Nicola, Massimiliano, Giulia, Guendalina, Dario, Roland, Giuseppe, Benoît for the lovely memories I carry of our time together.

Anna, my dear Anna, the biggest 'thank you' of all goes to you. For lighting up my life with your beautiful smile and your boundless sweetness. For putting up with my tantrums and healing my wounds. For being my lover and also my best friend. When I am by your side, I feel whole. To many more years of adventures together!

The last words of these acknowledgements go to my parents, Vittoria and Albano, to whom this dissertation is dedicated. Mi avete dato il dono della vita e dell'amore incondizionato, della libertà di scelta e del calore di un porto sicuro. Per questo e per tutto il resto, vi ringrazio di cuore.

Zeno Belligoli
Rotterdam, February 12, 2021

List of publications

Journal papers

Belligoli, Z., Dwight, R.P. and Eitelberg, G., 2020. "Reconstruction of Turbulent Flows at High Reynolds Numbers Using Data Assimilation Techniques". *AIAA Journal*, accepted for publication

Belligoli, Z., Dwight, R.P. and Eitelberg, G., 2020. "Non-Linear Wind-Tunnel Wall Interference Corrections Using Data Assimilation". *AIAA Journal*, **59**(2) pp. 596-606

Belligoli, Z., Koers, A.J., Dwight, R.P. and Eitelberg, G., 2019. "Using an Anti-Fairing to Reduce Drag at Wing/Body Junctions". *AIAA Journal*, **57**(4) pp. 1468-1480

Belligoli, Z., Dwight, R.P., Kok, G.J.P. and Lucas, P., 2017. "A Bayesian study of uncertainty in ultrasonic flow meters under non-ideal flow conditions". *Metrologia*, **54**(4), pp. 584.

Conference proceedings

Belligoli, Z., Dwight, R.P., Eitelberg, G., Srikumar, S., Faleiros, D., van Nesselrooij, M. and van Campenhout, O., 2020. "A Review of Numerical and Experimental Studies of the Anti-Fairing". *AIAA Aviation Forum*, Reno, NV - USA.

Belligoli, Z., Dwight, R.P. and Eitelberg, G., 2019. "RANS Data Assimilation Techniques for Wind-Tunnel Wall Interference Corrections". *AIAA Scitech Forum*, San Diego, CA - USA.

Belligoli, Z., Dwight, R.P. and Eitelberg, G., 2019. " Assessment of a Data Assimilation Technique for Wind-Tunnel Wall Interference Corrections". *AIAA Aviation Forum*, Dallas, TX - USA.

Patents

Belligoli, Z., Dwight, R.P. and Eitelberg, G. "Configuration of a T Junction of a Flow Obstacle on a Wall Bounding a Flow ". *EP3348470A1*, issued 6th March 2019.

About the author

by Anna Dolcetta

Zeno Belligoli (Verona, 1990), born and raised in the north of Italy, had always been top of the class in school and in sports throughout his childhood and teenage years. At the age of 18 he took up Aerospace Engineering in Milan and he had the chance to do the Erasmus program in Glasgow during which he not only increased his knowledge in Aerodynamics but also in typical Scottish drinks. After returning from Scotland and graduating with the highest vote, he was chomping at the bit to discover the world and gain more international recognition. So he moved to Delft for his Master studies and managed to obtain a patent for the design presented in his Master thesis. Inspired by the research carried out at TU Delft, he continued his academic career with a PhD in Computational Aerodynamics during which he had the chance to work on disparate topics and present his findings at international conferences. This dissertation is the final result of five full years of commitment, with all its successes and setbacks.